Probing the Dynamics of Dihydrofolate Reductase with Small Molecule Inhibitors

by
Mary J. Carroll

A dissertation submitted to the faculty of the University of North Carolina at Chapel Hill in partial fulfillment of the requirements for the degree of Doctor of Philosophy in the Eshelman School of Pharmacy (Pharmaceutical Sciences).

Chapel Hill
2011

Approved by:

Andrew L. Lee, Advisor

Sharon L. Campbell, Reader

Edward J. Collins, Reader

Harold Kohn, Reader

Jian Liu, Reader

Abstract

Mary J. Carroll
Probing the Dynamics of Dihydrofolate Reductase with Small Molecule Inhibitors
(Under the direction of Andrew L. Lee)

High-resolution protein crystal structures have served as the template from which to devise small molecule modulators of protein function through structure-based drug design for many decades. However, protein function, such as ligand binding, dissociation and catalysis, necessitates structural flexibility of the macromolecule. Protein dynamics are often ignored in structure-based design, largely due to limited information on protein flexibility in the presence of bound ligands (e.g., peptides or small molecules). To gain insight into how protein dynamics are modulated by the binding of small molecule inhibitors, nuclear magnetic resonance spectroscopy has been used herein to characterize both fast and slow timescale motions in the pharmaceutical target protein *Escherichia coli* dihydrofolate reductase. A series of inhibitors of the enzyme (antifolates) that cover a broad range of binding affinity have been studied while bound to the holoenzyme complex. In the presence of two high-affinity inhibitors, dynamics appear to be essentially identical on both the fast and slow timescales. Specifically, these two inhibitors decouple functional loop switching motions on the slow timescale. One medium-affinity antifolate from the series is shown to be conformationally flexible while bound to the enzyme, eliciting a functional switching motion in a loop distal to its binding. In considering the entire panel of eight antifolates (two of high affinity, one of medium affinity, and a homologous series five of reduced-affinity

antifolates), the rates of conformational switching of the enzyme on the slow timescale correlate well with ligand binding affinity and the kinetic rate of ligand dissociation. Within the sites exhibiting slow motions, a consensus set of residues is identified to be sampling a novel and structurally identical excited state that differs from physiological complexes bound to folate-derived ligands. This group of antifolate consensus residues is posited to serve as a mechanical initiator of ligand dissociation, an observation that may be quite prevalent in receptor-ligand interactions. Fast timescale motions across the series of antifolate complexes studied also suggest a correlation of flexibility with ligand binding affinity and a possible linkage between motions on the fast and slow timescales.

To my ninth grade science teacher and mentor, Miss Alice Reese, who first sparked my interest in science. Sadly, she passed away due to breast cancer while I was a student in her class. She battled through pain daily to do what she loved most – share with others her passion for science. I have chosen to dedicate my career to cancer research in her memory.

Acknowledgements

To fulfill the requirements of a Ph.D. requires an enormous amount of effort from the individual, but it is also impossible to complete without guidance and support from those around you. I would firstly like to thank my advisor, Andrew Lee, for the opportunity to work under his direction. My decision to attend UNC-CH for graduate school was based primarily on my interest in the Lee Lab. There was great competition amongst students for rotating in and joining the lab when I was a first-year student. Thus, I knew it would be necessary to work hard and earn a spot in the lab as a rotation student. By recognizing the unique skill set I brought to the lab, Drew provided me with a project that fit my interests well and gave me the opportunity to become a broadly trained experimentalist. He fostered my growth as an independent researcher, yet always was available to provide advice when called upon. Drew was very encouraging in my applying for external funding, and without such support, I likely would not have been as successful at winning fellowships. Aside from serving as my research mentor, Drew was also my advisor for two semesters of my teaching assistantship. He has very high expectations for his TAs, but the hard work and effort put in to teaching was very rewarding. My experience as a TA for his course makes me confident in my teaching abilities going forward in academics.

The decision I made to seek higher education following my undergraduate career was greatly influenced by my undergraduate mentor, Charles D. Schaeffer, Jr. Working under his guidance for four years sparked my scientific curiosity and made me enthusiastic for a career

in scientific research. His great interest in and excitement for Nuclear Magnetic Resonance was contagious, certainly driving me toward joining Andrew Lee's laboratory at UNC-CH. I only hope to someday approach Dr. Schaeffer's paramount work ethic.

I am indebted to two laboratories at UNC-CH with whom I have collaborated over the years. Scott Singleton graciously provided space for me to perform chemical synthesis and compound evaluation in his laboratory. The great discoveries made through this work could not have been possible without his willingness to accept my working part-time in his laboratory. Through making a series of small molecule inhibitors in Scott's laboratory came an interest in studying the structure of these molecules bound to their target. Edward Collins mentored me through the process of crystallizing multiple protein-ligand complexes and aided in structure determination using X-ray crystallography. Working with Ed not only generated very interesting data toward the goals of this project, but it also cultivated my interest in protein crystallography. His mentorship and excitement for structure determination has helped me to discover my true interest in structural biology. My search for a postdoctoral position was greatly impacted by our work together, for which I am very thankful.

I would also like to acknowledge the support and guidance of Sharon Campbell, Harold Kohn, and Jian Liu. The thoughtful advice and suggestions given by them during my committee meetings and in general discussions has had a significant impact on my progression and growth during the past several years. I am also indebted to my committee members for the numerous letters of recommendation they have willingly supplied toward fellowship applications and postdoctoral positions.

Core facilities on the campus of UNC-CH have been pivotal in this research. I am grateful for the technical expertise of Greg Young and Karl Koshlap, managers of the biomolecular NMR facilities on campus. Also, I acknowledge the assistance provided by Michael Miley, director of the X-ray crystallography core facility. Ashutosh Tripathy, manager of the Macromolecular Interactions Facility, also provided much training and advice during this research project for which I am grateful.

The daily grind of graduate school can take a hard toll on a person physically and mentally, generating a range of moods from severe depression to great excitement. This roller coaster is much more bearable when surrounded by genuinely caring and supportive coworkers. I am very thankful to have been guided by elder students in the Lee Lab, including Joshua Boyer, Randall Mauldin, and Matthew Whitley. I am particularly thankful for Randy's supervision during the early years of my graduate career, as we worked on the same protein system and share publications together. Randy's discoveries are highlighted throughout this work (methotrexate and holoenzyme studies) and have served as an excellent reference relative to my data. Postdoctoral fellows Chad Petit and Paul Sapienza and fellow students Anthony Law, Leanna McDonald, and Jun Zhang have been very supportive and provided a stimulating environment in which to work. I also thank Cristina Clay for the great effort she gave to keep the lab fully stocked and running smoothly.

Anna Gromova, a former postdoctoral fellow in Scott Singleton's laboratory, was not only a great collaborator, but she also became a great friend over the years. Anna was responsible for the preparation of several small molecule inhibitors used in this work, and she conducted biochemical assays to fully characterize the activity of the inhibitors. I constantly

sought her advice while performing chemical synthesis and for her willingness to help I am grateful.

As scientists, we are quick to recognize our coworkers and collaborators who made scientific contributions to a project. It is also important to thank those who helped with the administrative aspects of graduate school. I am very grateful for Amber Allen and Carrie Aldrich, two administrative assistants in the Eshelman School of Pharmacy, for their help and organization over the years. You have both become great friends of mine and I could not have made it through this process mentally without your support and open-door policy.

Finally, I would like to acknowledge my family for their continued support over the years. My husband Scott has been my biggest fan during this time, as he has provided much needed comforting words and moral support every day. I made a great sacrifice to move far from home in pursuit of my degree, but my family has been very understanding and accommodating of my career aspirations. My parents, Eugene and Mary, and my seven older brothers and sisters have been a large part of my success because of their great presence in my life. My father's fight against cancer during my tenure at UNC has further fueled my desire to be involved in cancer drug discovery. My brother John, who also earned his Ph.D., was a driving force in helping me seek out the best fit program for me. He always told me what to expect, helping me to not wander blindly into the unknown. I am so thankful for an inspirational family who has taught me to persevere against all odds and never stop short of my dreams.

Table of Contents

List of Tables

Chapter 1

Chapter 3

Chapter 4

Chapter 5

Appendices

List of Figures

Chapter 3

Chapter 4

Chapter 5

List of Abbreviations and Symbols

BMRB   biological magnetic resonance bank

CPMG   Carr-Purcell-Meiboom-Gill

CSA   chemical shift anisotropy

CSP   chemical shift perturbation

$\Delta\delta$ delta delta, steady-state difference in chemical shift

$\Delta\omega$ delta omega, dynamic difference in chemical shift

DHFR   dihydrofolate reductase

E   the enzyme, or DHFR

ΔG Gibbs' free energy

ΔH enthalpy

H_2F 7,8-dihydrofolate

H_4F 5,6,7,8-tetrahydrofolate

HMQC   heteronuclear multiple quantum coherence

HSQC   heteronuclear single quantum coherence

K_d equilibrium dissociation constant

K_i equilibrium inhibition constant

k_{ex} rate of chemical exchange

k_f forward rate component of k_{ex} – also called $k_{conf,forward}$

k_{off} kinetic dissociation rate

k_{on} kinetic association rate

k_r reverse rate component of k_{ex} – also called $k_{conf,reverse}$

MTX	methotrexate
μs-ms	micro- to millsecond
$NADP^+$	nicotinamide adenine dinucleotide phosphate, oxidized
NADPH	nicotinamide adenine dinucleotide phosphate, reduced
NMR	nuclear magnetic resonance
p_A	population of the major state
p_B	population of the minor state
ps-ns	pico- to nanosecond
PDB	protein data bank
R_1	longitudinal relaxation time
R_2	transverse relaxation time
$R_{2,eff}$	effective R_2
$R_{2,}^{o}$	intrinsic R_2
R_{ex}	conformation exchange contribution to R_2
RDC	residual dipolar coupling
S^2	backbone order parameter
S^2_{axis}	side-chain order parameter
τ_{cp}	spacing time delay between pulses in a CPMG train
τ_e	internal correlation time
$\tau_{e,axis}$	internal correlation time of the methyl symmetry axis
τ_m	rotational tumbling time
THQ	tetrahydroquinazoline
TMP	trimethoprim

χ^2 chi squared, a goodness of fit parameter

Chapter 1

Introduction

1.1. The need for dynamics data in drug design

Structure-based drug design is predicated on the rigid receptor hypothesis, in which the target protein of interest in assumed to be a static entity. Based on the static model of the target protein – likely a crystal structure – small molecules with shape and size complementarities to a binding site are sought as modulators of the protein's function. Computational approaches can be used to dock ligands in the binding site of interest and subsequently provide a score or rank for the binding interaction. However, it is well documented that proteins are not static under physiological conditions. Proteins are highly dynamic molecules in solution, breathing and flexing over a large timescale range from picoseconds to seconds. While we are well aware that the target is mobile, flexibility of the protein target is often ignored in *in silico* drug design. Two main reasons exist for the continued assumption of the rigid receptor hypothesis in computational methods: (i) the significant increase in computation time necessary for using an algorithm that incorporates protein target flexibility, and (ii) the lack of explicit experimental evidence for target plasticity, especially in ligand binding sites. *In silico* drug design can fail to accurately predict ligand binding affinities and also can predict incorrect ligand binding poses, at least

partly due to the ignorance of target flexibility. For example, in the case of thymidylate synthase binding to two inhibitors, computations predict incorrect binding poses and low scores for each inhibitor when using the other's crystal structure as a guide (1). By specifying flexibility in just three amino acid residues within the enzyme's binding site, a range of possible structures was generated as input into the computation, leading to significant improvements in scoring of novel inhibitors. This is just one example highlighting the importance of considering protein dynamics in structure-based drug design.

To apply knowledge of protein dynamics for improved structure-based drug design, an understanding of dynamics in receptor-ligand complexes is necessary. Protein dynamics or flexibility has been acknowledged from the analysis of high resolution crystal structures of a protein in the absence and presence of ligand (e.g., peptide or small molecule). The traditional view of ligand binding to receptor is based on size and shape complementaries: the lock and key description (2). This description applies when the structure of the bound complex does not differ from that in the absence of ligand and assumes no flexibility in the protein target or ligand. When structural differences are observed, flexibility has often been described by the 'induced fit' model, in which accommodation of the ligand is accomplished via distortion of the protein's structure (3). This apparent flexibility of the protein was thought to occur due to the binding of the ligand. More recently, it has been shown that proteins pre-exist in an ensemble of conformations that are constantly interconverting (4). Some of these pre-existing conformations are binding competent. Thus, ligand binds to that population of protein and causes a shift in the ensemble distribution towards stabilization of the binding competent conformation. This process, termed 'conformational selection,' prevails in the literature today.

The dynamic nature of proteins is implicit to function. For example, an enzyme must bind its substrate, catalyze a chemical reaction, and release the product. For the ligand binding and dissociation steps alone, significant flexibility must be present in the protein, as crystallography shows that 70-100% of ligand surfaces are buried when bound to the protein (5). Numerous studies highlight the direct relationship between enzyme flexibility and catalysis (6, 7), as will be discussed in later sections. Flexibility is of paramount importance in cell signaling, as the 'message' of ligand binding to an extracellular receptor must be relayed to the cytoplasm for a response to occur. Additionally, the shuttling of ions in and out of the cell is highly dependent upon the flexibility of various channels in the cell membrane. Thus, flexibility and dynamics are inherent to many classes of proteins, many of which are drug targets or implicated in disease states.

It is important to note that dynamics in receptor-ligand interactions can be observed in both the protein and the bound ligand. A range of flexibility in the protein is possible, from several residues within the binding sites reorienting up to large scale conformational changes of loops or subdomains (8-10). Flexibility can also be mutual, in that both the protein and the ligand change orientations to complement one another (8). Ligand promiscuity, in which one small molecule binds to multiple proteins, can result due to the highly dynamic nature of ligand binding sites. Some proteins have evolved great plasticity in ligand binding sites in order to perform a function, such as transport proteins and nuclear hormone receptors that bind a range of substrates (11).

Protein dynamics can also alter the kinetics of ligand binding and dissociation. For example in kinases, the DFG loop is known to exist in both 'in' and 'out' conformations. Some ligands bind only to one of these two conformations while others can bind either. The

ligands that bind only one conformation possess slow kinetic association rates, as a protein conformational change may be necessary for their binding (12). Some inhibitors may require hydrophobic collapse of the protein about the ligand, such as in one acetylcholinesterase inhibitor, resulting in slow inhibition kinetics as the protein undergoes the required conformational change (13).

Laying the foundation of protein flexibility and its multifaceted relationship to ligand binding begs the question: how can protein dynamics or flexibility be harnessed to improve structure-based drug design? One way in which flexibility can be useful is in the design of allosteric inhibitors. Such inhibitors bind at sites distal to the active or traditional binding site, and likely function through propagation of some dynamic change to the active site. The dynamic propagation may result in the protein being unable to bind its preferred substrate at the site distal to the inhibitor. Another useful way to harness protein flexibility is in driving a new conformational change upon ligand binding to improve selectivity. Instead of allowing the size and shape of the binding pocket seen by crystallography to dictate the size of the designed molecule, chemical additions to the ligand could be made to force structural changes in the protein to establish selectivity for that particular protein. As drug resistant mutations likely change flexibility of a ligand binding site, an understanding of those dynamic changes could allow new ligands to be designed that are more complementary to such mobility. Furthermore, the existence of a conformational ensemble under physiological conditions would allow for the targeting of conformations other than those on which we commonly focus (e.g., transient excited states). Stabilizing a transient excited state with a small molecule could result in therapeutics that are quite distinct from those targeting the visible ground state. Finally, and as illustrated earlier, information from detailed dynamics

studies could be incorporated into computational methods to improve our ability to predict

binding conformations and affinities for ligands.

1.2. Probing protein dynamics with NMR

While the need for incorporating or making use of protein dynamics in structure-based drug design is evident, the literature lacks explicit examples of studies detailing protein target flexibility in the presence of small molecule inhibitors. Multiple techniques exist for bridging this gap, including analysis of crystal structure temperature factors (*B* factors), fluorescence spectroscopy, molecule dynamics simulations, and NMR spectroscopy. Crystallographic *B* factors do provide information on the amplitude of motion at a particular site; however, they are not indicative of the motional timescale and also can vary due to static disorder instead of time-dependent motions. Fluorescence studies are dependent upon the addition of a fluorescent probe or label, which not only limit what can be studied to sites proximal to the probe, but also can cause structural perturbations to the protein. Molecular dynamics simulations, while very powerful, are typically only able to describe motions up to the nanosecond regime and also require experimental validation. NMR spectroscopy is well-suited for detailed studies of protein dynamics for several reasons. Firstly, it provides atomic level information on flexibility. In other words, dynamics data is collected on a per residue basis and affords a picture of flexibility both along the protein backbone and the variable side chains. Secondly, it allows for the study of dynamics across a range of timescales (Figure 1.1).
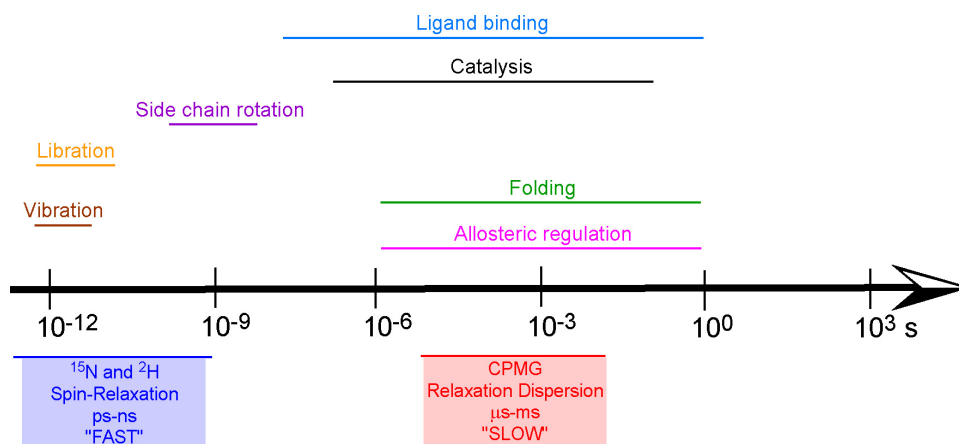
Figure 1.1. Dynamic motions in proteins occur over a broad range of timescales.

The two most commonly studied dynamic timescales include the "slow" or microsecond-millisecond (µs-ms) regime and the "fast" or picosecond-nanosecond (ps-ns) regime. Slow timescale motions include such things as ligand binding and dissociation, catalysis, protein folding, and allosteric regulation. As such, µs-ms motions are directly relevant for biological function (14). Fast timescale motions are comprised of bond vibrations and librations, and although not always apparently related to biology, may "lubricate" or form a foundation for the slower, biologically important motions (15). This study will focus primarily on µs-ms timescale dynamics in relation to ligand binding and dissociation (Chapters 2-4) with a smaller spotlight on ps-ns flexibility (Chapter 2 and 5).

Protein dynamics can be measured using what are called NMR spin relaxation experiments. In these experiments, the magnetization of the sample is perturbed from equilibrium, and the signal is observed as magnetization returns to its equilibrium state. The process by which non-equilibrium magnetization returns to equilibrium is called relaxation. Relaxation requires transitions between magnetic energy levels, stimulated by magnetic fields oscillating at the transition frequency (at or near the Larmor frequency of the nucleus).

6

The rate at which relaxation occurs depends on the likelihood of the nuclei experiencing the proper oscillating magnetic field. These oscillating fields could be due to movement of the nuclei relative to one another or relative to the magnetic field of the magnet, making relaxation very sensitive to molecular motion.

NMR spin relaxation experiments report primarily on the relaxation of ^{15}N and ^{13}C nuclei. The relaxation of these two nuclei on the ps-ns timescale is dominated by dipole-dipole interactions and chemical shift anisotropy (CSA) (15). Dipole-dipole relaxation results from the fluctuating magnetic field of two coupled nuclei as they rotate relative to the magnetic field of the magnet. For example, in ^{15}N relaxation, one considers a ^{1}H-^{15}N bond vector. Relaxation of the ^{15}N nucleus occurs due to fluctuations in the field of the ^{1}H nucleus, resulting from molecular tumbling or structural changes of the protein. This relaxation process is very dependent upon internuclear distance. CSA relaxation occurs as a result of a nucleus experiencing a fluctuating magnetic field due to variations in the shielding of the magnetic field of the magnet, arising from anisotropy of the electronic orbitals. While dipole-dipole and CSA relaxation mechanisms dominate, relaxation of transverse magnetization can also be affected by chemical or conformation exchange, as will be discussed in great detail in a later section. In brief, if the nucleus under study samples different conformations, the chemical shift change experienced dephases transverse magnetization, increasing its rate of relaxation.

To gain an understanding of the rotational motions of a bond vector, the time-dependent rotational correlation function must be defined. The rotational correlation function describes the probability that a bond vector (e.g., ^{1}H-^{15}N bond of the backbone) will have the same position relative to the magnetic field of the magnet at a time t after its start at

time zero (15). While this function always decays from 1/5 to zero (in solution) at infinite t, the shape of the correlation function provides information on motions of different time scales. However, relaxation parameters are better understood in terms of frequencies instead of times; therefore, it is more instructive to consider the Fourier transformation of the correlation function, called the spectral density function ($J(\omega)$). The spectral density function is, in other words, a distribution of all motional frequencies experienced by the bond vector. By collecting NMR spin relaxation data, we are attempting to reconstruct the spectral density function, a formidable task. As a decent approximation, we can evaluate its shape by determining the function at five different frequencies: $J(0)$, $J(\omega_X)$, $J(\omega_H)$, $J(\omega_H + \omega_X)$, and $J(\omega_H - \omega_X)$. To map the spectral density function, three relaxation parameters are determined by NMR, generally at two different static magnetic field strengths: R_1 (longitudinal relaxation rate constant), R_2 (transverse relaxation rate constant), and the NOE (nuclear Overhauser effect) (16). These three relaxation parameters can be determined by an analysis of peak intensity differences. How these relaxation parameters relate to the spectral density function are shown below for the case of ^{15}N or ^{13}C with a singly attached ^{1}H (15):

$$R_1 = R_1^{DD} + R_1^{CSA}, \tag{1.1}$$

$$\text{where} \quad R_1^{DD} = \frac{1}{4}d^2\left[J(\omega_H - \omega_X) + 3J(\omega_X) + 6J(\omega_H + \omega_X)\right] \tag{1.2}$$

$$\text{and} \quad R_2^{CSA} = c^2 J(\omega_X) \; ; \tag{1.3}$$

$$R_2 = R_2^{DD} + R_2^{CSA} + R_{ex}, \tag{1.4}$$

$$\text{where} \quad R_2^{DD} = \frac{1}{8}d^2\left[4J(0) + J(\omega_H - \omega_X) + 3J(\omega_X) + 6J(\omega_H) + 6J(\omega_H + \omega_X)\right] \tag{1.5}$$

$$R_2^{CSA} = \frac{1}{6}c^2\left[4J(0) + 3J(\omega_X)\right] \tag{1.6}$$

and R_{ex} = conformational exchange broadening;

$$NOE = 1 + \frac{1}{4} d^2 T_1 \left(\frac{\gamma_H}{\gamma_X} \right) \left[6J(\omega_H + \omega_X) - J(\omega_H - \omega_X) \right]. \qquad (1.7)$$

In the above equations, c and d are constants while γ_H and γ_X are the gyromagnetic ratios for ^{1}H and the heteronucleus.

Once the shape of the spectral density function has been mapped via the relaxation parameters determined from NMR experiments, a motional model is generally applied to interpret the molecular motions. In this work, the Lipari-Szabo model-free formalism is used to evaluate the defined spectral density function. The model-free formalism allows for the separation of global tumbling motions from internal motions or dynamics (17). The idea behind this formalism is that internal motions of protein bond vectors are independent from the overall rotational tumbling of the protein, as internal motions are generally much faster than tumbling. In addition, the rotational tumbling of the protein influences each individual bond vector in a predictable and sometimes identical manner (for proteins undergoing isotropic tumbling), whereas internal motions of the bond vectors are independent of one another.

If the global rotational tumbling time (τ_m) is known, the internal motions can be analyzed by fitting the relaxation data to the following equation:

$$J(\omega) = \frac{2}{5} \left(\frac{S^2 \tau_m}{1 + (\omega\tau_m)^2} + \left(\frac{(1 - S^2)\tau}{1 + (\omega\tau)^2} \right) \right), \qquad (1.8)$$

$$\text{where } \tau^{-1} = \tau_m^{-1} + \tau_e^{-1}. \qquad (1.9)$$

The fitting yields two model-free parameters, S^2 and τ_e, to be described below. The above equation is solved in terms of a series of models (models 1-5) that are mathematical

expressions incorporating different assumptions about the timescales of internal motions or the presence of conformational exchange. Although 'models' are being used in this approach, the formalism is considered 'model-free' in that no motional mechanism (i.e., diffusion in a cone, two-site jump) is assumed for the internal motions. A summary of models 1-5 and the parameters fit on a per residue basis are provided in Table 1.1 (15).

Model	Parameters Fit	Assumptions
1	S^2	$\tau_e \ll \tau_m$, no R_{ex}
2	S^2, τ_e	$\tau_e < \tau_m/5$, no R_{ex}
3	S^2, R_{ex}	$\tau_e \ll \tau_m$
4	S^2, τ_e, R_{ex}	$\tau_e < \tau_m/5$
5	S^2_s, S^2_f, τ_s	$\tau_f \ll \tau_m$, $\tau_s \geq \tau_m/5$, no R_{ex}

Table 1.1. The five mathematical models of the model-free formalism.

To determine τ_m for the model-free approach, a global grid search is performed by fitting the R_1, R_2, and NOE data to model 2 (18). The grid search starts broad (e.g., 5-15 ns) and is narrowed (e.g., 10-11 ns) until the point lowest in error is found, taken as the best value for the global tumbling time. Residues with elevated R_2 values that are suspect of slower conformational exchange motions are removed from the analysis before grid searching begins.

Several new parameters describing the internal motion appear in the above table from the fitting procedure. The first is S^2, or the generalized order parameter. This parameter describes the re-orientational amplitude of bond vector motion and ranges anywhere from zero to one. An S^2 value of one corresponds to a completely rigid N-H bond vector while a value of zero corresponds to a completely disordered or isotropic vector. In studying ^{15}N relaxation, this parameter is fit for every resolvable peak in a 2D NMR spectrum, or for each amide of the protein backbone. A second parameter shown is τ_e, or the effective correlation time of motion of that studied amide bond vector. There are certain assumptions about the value of τ_e, mainly that it is assumed to be much faster than τ_m. A third parameter mentioned

is R_{ex}. This is an indication of elevated R_2 values, suggestive of internal motions on the slower µs-ms timescale due to conformational exchange. Finally, model 5 represents complex motions that can be decomposed into independent fast and slow components,

$$S^2 = S^2{}_f S^2{}_s . \qquad (1.10)$$

Along with $S^2{}_f$ and $S^2{}_s$ comes fast and slow effective correlation times, τ_f and τ_s. Because of the occurrence of R_{ex} and the complex motions of model 5, models 3-5 report on internal motions of two timescales.

It turns out that for most well-folded proteins, the dynamic range of S^2 values is relatively narrow. What is more telling of protein flexibility is an analysis of dynamics along protein side chains, where flexibility is much more variable (Figure 1.2).
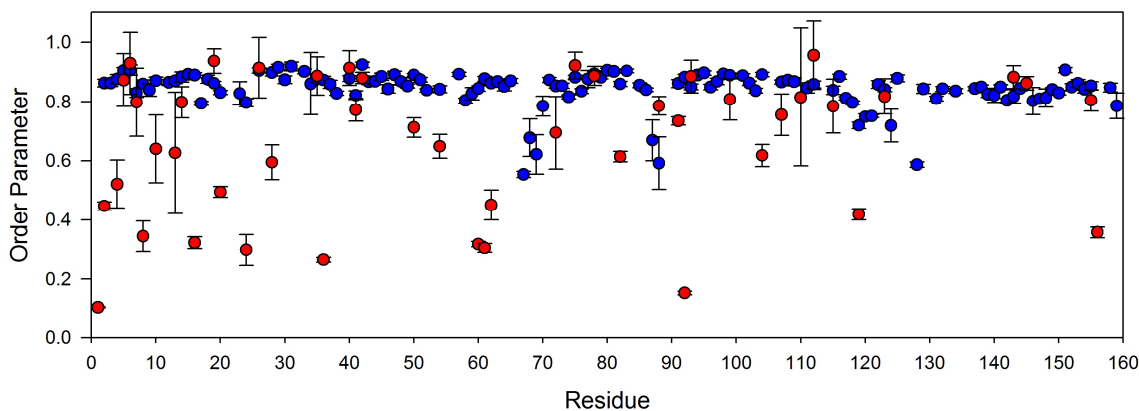
Figure 1.2. Backbone (blue) and side-chain (red) order parameters for a representative ternary complex of *E. coli* dihydrofolate reductase.

In a similar manner to studying the flexibility of the backbone, ps-ns dynamics of methyl-bearing side chains can be studied by using ^{2}H relaxation experiments. These experiments utilize fractionally deuterated protein, focusing on the quadrupolar relaxation of the CH_2D methyl isotopomer (19). The quadrupolar longitudinal (D_z) and transverse (D_y) relaxation

rates are measured from experiments developed by Kay and coworkers, the equations

describing the relaxation processes are shown below (20):

$$D_z = \frac{3}{16}\left(\frac{e^2qQ}{\eta^2}[J(\omega_D)+4J(2\omega_D)]\right) \tag{1.11}$$

$$D_y = \frac{1}{32}\left(\frac{e^2qQ}{\eta^2}[9J(0)+15J(\omega_D)+6J(2\omega_D)]\right), \tag{1.12}$$

where e^2qQ is the quadrupolar coupling constant, set to 165 kHz. Quadrupolar relaxation

results from an electrostatic interaction between the quadrupolar moment of a nucleus (with a

spin of ≥ 1) and the electric field gradient. This mechanism is about 1-2 orders of magnitude

more efficient than dipole-dipole or CSA contributions. Thus, other forms of autorelaxation

are considered negligible. The model-free analysis of D_z and D_y relaxation rates yields S^2_{axis},

the order parameter of the methyl side-chain symmetry axis, and $\tau_{e,axis}$ describing the

effective internal correlation time. Unlike S^2 values for the protein backbone, S^2_{axis} values

are quite sensitive to perturbations such as mutation and ligand binding (21-25).

It is well accepted that, in solution, proteins can sample multiple conformations via

thermal fluctuations. Chemical or conformation exchange includes processes that alter the

magnetic environment of the nuclei under study. In the simplest case of chemical exchange,

a dynamic equilibrium exists between two states, A and B:

$$A \underset{k_r}{\overset{k_f}{\Longleftrightarrow}} B . \tag{1.13}$$

The forward conversion of A to B is dependent upon the forward rate constant, k_f, while the

reverse conversion of B to A depends on the reverse rate constant, k_r. Chemical exchange

motions occur on the slow, or microsecond-millisecond (μs-ms) timescale and are detectable

by ^{15}N relaxation experiments and the model-free analysis (models 3 and 4) due to elevation

of R_2 (15). However, the R_2 experiment conducted to fit model-free parameters actually

serves to dampen or keep constant the effects of conformational exchange (26). It is

therefore important to not over-interpret the detection of R_{ex} from model-free analysis.

Instead, conformational exchange on the μs-ms timescale is better studied using R_2 relaxation

dispersion experiments (27). As mentioned previously, R_2 is the rate of transverse or spin-

spin relaxation primarily determined by fluctuations on the ps-ns timescale. However, the

presence of chemical exchange causes an apparent increase in R_2 on a per residue basis. ^{15}N

Carr-Purcell-Meiboom-Gill (CPMG) R_2 relaxation dispersion experiments allow for

decomposition of R_2 into R_{ex}, the relaxation rate component due to conformational exchange,

and R_2^{o}, all the remaining contributions to transverse relaxation on the faster timescale (28):

$$R_2 = R_2^{o} + R_{ex} \ .$$
(1.14)

The overall rate of transverse relaxation (R_2) is directly proportional to the half-height

linewidth of resonances, and thus as R_{ex} increases R_2 values, resonances undergoing

exchange experience line broadening. For the assumption of a two-state exchange process,

R_2 depends on the exchange rate constant (k_{ex}), the populations of ground state A and excited

state B (p_A and p_B), and the difference in chemical shift between states A and B ($\Delta\omega$) (28).

Thus, from these experiments, kinetic, thermodynamic and structural information,

respectively, can be obtained to describe the sampling of a lowly populated substate.

Relaxation dispersion experiments are sensitive to minor substates sampled by

proteins in solution, given that the minor substate is populated to at least 1% and chemical

shift differences between the two states are large (29). Therefore, these experiments can

provide information on 'invisible' substates: those for which peaks cannot be detected in a

HSQC or in other spin-relaxation experiments. Contributions to R_2 from R_{ex} can be

suppressed by the application of an external B_1 magnetic field: R_{ex} decreases as the B_1 field strength increases, as illustrated in Figure 1.3.
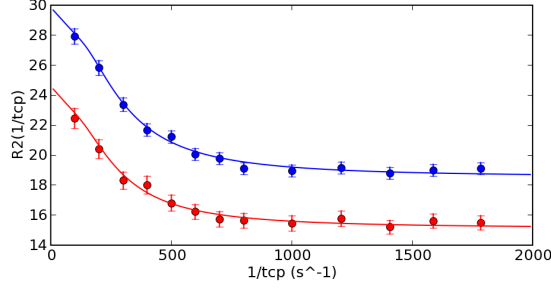
Figure 1.3. Sample relaxation dispersion curve of a residue in dihydrofolate reductase. Data at 700 and 500 MHz are shown in blue and red, respectively.

The field strength of the applied B_1 field is modulated by the frequency of applied 180° refocusing pulses during the CPMG (τ_{CP} – 180° pulse – τ_{CP}) train of the pulse sequence. The frequency by which refocusing pulses are applied is controlled via the parameter τ_{CP}, or the delay between the 180° pulses. Short values of τ_{CP} can suppress R_{ex} completely while long values of τ_{CP} can partially affect R_{ex}. The data points in Figure 1.3 plateau at the intrinsic R_2 rate (R_2^o) if R_{ex} has been completely suppressed. The effective rates of transverse relaxation ($R_{2,eff}$) come from the conversion of peak intensities in the experiment to R_2 values via the following equation (30):

$$R_{2,eff} = -\frac{1}{T}\ln\frac{I}{I_0} \ , \tag{1.15}$$

where T is the length of the total constant time relaxation period and I and I_0 are the peak intensities in the presence and absence of the constant time CPMG period. The data points in Figure 1.3 can be fit to the Carver-Richards equation in order to determine k_{ex} (the sum of k_f and k_r), p_A and p_B, $\Delta\omega$, and R_2^o at each field (31):

$$R_2(1/\tau_{CP}) = \frac{1}{2}\left(R_{2A}^o + R_{2B}^o + k_{ex} - \frac{1}{\tau_{CP}}\cosh^{-1}\left[D_+\cosh(\eta_+) - D_-\cos(\eta_-)\right]\right) \tag{1.16}$$

14

$$\text{where } D_\pm = \frac{1}{2}\left[\pm 1 + \frac{\Psi + 2\Delta\omega^2}{\left(\Psi^2 + \xi^2\right)^{1/2}}\right] \tag{1.17}$$

$$\eta_\pm = \frac{\tau_{CP}}{\sqrt{2}}\left[\pm\Psi + \left(\Psi^2 + \xi^2\right)^{1/2}\right]^{1/2} \tag{1.18}$$

$$\Psi = \left(R_{2A}{}^o - R_{2B}{}^o - p_A k_{ex} + p_B k_{ex}\right)^2 - \Delta\omega^2 + 4 p_A p_B k_{ex}{}^2 \tag{1.19}$$

$$\xi = 2\Delta\omega\left(R_{2A}{}^o - R_{2B}{}^o - p_A k_{ex} + p_B k_{ex}\right). \tag{1.20}$$

Relaxation dispersion experiments have been applied in studies attempting to correlate dynamics with enzyme function and catalysis, such as in RNase A and cyclophillin (7, 32). Others have used these experiments to understand the sampling of folded and unfolded states of proteins in solution (33), as well as to describe the process of ligand binding (30, 34).

1.3. Dihydrofolate reductase as a model system

Dihydrofolate reductase, or DHFR, is a small, monomeric enzyme that catalyzes the NADPH-dependent reduction of 7,8-dihydrofolate (H_2F) to form 5,6,7,8-tetrahydrofolate (H_4F) (Figure 1.4).
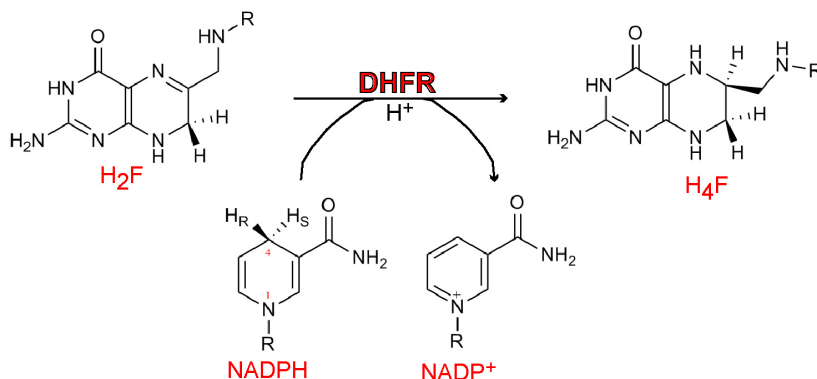
Figure 1.4. The stereospecific reduction of dihydrofolate to tetrahydrofolate, catalyzed by DHFR.

H_4F is a very important cofactor in the cell, as it carries one-carbon units that are ultimately used in biosynthetic pathways to produce thymidylate, purines, and methionine. Because the intracellular pool of H_4F is maintained solely by the action of DHFR, a successful way to control DNA replication and hence cell proliferation is by inhibiting the action of this enzyme. For this reason, DHFR has been exploited as a drug target since the 1940s for treating diseases such as cancer, bacterial infections, and malaria (35). Interestingly, small molecules that bound to DHFR were found to be effective against cancer before the enzyme had been identified. These first DHFR inhibitors led to its subsequent discovery and extensive characterization at present.
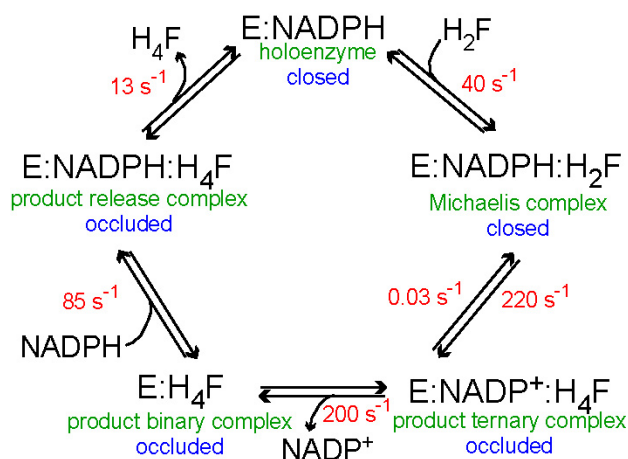
Figure 1.5. The catalytic cycle of dihydrofolate reductase. Kinetic characterization results are shown in red (36). The general name of each complex and the conformation of the Met20 loop are given in green and blue, respectively.

Found across all organisms, DHFR is a ubiquitous enzyme. While there is great structural similarity across species, sequence homology is much lower ($< 30\%$) (37). DHFR catalyzes the reduction of H_2F to H_4F, necessitating the cofactor NADPH. The reaction is stereospecific, in which the 4-*pro-R* hydrogen of the reduced cofactor is transferred to C6 of the pteridine ring of H_2F (37). As DHFR binds two ligands, the order of binding and release

16

is very important, and the mechanism of catalysis can be described as ordered bi-bi in nature. To perform the full cycle, the enzyme uses five steps, depending on the ligands bound in its two binding sites, as shown in Figure 1.5. The kinetics of the steps have been determined via fluorescence studies by Benkovic and coworkers (36). Release of the product H_4F, the rate-limiting step of catalysis, occurs only after the oxidized cofactor ($NADP^+$) dissociates and is replenished with reduced cofactor (NADPH). Thus, DHFR never samples an apo-enzyme form physiologically.

The *Escherichia coli* isoform of DHFR had been studied extensively by X-ray crystallography. There are approximately fifty structures deposited in the Protein Data Bank (PDB), in which the enzyme has been crystallized both in different space groups and with a wide array of ligands (38-43). Most of these structures show DHFR while bound to endogenous ligands or models thereof, such as the substrate, product, cofactor, and their derivatives. Only a handful of structures possess substrate-competitive inhibitors within the active site, such as methotrexate (MTX) (42-44).
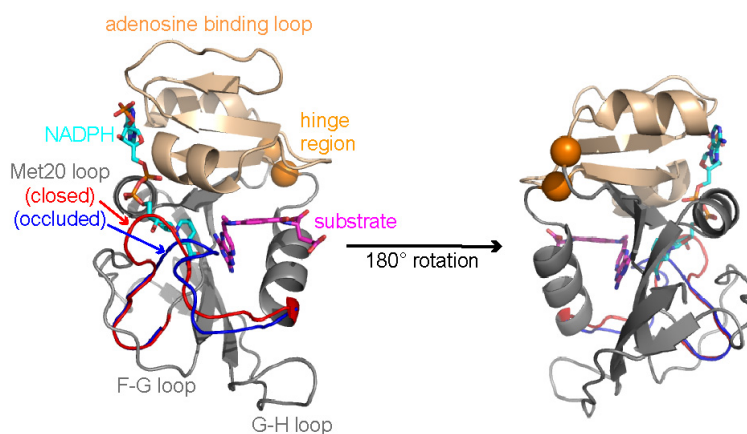
Figure 1.6. The structure of *E. coli* DHFR, highlighting important structural features. The adenosine binding and loops subdomains are colored in wheat and gray, respectively.

DHFR consists of an eight-strand β-sheet motif surrounded by four α-helices. The enzyme's active site, where both cofactor and substrate bind, divides the protein into two subdomains: the adenosine binding and the loops subdomains (Figure 1.6). The former is so named due to its close association with the adenosine of NADPH. The latter subdomain is comprised of about fifty percent loops. There are three highly flexible loops within this region, known as the Met20, the F-G, and G-H loops. The two subdomains are able to move relative to one another due to hinge motions at Lys38 and Val88, known to widen or narrow the active site cleft (42).

From the wealth of crystal structures, particularly a series of isomorphous structures of the five kinetic intermediates, a sequence of subdomain and loop movements have been tracked throughout the catalytic cycle (42). The Met20 loop, which closes over the active site, has been observed to sample three different conformations crystallographically: closed, occluded, and open. These conformations are stabilized by differential hydrogen bonding patterns. When in the closed conformation, the Met20 loop packs tightly against the nicotinamide-ribose moiety of NADPH to position it near to the substrate, facilitating the hydride transfer event. The closed conformation is found in the holoenzyme complex (E:NADPH) and in the reactive complex (E:NADPH:H_2F). Following the hydride transfer reaction, the Met20 loop undergoes a global conformational switch from closed to occluded. For this switch to occur, hydrogen bonds between the Met20 loop and the F-G loop must be broken, while new bonds between the Met20 loop and the G-H loop form to stabilize the occluded state. Interestingly, the nicotinamide-ribose moiety of NADP$^+$ is expelled from the active site when the loop is occluded, as the side chains of Met16 and Glu17 flip inwards to occupy its binding site. The expulsion of nicotinamide could facilitate the loss of NADP$^+$

18

and rebinding of reduced NADPH. DHFR's Met20 loop is found in the occluded

conformation in the complexes following hydride transfer and leading up to product release

(E:NADP$^+$:H$_4$F, E:H$_4$F, and E:NADPH:H$_4$F). The open Met20 loop conformation appears to

be a composite of the closed and occluded states, considered an intermediate in the transition

between the two. This state appears to be stabilized by crystal contacts in certain space

groups (42).

Because crystallographic studies of DHFR set precedent for motions within the loops

and subdomains of DHFR, NMR dynamics studies on the enzyme followed suit. The apo-

enzyme exhibits high frequency backbone motions in the Met20 and associated F-G and G-H

loops (45). Such motion is seen in other complexes in which the Met20 loop is occluded

(E:folate and E:DHNADPH:folate) (46, 47). These ps-ns motions are attenuated when the

Met20 loop assumes the closed conformation in response to the binding of ligands in the

folate binding site or forming ternary complexes (47). Side-chain dynamics studies on closed

versus occluded complexes mirror these observations of backbone flexibility (48).

Additionally, high frequency motions of the methyl-bearing side chains are observed in the

F-G loop in the E:NADP$^+$:folate Michaelis model complex (48). More recent studies have

focused on characterizing μs-ms timescale motions of DHFR in the complexes of the

catalytic cycle (6, 49-51). Interestingly, in the E:NADP$^+$:folate complex, widespread μs-ms

timescale motions have been observed, including a number of sites known to be chemical

shift markers of the Met20 loop conformation. Using relaxation dispersion experiments, a

functional switching of the Met20 loop from closed to occluded in the excited state has been

observed via a linear correlation between Δω fitted from relaxation dispersion experiments

with the steady-state difference in chemical shift (Δδ) between Met20 loop closed and

occluded conformations (51). Further efforts have characterized the energy landscape and associated dynamics throughout the catalytic cycle of the enzyme (6). This study has revealed that the enzyme appears to function by a selective fit mechanism, where each intermediate of the catalytic cycle samples the following catalytic intermediate as a higher-energy substate through slow timescale conformational changes. The transiently sampled excited states become the major state as the enzyme moves forward in the cycle. Very recently, the exquisite dynamic and thermodynamic sensitivity of DHFR to its bound ligand when the Met20 loop is occluded in nature has been reported (50).

1.4. Antifolates: Substrate-competitive inhibitors of DHFR

Considering the function of DHFR as the sole producer of H_4F for DNA replication and cell division purposes, inhibiting the activity of DHFR serves as a common route to treating diseases such as cancer, bacterial infections, and malaria. Small molecule inhibitors which bind in the folate binding site of DHFR are more commonly referred to as antifolates. The aforementioned MTX, along with trimethoprim (TMP) and pyrimethamine are examples of clinically useful antifolates (Figure 1.7).
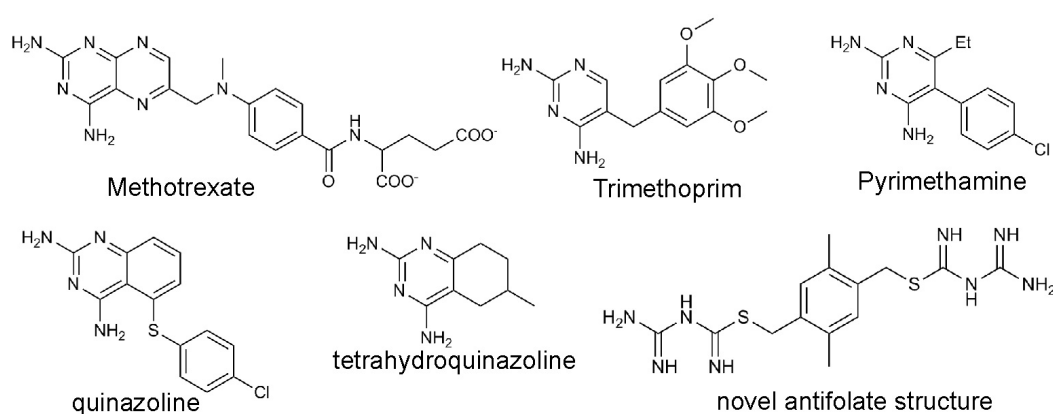

Figure 1.7. Sample substrate-competitive inhibitors of DHFR.

20

Methotrexate, a classical antifolate, is highly similar in chemical structure to folic acid, differing only at two positions (i.e., 4-amino and *N*-10-methyl modifications). The pteridine ring system of MTX likely contributes most of the interactions important to its high affinity for DHFR, in that its 2,4-diaminopyrimidine moiety forms several important hydrogen bonds to the enzyme (52). Non classical pteridine analogs containing the 2,4-diaminopyrimidine core but lacking the *p*-aminobenzoylglutamate tail were thus explored as novel folate antagonists (53). Given that quinazoline and pteridine ring systems are isosteric, lipophilic 2,4-diaminoquinazoline compounds were found useful as antibacterial and antimalarial agents (54). From this finding, 2,4-diaminotetrahydroquinzoline analogs were evaluated as antifolates (55, 56). Even smaller in size and maintaining the important pharmacophore are the 2,4-diamino-5-benzylpyrimidine antifolates, of which TMP is the most commercially successful (57). Recently, one high-affinity antifolate has been identified that does not contain the 2,4-diaminopyrimidine or quinazoline scaffolds (43). Of these structurally similar classes of antifolates, some are species specific and others bind across species (58). For example, MTX targets human DHFR for treatment of leukemias and lymphomas; however, it also binds with a high affinity to *E. coli* DHFR (59, 60). On the contrary, TMP is highly specific for bacterial forms of DHFR, and pyrimethamine to the *P. falciparum* isoform (57, 61).

Over the years, great synthetic efforts have focused on generating high affinity and species specific antifolates possessing the TMP scaffold to be used as antibacterial agents (62-74). However, these inhibitors are prone to mutational drug resistance (75, 76). One recent study aimed to overcome this problem by identifying novel *E. coli* DHFR antifolate

scaffolds via screening a large library of diverse compounds available commercially from Maybridge (77). This group identified several novel chemical scaffolds that differed from the gold standard antibacterial folate antagonist TMP. A number of hit compounds reported were of the quinazoline and tetrahydroquinazoline classes. As discussed in later chapters, several of these antifolates have been chosen for study in this work, including one quinazoline compound and one tetrahydroquinazoline (Figure 1.7), expanded into a series of structurally similar compounds (Figure 1.8). Of the novel scaffolds identified, only one compound was similar to TMP in its K_i value (MJC-7 in Figure 1.8). Upon solving the structure of this novel inhibitor while bound to *E. coli* DHFR, it appears to sample a different part of the active site that TMP cannot access (43). Therefore, it may show promise against resistance mutations. New chemical scaffolds that inhibit the activity of DHFR would be useful, given the prevalence of drug resistant mutants limiting the use of antifolates in general (75, 76, 78). Another approach would be to understand if dynamics of DHFR play a role in conferring resistance to small molecule inhibitors. If so, inhibitors could be designed to target functional dynamics or to avoid flexible portions of the active site as a means to overcome such mutations.

Because DHFR has been extensively utilized as a drug target, we can take advantage of the wealth of published antifolates, their synthetic schemes, and their characterization data in the current study. As will be described below, a series of antifolates has been chosen from the literature for this work. Several of the series are commercially available (MTX, TMP, and trimetrexate), while the remainder have been prepared synthetically (Figure 1.8).
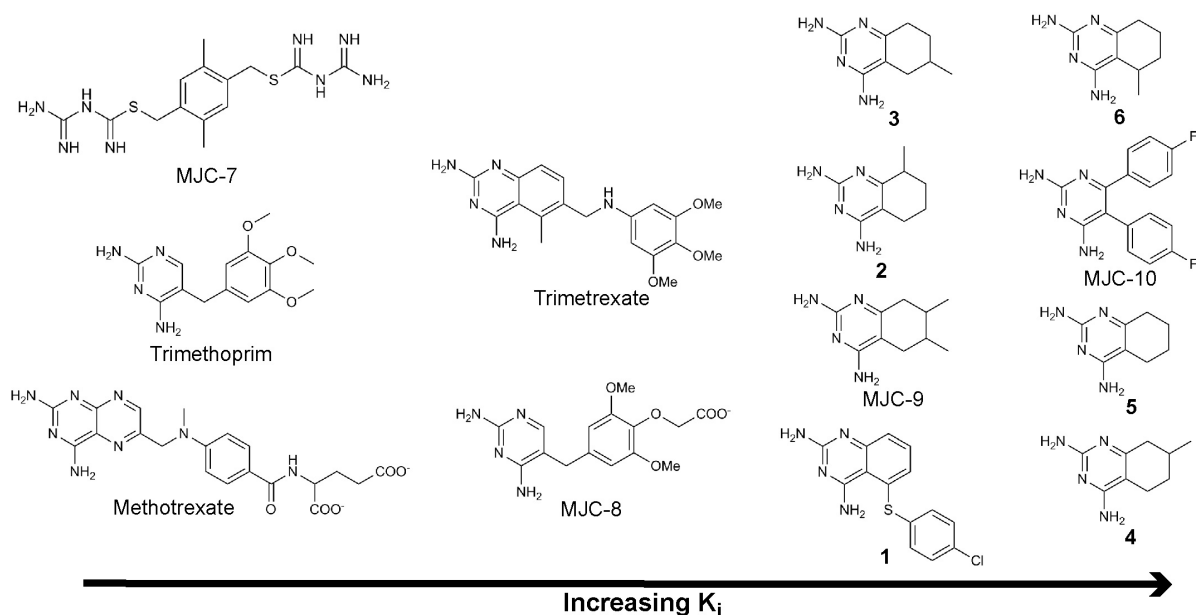
Figure 1.8. The series of antifolates chosen from the literature for this study.

1.5. Synopsis of this work

It is clear that DHFR has been extensively characterized in the past, regarding its structure, dynamics, and ability to be inhibited by small molecules. Where I can make new contributions to this system, and more relevantly to the realm of drug design, is by studying the impact of small molecule inhibitor binding and dissociation on DHFR's dynamics. More specifically, I am interested in how the flexibility of the enzyme differs when bound to a series of antifolates that cover a broad range of binding affinity (Figure 1.8). In Chapter 2, I characterize the changes in slow and fast timescale dynamics that result upon the binding of the high-affinity antifolate TMP. These data, in combination with data collected in the presence of MTX and in the absence of drug (data collected by Randall Mauldin) (79), provide an interesting set of observations to serve as reference points for the later chapters. TMP and MTX binding modulates dynamics of the holoenzyme identically on both timescales, despite differences in the chemical structure of the two inhibitors. In Chapter 3,

the structure and slow timescale dynamics of DHFR in the presence of a novel reduced-affinity quinazoline inhibitor are described (40). Ironically, the X-ray crystal structure and solution NOE data identify two different binding poses for the quinazoline inhibitor. These two binding conformations are rationalized by the presented slow timescale dynamics, which point to drug switching motions in the bound state. In Chapter 4, an investigation of slow timescale dynamics for a series of structurally similar tetrahydroquinzoline compounds is presented (41). These data, in combination with data described in Chapters 2-3, identify a consensus group of residues within the active site that exhibit slow timescale motions regardless of chemical structure or binding affinity of the bound antifolate. I report that this group of residues samples a novel and identical excited state in the presence of all antifolates studied, and that the rate at which DHFR switches to this state is highly dependent on K_i and the kinetic off-rate (k_{off}) of the ligands. From this, I hypothesize that the excited state mediates dissociation of the inhibitors. Finally, in Chapter 5, the beginning of a full-scale ps-ns dynamics analysis in the presence of three reduced-affinity inhibitors from the series is presented. Correlations between fast timescale dynamics and K_i are also apparent from these data, and a dynamics balancing act is suggested by comparing backbone and side-chain motions. Altogether, these results bring to the forefront the importance of understanding protein dynamics and how they are modulated by small molecule inhibitors.

Chapter 2

Identical Modulation of Dynamics Results from High Affinity Antifolate Binding

2.1. Introduction

In traditional structure-based drug design, high resolution protein crystal structures are used as a template from which to devise small molecules that are complementary to a particular binding site for modulating protein function. However, under physiological conditions, proteins are highly dynamic and can sample a number of conformations. Protein flexibility is ignored in drug design largely due to an inadequate understanding of how dynamics influence small molecule binding and dissociation (5). While studies have characterized protein dynamics in the presence of endogenous ligands (i.e., substrate and product) (6, 7, 80), very few examples of explicit dynamics determinations in the presence of exogenous small molecules exist (81-85), and those studies in the literature generally focus on ps-ns flexibility of the protein backbone. For this reason, we herein report the structure and dynamics of a common pharmaceutical target protein, *Escherichia coli* dihydrofolate reductase (DHFR), in the presence and absence of small molecule inhibitors. NMR spectroscopy is well-suited for this study, as it provides information on protein structure in

solution and also allows for protein dynamics to be studied on multiple timescales with atomic level resolution.
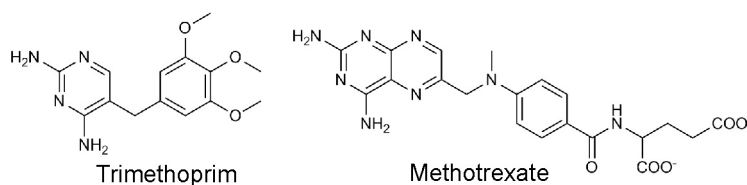
Figure 2.1. The chemical structures of trimethoprim and methotrexate.

The results presented in this chapter show the differences in dynamics that result upon binding of the high-affinity, clinically useful antifolate trimethoprim (TMP) to the E:NADPH holoenzyme complex (Figure 2.1). The analysis of both μs-ms and ps-ns dynamics are presented for this complex (referred to as E:NADPH:TMP). By themselves, these data are not very informative. However, relative to the absence of inhibitor (E:NADPH) and in combination with data on a second ternary inhibited complex with methotrexate (MTX) (Figure 2.1), E:NADPH:MTX (collected by former Lee Lab graduate student, Randall Mauldin), these data afford an interesting picture of how high affinity antifolates modulate the dynamics of the enzyme (79). Also, since all three of these studied complexes are contained within the Met20 loop closed conformation, this study allows for dynamics differences within the same structural state to be analyzed. Past reports of DHFR dynamics have only focused on dynamics modulation between complexes exhibiting different loop conformations (6, 47, 48, 51). Furthermore, this chapter serves as a reference point for the later chapters that will discuss the dynamic impact of reduced-affinity antifolates binding to the holoenzyme. It was found that TMP and MTX, despite their differences in chemical structure, elicit nearly identical patterns of dynamics on both the fast and slow timescales. Motions on the slow timescale are consistent with a decoupling of

26

motion in the Met20 loop and active site observed in physiological complexes, such as the E:NADPH holoenzyme. Residues proximal to the drug binding site remain flexible in the presence of TMP and MTX; however, loop motions distal to the substrate binding site are quenched. Unlike the slow motions concentrated within the active site, changes in fast timescale dynamics of the backbone and methyl-bearing side chains are dispersed across the entire protein. Propagation of dynamic changes to sites in the adenosine binding subdomain distal to the substrate binding site is observed, affecting sites that are highly conserved and implicated in catalysis. The results in this chapter, as well as complete analyses, were reported previously (79).

2.2. Materials and Methods

2.2.1. Protein Expression and Purification

DHFR was expressed in M9 minimal media supplemented with combinations of $^{15}NH_4Cl$, U-$^{13}C_6$-glucose, and ^2H_2O. Following a 5-6 hour induction period, cells were harvested by centrifugation. The cell pellet was resuspended in Lysis Buffer (20 mM sodium phosphate, 50 mM sodium chloride, 1 mM EDTA, 1 mM DTT, pH 7.0). Cells were lysed via sonication, and DHFR was subsequently purified similar to previously published methods (86). Briefly, cell lysate was loaded onto a MTX-agarose column that had been equilibrated with Lysis Buffer. Following the loading stage, the column was washed (Lysis Buffer containing 750 mM NaCl) to remove molecules which bound non-specifically. DHFR was eluted from the affinity column with Elution Buffer (20 mM sodium borate, 750 mM NaCl, 1 mM EDTA, 1 mM DTT, 5 mM folate, pH 9.5). The concentrated eluent was then loaded onto a G-50 size exclusion column equilibrated with KPE Buffer (50 mM

potassium phosphate, 150 mM KCl, 1 mM EDTA, 1 mM DTT, pH 7.2) to remove excess, unbound folate. Remaining bound folate was removed by dialysis of the concentrated G-50 pool against KPE containing 5 M deionized urea. DHFR was finally passed over a G-50 column equilibrated with NMR Buffer (70 mM HEPES, 20 mM KCl, 1 mM EDTA, 1 mM DTT, pH 7.6). The pool was concentrated, separated into aliquots for NMR experiments, flash frozen, lyophilized, and stored at 4 °C until use.

2.2.2. NMR Spectroscopy

NMR samples contained 1 mM isotopically labeled DHFR in NMR Buffer, 15 mM NADPH, 10 mM glucose-6-phosphate, 10 *U* glucose-6-phosphate dehydrogenase, 1.1-1.25 mM TMP, and 10% D_2O for spectrometer locking purposes. All samples were protected from light and air exposure by containment in amber NMR tubes flame-sealed under argon. Stock solutions of TMP (1.4 mM) were prepared by prolonged stirring of the carefully weighed solid in NMR Buffer. All NMR experiments were conducted at 298 K on Varian spectrometers equipped with room temperature (500 and 600 MHz) or cryogenic (500 MHz and 700 MHz) probes. NMRPipe was used to process NMR data, and data visualization was accomplished with the combination of NMRDraw and NMRView (87, 88).

Standard triple-resonance experiments were used to complete the backbone and side-chain resonance assignments of E:NADPH:TMP. HNCACB, CBCA(CO)NH and HNCA experiments were used to assign the $^{1}H^{N}$, ^{15}N, $^{13}C^{\alpha}$, and $^{13}C^{\beta}$ resonances of the backbone (89). Residues that could not be assigned, likely due to chemical exchange, include D11 and A145. Side-chain assignments for ^{1}H and ^{13}C methyl resonances were made using (H)CCH$_3$-

TOCSY and HMBC (90, 91). Stereospecific assignments of leucine and valine methyl groups were determined using the method of Neri and coworkers (92).

Relaxation dispersion experiments were conducted on protonated E:NADPH:TMP at 500 and 700 MHz using a 40 ms total constant time CPMG period (28). Sixteen HSQC-like planes were collected by varying the interpulse delay, τ_{CP}, from 0.556 to 10 ms. Two of these planes were duplicate measurements for error propagation purposes and one plane served as the reference (lacking the CPMG period). Peak intensities were extracted using the nlinLS module of NMRDraw.

R_1, R_2, and {^{1}H}-^{15}N NOE data were collected at 500 and 600 MHz using standard backbone relaxation experiments (16). T_1 sampling delay times were as follows: 49*, 139, 254, 389*, 544, 709, 894, 1004*, and 1304 ms. T_2 sampling delay times were as follows: 7.8*, 15.7, 23.5, 39.2*, 62.7, 78.3, 94.0, 109.6*, and 125.3 ms. D_z and D_y data were collected at 600 and 700 MHz using the side-chain ^{2}H relaxation experiments described by Kay and coworkers (20). D_z sampling delay times were as follows: 4.15*, 10.9, 19.6, 30.0*, 41.8, 54.8, 68.9, 84.1*, and 100.4 ms. D_y sampling delay times were as follows: 0.7*, 2.1, 3.8, 5.9*, 8.3, 10.9, 13.7, 16.8*, and 20.0 ms. Three duplicate planes were collected for both ^{15}N and ^{2}H relaxation experiments for the purpose of error estimation, as denoted by an asterisk.

2.2.3. Relaxation Dispersion Analysis

A two-state model of exchange was assumed for motions on the μs-ms timescale. Residues for which $R_{2,eff}$ changed by more than 2 s^{-1} over the τ_{cp} range were considered for further analysis. An F-test (α critical = 0.01) was used to identify residues with significant exchange, testing whether residues best-fit to the exchange model or to a model lacking

exchange ($R_2 = R_2^o$). Residues passing the F-test were fit using the Carver-Richards equation (equation 1.16) to determine k_{ex}, p_A and p_B, R_2^o at both fields, and $\Delta\omega$ (28, 31). Errors in the fitted parameters were determined by Monte-Carlo simulations. Residues undergoing slow timescale exchange can often move in a concerted fashion, with shared k_{ex} and p_A values. DHFR is known to possess ligand-independent motions at regions containing residues 129-134 and 155-159 (6, 79). Exchange at these residues was also identified in the current study, but they were excluded from global analysis of the data. Global fitting of the remaining residues was accomplished via the strategy of Kay and coworkers (30), in which the ratio of $\chi^2_{global}/\chi^2_{local}$ is used to identify residues that fit better locally and not within the group.

2.2.4. ^{15}N and ^{2}H Relaxation Analyses

For ps-ns timescale motions, data were analyzed by the Lipari-Szabo model-free formalism (17). The isotropic rotational tumbling time for E:NADPH:TMP was found to be 10.7 ns/rad at 298 K. Because rotational anisotropy can have a profound impact on model selection (93), the presence of anisotropy was analyzed in E:NADPH:TMP via the local D_i method (94) using the in-house program qfit and Protein Data Bank (PDB) code 1RX3 for E:NADPH:MTX. The D_{par}/D_{perp} value for E:NADPH:TMP was found to be 1.13, and anisotropy was used in subsequent data fitting of backbone dynamics. Using the in-house program relxn2.2, the backbone relaxation rates were fitted to the five models of the model-free formalism. Akaike's information criterion was used to select the best fit motional model (95). Side-chain relaxation rates were fit to model 2 with no application of rotational anisotropy to the data fitting procedure.

2.3. Results and Discussion

2.3.1. Chemical shifts show structural similarity for E:NADPH:TMP and E:NADPH:MTX

Although the Protein Data Bank (PDB) contains approximately fifty crystal structures

of *E. coli* DHFR, only a few structures possess bound antifolates in the substrate binding site

(42-44). For example, the crystal structure of E:NADPH:MTX (PDB ID 1RX3) has been

solved (42), but E:NADPH:TMP has not. What does exist is a solution structure for

Lactobacillus casei E:NADPH:TMP (96). Because the crystal structure of *E. coli* DHFR

bound to reduced cofactor and TMP has not been solved, I characterized the structure of this

complex via NMR. This structure is expected to be quite similar to that of E:NADPH:MTX,

given the similarity of the *E. coli* E:NADPH:MTX crystal structure with that of *L. casei*

E:NADPH:TMP (RMSD = 1.43 Å). Therefore, instead of solving the solution structure of *E.*

coli E:NADPH:TMP, one can approach the question by first comparing differences in

chemical shifts elicited by the two inhibitors. A lack of significant differences in chemical

shift could preclude the need to solve the structure of E:NADPH:TMP. The site specific

chemical shift perturbations (CSPs) as a result of TMP binding were calculated relative to the

absence of inhibitor (E:NADPH:TMP – E:NADPH). A box plot function in SigmaPlot was

used to identify those CSPs that were considered to be outliers, and those residues are

highlighted in Figure 2.2. Most sites 'sensing' the ligand by a change in chemical shift are

within the folate binding site, as would be expected. Many of these sites considered CSP

outliers are shared with the sites perturbed by MTX binding, suggesting structural changes

are minimal (Figure 2.3) (79).
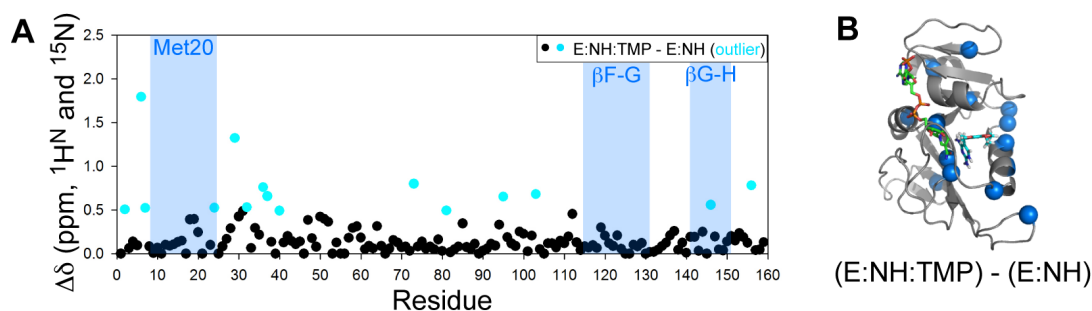
Figure 2.2. CSPs of E:NADPH:TMP relative to E:NADPH. (A) A box plot function was used to identify significant outliers in CSPs upon TMP binding. (B) These outliers are highlighted in blue colored spheres on the structure of DHFR.
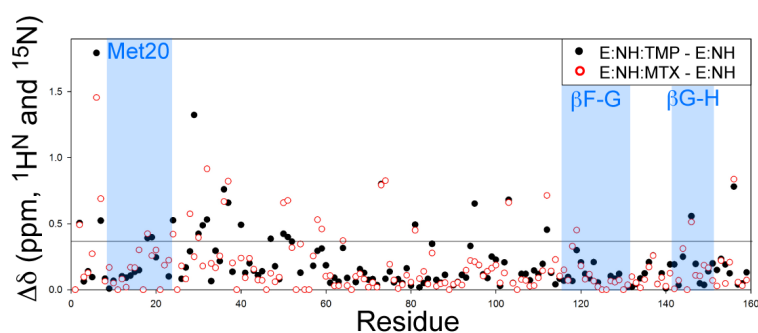
Figure 2.3. CSPs of E:NADPH:TMP and E:NADPH:MTX relative to E:NADPH. The line represents an approximate threshold for significant chemical shift changes in both complexes.

Interestingly, sites exhibiting significant CSPs in response to TMP or MTX do not localize to the Met20, F-G, or G-H loops. This suggests that the Met20 loop conformation in E:NADPH:TMP is likely the same as that in E:NADPH:MTX.

For a more detailed analysis of Met20 loop structure in solution in the presence of TMP, additional CSPs can be calculated relative to model chemical shifts for known Met20 loop conformations. Wright and coworkers have carefully analyzed chemical shift differences between a complex known to possess a closed Met20 loop (E:NADP+:folate) and one known to exhibit an occluded Met20 loop (E:DHNADPH:folate) (97). These chemical shifts have been deposited in the Biological Magnetic Resonance Bank (BMRB). There are approximately twenty residues that report directly on the conformation of the Met20 loop,

based on this previous analysis. Therefore, CSPs for E:NADPH:TMP relative to these two complexes have been calculated, specifically focusing on the residues known to be markers of the Met20 loop conformation, shown in Figure 2.4.
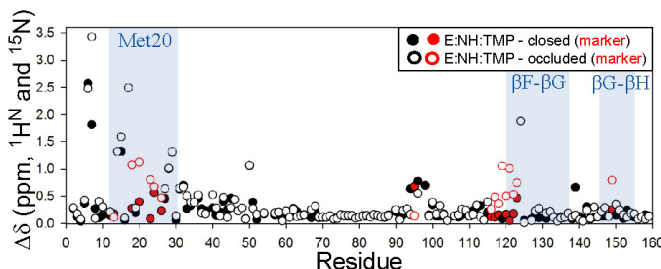
Figure 2.4. CSPs of E:NADPH:TMP relative to model closed and occluded complexes. Residues highlighted in red are markers of the Met20 loop conformation.

Of the twenty marker residues, only V13 and I94 have chemical shifts more similar to an occluded Met20 loop conformation. This strongly suggests that the Met20 loop in the E:NADPH:TMP complex is closed in solution. In support of this, a residual dipolar coupling (RDC) analysis (performed by Randall Mauldin) further suggests the prevalence of the closed conformation for the Met20 loop in the TMP ternary complex (79). This was also the case for E:NADPH:MTX.

2.3.2. Decoupling of functional active site motions on the slow timescale

As discussed in section 1.3, DHFR is known to possess significant μs-ms timescale motions while bound to endogenous ligands, and such conformational excursions from the ground state step the enzyme through its catalytic cycle (6). We wondered how these dynamics would be modulated by the binding of high affinity small molecule inhibitors, such as TMP and MTX. ^{15}N CPMG relaxation dispersion experiments were used to identify μs-ms motions in the E:NADPH:TMP complex. The data were fitted to the Carver-Richards

equation to determine k_{ex}, p_A and p_B, and $\Delta\omega$ for the sites with significant dispersion. These

data are presented in comparison to the absence of inhibitor (E:NADPH) and to the

E:NADPH:MTX complex (6, 79). In addition to motions observed in the ligand independent

sites (128-134 and 157-158) (6), R_{ex} was identified at the following residues in the presence

of TMP: 7-10, 28-31, and 111-112 (Figure 2.5A).
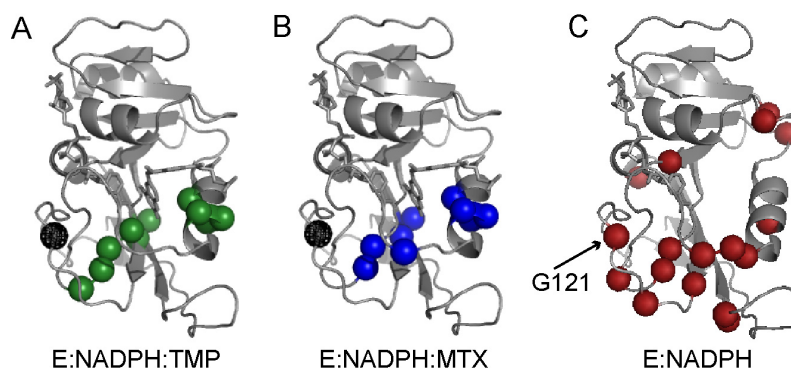
Figure 2.5. R_{ex} in the presence and absence of TMP and MTX. Backbone sites experiencing slow timescale motions are identified by colored spheres for (A) E:NADPH:TMP, (B) E:NADPH:MTX, and (C) E:NADPH.

When compared to the sites with slow motion in the E:NADPH:MTX complex (Figure

2.5B), TMP and MTX appear to elicit μs-ms motions at an essentially identical pattern of

residues. The consensus residues between the two ternary inhibitor complexes are residues

8-9, 28-31, and 111-112. MTX elicits detectable dynamics at Ile14 which is not observed in

the presence of TMP. It is worth noting that motions on this timescale are only detected in

the loops subdomain of the enzyme.

Global fitting of k_{ex} and p_A for the sites with slow motion was performed on

E:NADPH:TMP and compared to the same analysis of E:NADPH:MTX. It turns out that not

only do the same sites exhibit slow motion in the presence of these two high affinity

antifolates, but the rate of switching in the two are also identical. Both complexes sample the

excited state to about 2% in solution. The global rates of exchange were fit to 460 ± 170 (see

Appendix 2.1) and 430 ± 150 s^{-1} for TMP and MTX, respectively. This leads to the

calculation of the forward rate of exchange, $k_{conf, forward}$, of 10.6 ± 3.8 and 7.4 ± 2.7 s^{-1},

respectively. Therefore, TMP and MTX, despite differences in their chemical structures,

elicit identical patterns of slow motions, both in the sites affected and the rates of switching.

It is instructive to compare this dynamic pattern due to drug binding to a reference

state – the absence of inhibitor. Such a comparison allows for an understanding of how

DHFR's dynamics are modulated by the two high affinity inhibitors. Sites at which slow

timescale motions are detected by relaxation dispersion experiment in E:NADPH are shown

in Figure 2.5C. Dynamics are observed at sites within the active site, the hinge region, and

also in the F-G and G-H loops. Interestingly, slow motions are present at G121, a marker for

conformational exchange of the Met20 loop (51, 97). It has been previously reported,

however, that motion of the Met20 loop in the E:NADPH complex is not coherent between

closed and occluded forms (6). But, seeing motion at G121 indicates that the Me20 loop is

not static. In the presence of TMP or MTX, motion at G121 is quenched (black sphere in

Figure 2.5A-B). This suggests that these two high affinity inhibitors freeze motion of the

Met20 loop when bound. In general, both TMP and MTX quench µs-ms timescale motions

in the enzyme, as evidenced by a decreasing number of sites with significant dispersion

relative to E:NADPH.

The dynamic result of high-affinity antifolate binding to the holoenzyme appears to

be a decoupling of active site and loop motions. R_{ex} is observed at residues within close

contact to the bound inhibitors in the active site; however, the functional loop motions

detected in E:NADPH and E:NADP$^+$:folate are quenched. DHFR can be considered a

dysfunctional, half-switching enzyme in the presence of TMP and MTX, as the rate of forward switching in these two inhibitor complexes is about the same as seen for physiological complexes, but switching is only observed for residues proximal to the drug binding site.

2.3.3. Highly similar ps-ns flexibility results upon TMP and MTX binding

Fast timescale flexibility of DHFR has been previously studied for complexes of the catalytic cycle, in which the enzyme is bound to endogenous ligands. It was found that large differences in backbone and side-chain flexibility were only observed when comparing complexes with a closed Met20 loop relative to an occluded loop (47, 48). No large differences were observed when two closed Met20 loop complexes were compared. We were interested in determining if ps-ns dynamics were different in the case of ligand binding within the closed Met20 loop state. Both backbone and methyl side-chain ps-ns dynamics have been characterized for the E:NADPH:TMP complex. Backbone amide order parameters (S^2) were probed by collecting ^{15}N R_1, R_2 and {^1H}-^{15}N NOE experiments at two fields and fitting the data to the model-free formalism. An anisotropic diffusion tensor was used in the model selection process. Side-chain order parameters (S^2_{axis}) were probed with D_z and D_y experiments collected at two fields. Similar to the slow timescale motions reported in section 2.3.2, ps-ns flexibility in E:NADPH:TMP will be presented in comparison to E:NADPH:MTX and the reference E:NADPH complex.

Site-specific differences in flexibility of the backbone and side chains (ΔS^2 and ΔS^2_{axis}) have been calculated relative to the absence of TMP (i.e., E:NADPH:TMP – E:NADPH). A site is considered to have a significant change in flexibility if its ΔS^2 or

ΔS^2_{axis} is greater than two times the error in the fitted model-free parameter. Such sites are identified below in Figure 2.6, indicated in either blue (backbone) or red (side-chain) colored spheres. Sites with significant changes in backbone dynamics include residues 33, 51, 73, 134, and 159 (Appendix 2.2). Changes in side-chain flexibility are noticed at residues 8, 28, 36, 50, 60-62, 104, 107, and 115 (Appendix 2.3). Thus for the binding of TMP, significant changes in flexibility are observed across the entire sequence of DHFR, both in the adenosine binding and loops subdomains. This is different than the case of μs-ms motions, which were only observed within the loops subdomain.
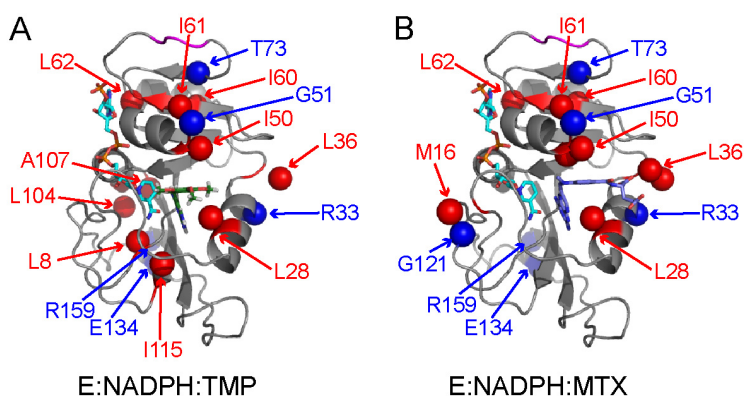
Figure 2.6. Significant differences in backbone and side-chain dynamics relative E:NADPH for (A) E:NADPH:TMP and (B) E:NADPH:MTX. Perturbed residues 67-69 of the adenosine binding loop are colored magenta, while blue and red spheres indicate significant changes in backbone and side-chain flexibility, respectively.

The side-chain flexibility of β-sheet C (residues 60-62) is greatly perturbed by TMP binding, which is interesting given that these residues are outside of the binding pocket, highly conserved in DHFR, and important in a statistical coupling analysis (98). Also, decreases in backbone flexibility that lie just below our stringent threshold of significance are observed for residues 67-69 of the adenosine binding loop (magenta loop), very distal to the active site. Many of these sites afflicted dynamically are highly conserved in DHFR and have been linked to promoting catalysis (98). Because the binding of TMP within the active site

imparts changes in flexibility at many sites within the adenosine binding subdomain, a dynamic link between the active site and this subdomain is probable. One might envision a path of dynamic changes that propagates from the active site where TMP binds up through α-helix C, β-sheet C, β-sheet D, and ending at the adenosine binding loop. Past reports of fast timescale dynamics have shown a similar propagation of dynamics that link two distal, coupled sites (21, 23).

In comparing the changes in ps-ns flexibility of TMP and MTX, a very similar pattern is observed, building on what was previously reported for the μs-ms timescale. A core pattern of both changes in backbone and side-chain flexibility is observed for the two antifolates (residues 28, 33, 36, 50, 51, 60-62, 73, and 134), with only a few additional unique residues changing significantly in flexibility outside of this pattern. Furthermore, it is interesting to note that most of these significant changes in flexibility (i.e., E:NADPH:antifolate – E:NADPH) are positive, indicating rigidification of DHFR upon the binding of these two inhibitors to the holoenzyme. Therefore, not only do TMP and MTX quench motion on the slow timescale, but they also quench fast timescale motions. The magnitudes of ΔS^2 and ΔS^2_{axis} relative to E:NADPH are even similar for E:NADPH:TMP and E:NADPH:MTX (ΔS^2 $R = 0.74$; ΔS^2_{axis} $R = 0.65$), although not identical. One final note to make regarding these observed changes in ps-ns dynamics is that these differences are observed within the same conformational state (closed Met20 loop). Previous studies focused on how dynamics changed upon switching of the loop from closed to occluded (47, 48). Our study demonstrates that flexibility of DHFR can vary within a single state and that some of the differences observed between TMP and MTX binding may be the result of the binding of two structurally dissimilar antifolates.

2.4. Concluding Remarks

Characterizing the changes in structure and dynamics that result upon the binding of the high-affinity antifolate TMP provide an interesting framework in which to interpret later results in Chapters 3-5. TMP binding induced minimal structural changes in the enzyme relative to MTX binding. Specifically, the Met20 loop appears to assume the closed conformation, similar to the absence of inhibitor and the presence of the structurally different inhibitor MTX. The binding of TMP has quenched slow motion at several sites compared to the absence of inhibitor. The pattern of slow timescale dynamics is essentially identical to that induced by MTX in both the identity of the sites affected and the rate of conformational exchange. While residues within the active site are mobile, these two inhibitors appear to freeze motion of the Met20 loop that is observed in the absence of bound antifolates, thus decoupling the active site from the flexible loops. Similarly on the fast timescale, TMP and MTX binding elicit changes in backbone and side-chain flexibility that are highly correlated in identity and magnitude. Sites in both subdomains of DHFR are modulated, suggesting a dynamic link between the subdomains and the active site. As many of the sites impacted by antifolate binding are highly conserved and implicated in catalysis, a link between ps-ns dynamics and function is suggested.

Chapter 3

Direct Detection of Structurally Resolved Dynamics in a Multi-Conformation Receptor-Ligand Complex

3.1. Introduction

High-resolution crystal structures have classically provided the information that drives structure-based drug design. However, such structures are static models and are not representative of the dynamic nature of proteins under physiological conditions *in vitro* or *in vivo*. Proteins undergo constant motions in solution (dynamics), and they can also flex their structures such that the time-averaged, 'static' coordinates change significantly (flexibility). Both complicate the process of structure-based drug design (5, 99) and hence are often ignored in the design of small molecule inhibitors (100). This is one of the main reasons why prediction of binding affinities (and efficacies) is fraught with inaccuracies and drug design is dominated by an empirical approach. Although computational methods are being developed to account for molecular dynamics in free energy calculations, dynamics can exist over a wide range of timescales, some of which are still inaccessible to those methods (101). We propose here that experimental determination of the dynamic properties of protein-small molecule complexes will speed the development of reliable methods to more accurately predict ligand binding affinities.

There are several ways in which knowledge of protein flexibility and/or dynamics can aid structure-based drug design, according to different views. Flexibility is most commonly acknowledged from multiple crystal structures of the same protein bound to different ligands, in which the protein adopts different conformations ('induced fit'). This is now often viewed as reflecting the inherent flexibility in the absence of ligand ('selected fit'). *A priori* knowledge of flexible residues (e.g., from crystal structures) can be used to model active site conformational changes that might occur, even in a homologous protein, on binding a given small molecule (99). Induced fit behavior is also seen from the ligand side: minor changes to ligand structure can drastically affect its mode of binding, resulting in different orientations in the binding site (5, 101, 102). The second view, orthogonal to induced and selected fit, recognizes that binding free energy is not restricted to arise only from non-covalent bonding within the binding site. For example, changes in the nature of the conformational ensemble can influence the overall entropy (22). Thus, the dynamics of the whole system, both the free and bound states (of protein and ligand), become important. Third, as there is often a relationship between dynamics and function, drugs may be developed to inhibit (or activate) functional dynamics, as opposed to acting directly on the binding site (103). This strategy figures prominently in the development of allosteric drugs (104, 105). Finally, it has been proposed that dynamics play an important role in mediating drug resistance, as demonstrated in a recent study on the Bcr-Abl fusion kinase (106). In principle, accounting for dynamics should improve prediction accuracy of binding affinities. This is underscored by the recent finding that 85% of the proteins with deposited structures have 1-3 "flexible" residues within their ligand binding pockets (10), and that most ligand receptors show an increase of atomic mobility for some ligand binding site atoms (107).

Given the large number of examples from crystallographic studies implicating conformational heterogeneity as an important consideration for small molecule design, it is surprising that relatively few studies have reported more direct characterizations of dynamics in complexes of small, drug-like molecules with their targets. It stands to reason that accurate information on target and small molecule flexibility in solution should be gained to lay a foundation for developing more sophisticated methods that incorporate dynamics into drug design. Here, we have identified a small molecule-target enzyme interaction that is inherently dynamic. The target, *E. coli* dihydrofolate reductase (DHFR), is a popular target for drug design against microbial infections, and the human enzyme is the target for cancer chemotherapy agent methotrexate (108). The bacterial enzyme bound to a quinazoline derivative (Figure 3.1) is shown here to exhibit conformational dynamics, both in the enzyme and the small molecule. From NMR spectroscopy and X-ray crystallography, the compound was found to bind in an unorthodox orientation but switch internally to drive a dynamic conformational loop change in the protein. The two methods used jointly are highly complementary, and both are necessary to develop a full, accurate picture of this small molecule complex.

3.2. Materials and Methods

3.2.1. Synthesis of Compound 1

Compound **1** was prepared in one step by the method patented previously by Singh and Gurney (109). Characterization information can be found in Appendix 3.1.

3.2.2. Protein Expression and Purification

Isotopically labeled wild-type *Escherichia coli* DHFR was over-expressed and purified as described previously in Chapter 2 (79). For relaxation dispersion experiments, ^{15}N labeled and highly deuterated (~80%) protein was used. Purified apo-DHFR was frozen in a dry ice and ethanol bath, lyophilized, and stored in a desiccator at 4 °C until use.

3.2.3. K_i Determination

Biochemical competition assays using a 96-well plate reader were used to determine the inhibition constant (K_i) for **1**. **1** was added to a reaction of DHFR, NADPH, and dihydrofolate substrate, and depletion of NADPH was monitored by UV absorbance at 340 nm (77). The total reaction volume was 100 μL.

3.2.4. NMR Spectroscopy

NMR samples contained 1 mM isotopically labeled DHFR in NMR buffer (70 mM HEPES, 20 mM KCl, 1 mM EDTA, 1 mM DTT [pH 7.6]) along with 15 mM NADPH, 2.5 mM **1**, 10 mM glucose-6-phosphate, 10 units of glucose-6-phosphate dehydrogenase, and 10% D_2O. All samples were protected from light and air exposure by containment in amber NMR tubes flame-sealed under argon. Stock solutions of **1** were prepared in 10% D_2O/90% H_2O, and PULCON was used to determine the concentrations of stocks, relative to a tyrosine standard (110). All NMR experiments were conducted at 298 K on Varian spectrometers equipped with room temperature (500 MHz) or cryogenic (500 MHz and 700 MHz) probes. NMRPipe was used to process NMR data, and data visualization was accomplished with the combination of NMRDraw and NMRView (87, 88).

Resonance assignments – Standard triple-resonance experiments were used to complete the backbone and side-chain resonance assignments of E:NADPH:**1**. HNCACB, CBCA(CO)NH and HNCA experiments were used to assign the $^1H^N$, ^{15}N, $^{13}C^\alpha$, and $^{13}C^\beta$ resonances of the backbone (89). Residues that could not be assigned, likely due to chemical exchange, include W22, K38, T46, D87 and A145. Side-chain assignments for $^1H^\alpha$, $^1H^\beta$, and ^1H and ^{13}C methyl resonances were made using HBHA(CO)NH, (H)CCH$_3$-TOCSY, and HMBC (90, 91). Assignments from these experiments were sufficient for assigning the majority of protein-**1** NOEs. Stereospecific assignments of leucine and valine methyl groups were determined using the method of Neri and coworkers (92).

3.2.5. Relaxation Dispersion Analysis

^{15}N CPMG relaxation dispersion experiments were conducted on ^{15}N-labeled and highly deuterated (>80%) DHFR at 500 and 700 MHz using cryogenic probes. Collection and analysis of the data was completed as described previously (79). Residues undergoing slow timescale exchange can often move in a concerted fashion, with shared k_{ex} and p_A values. DHFR is known to possess ligand-independent motions at regions containing residues 127-134 and 155-159 (in addition to the 37% of non-proline backbone residues mentioned in later the text) (6, 79). Exchange at these residues was also identified in the current study, but they were excluded from global analysis of the data.

Relaxation dispersion global fitting – Due to the large number of residues experiencing μs-ms motion in E:NADPH:**1**, group fitting via the method of Mulder *et al.* was prohibitively impractical (30). Instead, all non-ligand-independent sites were fitted together. Several residues had a $\chi^2_{global}/\chi^2_{local}$ ratio of > 2; therefore, the local fit Δω value for such

residues is reported. The sign of $\Delta\omega$ was determined from peak positions in HMQC and HSQC spectra (111).

Procedure for determining data included in correlations of $\Delta\omega$ and $\Delta\delta$ – For sites lining the solution-preferred binding pose of the thiophenyl group undergoing slow motion (35-37, 40, 50-52, 54, and 57), residues 51 and 54 were considered to not respond significantly to the movement of the thiophenyl ring, given $\Delta\delta$ values of less than 0.4 ppm (51), and were excluded from the analysis. Residue 35 displayed a disagreement in sign for $\Delta\omega$ and $\Delta\delta$ and thus was excluded. However, because the difference in frequency of the peak in the HSQC relative to the HMQC is quite small in magnitude, the reported sign of $\Delta\omega$ may be reversed (111). While of the same sign, $\Delta\omega$ fitted for residue 36 was anomalously smaller than the calculated $\Delta\delta$. This residue was excluded, given the excellent correlation of the five residues that remained (37, 40, 50, 52, and 57). Similarly for the Met20 loop transition, residues with $\Delta\delta$ values less than 0.4 ppm (33 sites) were considered to not respond significantly to the closed-to-occluded transition and were excluded from the analysis (51). Residues suspected to be experiencing changes in chemical shift as a result of multiple conformational changes (i.e. a combination of Met20 loop, cofactor or inhibitor motions) were also further excluded from the analysis (6 sites). Several residues (27, 94, and 96) were initially thought to participate in this switching motion; however, upon sign determination for $\Delta\omega$, these residues no longer fell on the line of best fit – totaling 9 sites with complex motions.

3.2.6. Residual Dipolar Coupling Analysis

While the crystal structure suggests that the Met20 loop is more closed than occluded in nature, further evidence that the Met20 loop is closed in solution in E:NADPH:**1** was obtained by NMR. Structural perturbation of the protein backbone was assessed using N-H^N residual dipolar couplings (RDCs). As described previously, DHFR was partially aligned in 5% acrylamide via a 6 mm stretched gel alignment kit (79, 112). IPAP-HSQC experiments were collected on the anisotropic (gel) sample and on an isotropic sample prepared from the same ^{15}N-labeled protein stock solution. The data were processed and analyzed as described previously (79). $^1D_{NH}$ coupling values were compared to PDB IDs 3KFY, 1RX3, and 1RX5 to determine quality (Q) factors, excluding residues known to possess slow timescale motions (113).

RDC values for E:NADPH:**1** were compared to the crystal structures of E:NADPH:MTX and E:ddTHF. The Q-factor for comparing $^1D_{NH}$ values to 1RX3 (Met20 loop closed) was determined to be 0.42 while the comparison to 1RX5 (Met20 loop occluded) was 0.54, suggesting that the present ternary complex is more closed-like in solution. Comparing the $^1D_{NH}$ values for E:NADPH:**1** to its crystal structure (3KFY) led to a Q-factor of 0.40, similar to its agreement with 1RX3. The basis for the relatively high Q-factor is not entirely clear. The mild disagreement could be due to the quality of the alignment, differences between the crystal and solution, or the inherent dynamic nature of the complex.

3.2.7. Intermolecular NOE Analysis

The bound conformation of **1** in E:NADPH:**1** was determined using a 3D ^{13}C F$_1$-edited, F$_3$-filtered HMQC-NOESY experiment (114). This experiment provides

intermolecular NOEs between ^{13}C-labeled protein and unlabeled bound ligands. Interpretation was complicated by the presence of NOEs between the protein and both NADPH and **1**. A second NOESY spectrum was therefore also collected for the E:NADPH binary complex to make preliminary NOE assignments to cofactor. Chemical shift assignments for the bound protons of **1** were confirmed from a 2D ^{15}N,[13]C-filtered TOCSY experiment on a 1:1:1 complex of E:NADPH:**1** (115). There was no indication in the TOCSY or NOESY spectra of separate resonances for symmetric protons on the thiophenyl ring, consistent with symmetric ring flipping that is fast on the NMR timescale. Amino acids expected to be within 5-6 Å of **1** for pose A include F31, T35, V40, I50, L54, R57, and I94. Those nearest to pose B include I14, M20, T46, S49, I94, G95, and G96.

3.2.8. Protein Crystallization, Data Collection, and Refinement

Preparation of the ternary complex – Three- and 1.5-fold molar excesses of NADPH and **1**, respectively, were added to the apoenzyme when the concentration of DHFR was relatively dilute (~ 1 mg/mL). The ternary complex was then concentrated down to 30 mg/mL using a centrifugal concentration device.

Crystallization conditions – The ternary complex was crystallized via microseeding by the hanging drop vapor diffusion method in a 24-well crystallization plate under the following conditions: 30 mg/mL DHFR, 20 mM imidazole at pH 8, 350 mM $CaCl_2$, and 29% PEG-6000. The reservoirs of the plate contained 0.5 mL of mother liquor. Each hanging drop was a mixture of 5 μL of the reservoir solution and 5 μL of the prepared ternary complex in 20 mM imidazole. The crystals used in microseeding were grown under identical conditions. Crystals were allowed to grow at room temperature in the absence of light for 3-

5 days before harvesting. The high concentration of PEG-6000 in the mother liquor was sufficient for cryoprotection of the crystals. Upon addition of another 10 μL of the reservoir solution to each drop, mounted crystals were flash frozen in liquid nitrogen.

Data collection – Diffraction data were collected in-house at UNC using a RU300 rotating copper anode (Rigaku/MSC) and a Saturn 944+ CCD detector at ~100 K. Data were processed using HKL2000 (116).

Structure determination – The structure of E:NADPH:**1** was determined using molecular replacement. The CCP4 program suite and the MR program Phaser (117) was used. The search model was *E. coli* DHFR bound to $NADP^+$ in the C_2 space group (PDB ID 1RA9). It should be noted that the Met20 loop in the search model was not closed in conformation, reducing the bias to the final model for E:NADPH:**1**. Manual model building was accomplished using Coot (118). Final rounds of refinement used BUSTER (119). Initial placement of the ligands was accomplished by examination of the fo-fc difference densities. While electron density for the thiophenyl ring is very weak, the placement of the substituent is stereochemically sound and accounts for positive density seen in the fo-fc maps used and there is no other position in the maps that would account for the ring. The poor fits for the Met20 loop and the nicotinamide-ribose of NADPH could not be improved by repositioning, iterative omit maps trials with 2fo-fc or fo-fc difference maps. Atomic coordinates have been deposited in the PDB with ID 3KFY.

3.2.9. Molecular Docking Calculation

The Induced Fit Docking (IFD, Schrodinger, LLC) protocol (120) was employed to predict the possible binding orientations of **1** within the E:NADPH:**1** ternary complex. This

approach takes both ligand and receptor flexibility into account by combing rigid receptor docking (Glide) (121) with protein structure prediction (Prime) (122) methods in an iterative and exhaustive way. First, an ensemble of docking poses is generated into a rigid receptor using the softened potential. Second the "induced" protein conformations for each ligand pose are sampled effectively. At this point the algorithm considers side-chain flexibility and small-scale backbone motions within a 5 Å sphere of the co-crystallized ligand by default. Next the ligand is redocked into the low-energy induced-fit structures from the previous step. At the fourth step the protein/ligand complex is scored by accounting for both the docking energy (GlideScore), and receptor strain and solvation terms (Prime energy). In the end, if the gap in composite scores between top ranked structures is below 0.2 (nearly isoenergetic solutions), the entire IFD protocol is repeated for the top-ranked receptor structures from the first round of IFD as a starting point. During the calculation we employed the scoring function of the highest accuracy in Glide, the XP mode. No NOE data were used as restraints to guide our docking process.

Prior to the IFD calculation, the optimal protonation states for the ligand, receptor acidic/basic residues as well as histidine residues were determined. The protein's hydrogen bond network has been optimized by means of a systematic, cluster-based approach while a restrained minimization was conducted by allowing hydrogen atoms to be freely minimized as well as sufficient heavy-atom movement to relax strained bonds, angles, and steric clashes. We examined the positions of co-crystallized water molecules carefully before their removal and retained two water molecules (HOH13, HOH148) close to the quinazoline moiety of the inhibitor because similar positions were also observed for co-crystallized water molecules in other DHFR crystal structures.

3.2.10. k_{off} Determination

Stopped-flow fluorescence assays – A competitive binding assay, as described previously, was used to determine k_{off} for **1** from the E:NADPH:**1** complex (36). Briefly, E:NADPH:**1** (20 μM DHFR, 400 μM NADPH, and 200 μM **1** in NMR Buffer) was preformed and loaded into the drive syringe of the stopped-flow housing of a Fluorolog spectrofluorometer (Jobin Yvon Horiba, Inc).   Methotrexate (MTX) (500 μM in NMR Buffer) was loaded in a second syringe.   Intrinsic tryptophan fluorescence was excited at 290 nm while FRET emission (Trp to bound nicotinamide of NADPH) was monitored at 456 nm. Because MTX is a higher affinity inhibitor than **1**, upon rapid mixing via the stopped-flow apparatus, MTX displaces **1**, leading to a non-fluorescent ternary E:NADPH:MTX complex. The exponential decrease in fluorescence of E:NADPH:**1** to E:NADPH:MTX is fit to determine k_{off} for **1**. However, in the present experiment, no burst in FRET was observed upon mixing. This suggests that k_{off} for **1** is too slow to measure. However, it is also possible that **1**, being an excellent quencher of tryptophan fluorescence, forms a non-fluorescent ternary complex which cannot be distinguished from the non-fluorescent E:NADPH:MTX complex. Other inhibitors of DHFR with K_i values near 1 μM possess k_{off} values of less than 1 s^{-1}, and a series of inhibitors with widely varying binding affinities shows a strong correlation of increasing k_{off} with increasing K_i (see Chapter 4) (41). This suggests that **1** with a K_i of 120 nM would have a $k_{off} \ll 1$ s^{-1}, in agreement with our finding. By this, k_{on} is estimated to be ~10^6 s^{-1}.

3.3. Results

3.3.1. Compound 1 is a high-affinity, competitive inhibitor of DHFR

In studying a larger panel of ~10 DHFR inhibitors, 5-(4-chlorophenylthio)-quinazoline-2,4-diamine (compound **1**, Figure 3.1) was identified as exhibiting interesting NMR line-broadening properties when bound in a ternary complex with DHFR and NADPH (referred to as E:NADPH:**1**).
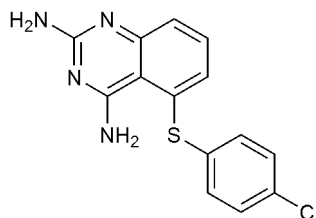
Figure 3.1. Structure of Compound **1** (5-(4-chlorophenylthio)-quinazoline-2,4-diamine).

The number and identity of sites experiencing line broadening differed greatly from that observed in the absence of **1** (E:NADPH) (79). Based on this, we decided to carry out a full structural and dynamic characterization of this complex. Compound **1** was previously identified as a competitive inhibitor of *E. coli* DHFR from a high-throughput screen of 50,000 small molecules (77). Using a competition assay, **1** was confirmed to competitively inhibit DHFR with a K_i of 120 ± 9 nM.

3.3.2. Structural evidence of multiple conformations in E:NADPH:1

DHFR is one of the most thoroughly studied enzymes from both a structural and dynamic point of view (6, 39, 42, 108). From these studies, it is known that the loops subdomain (Figure 3.2) is highly dynamic.

51
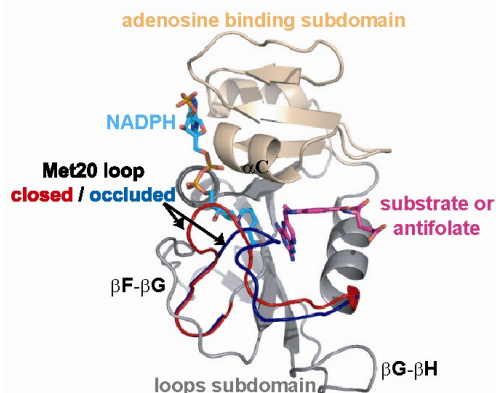
Figure 3.2. Structure of *E. coli* DHFR. Important subdomains, loops, and ligand binding sites are highlighted on a ternary complex of DHFR (PDB IDs 1RX3 and 1RX6 rendered using PyMOL.)

As DHFR progresses through its catalytic cycle, the enzyme undergoes a functionally important conformational change in its Met20 loop (residues 9-24) from the 'closed' state prior to hydride transfer, to the 'occluded' state following hydride transfer and leading up to product release (42, 108). Stabilizing hydrogen bonds between the Met20 and F-G (residues 116-132) loops within the closed state are broken as the Met20 loop transitions to form new hydrogen bonds with the G-H (residues 142-150) loop in the occluded state. In the occluded conformation, the side chains of M16 and E17 occupy the active site, forcing the nicotinamide of NADPH out into solvent.

The structure of E:NADPH:**1** in the $P2_12_12_1$ space group was determined to a resolution of 2.1 Å (Appendix 3.2). This structure is isomorphous to those determined previously (42), thus minimizing structural differences due to crystal packing artifacts and allowing for direct comparisons to be made. Overall, it is very similar to the methotrexate (MTX) ternary complex, PDB ID 1RX3 (backbone rmsd = 0.33 Å). However, some notable differences are observed relative to other ternary or closed complexes (42). While the Met20 loop is found primarily in the closed conformation (Figure 3.3A), electron density for some regions of the loop is quite poor, suggestive of mobility.
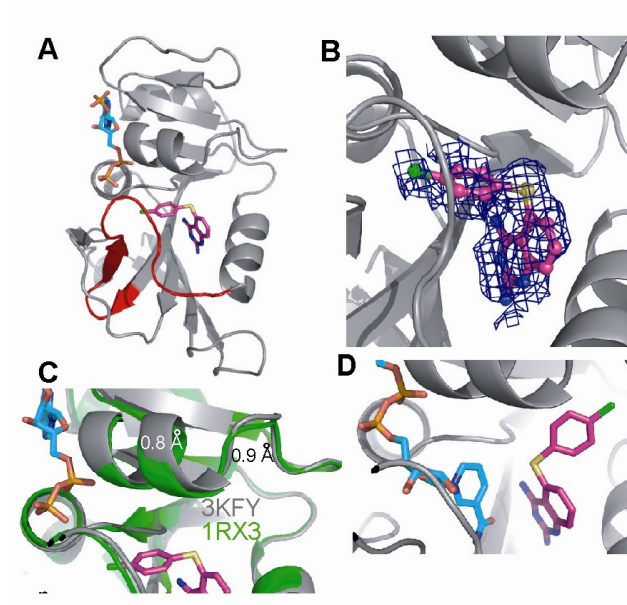
Figure 3.3. The crystal structure of E:NADPH:**1**. (A) The 2.1 Å resolution structure demonstrates that the Met20 loop is primarily in the closed conformation. NADPH is shown in cyan and **1** in magenta. (PDB ID 3KFY rendered using PyMOL.) (B) The $2\mathbf{F}_o$-$\mathbf{F}_c$ electron density for **1** is shown with a cover radius of 3 Å to remove extraneous electron density that complicates this view (pose B). Electron density on the 4-chlorophenyl group is a convolution of density of **1** and weak electron density of nicotinamide. (C) α-Helix C above the inhibitor binding site shifts away from the drug by approximately 1 Å in E:NADPH:**1** (grey) relative to 1RX3 (green). (D) NOE and chemical shift data suggest an alternative, ground state binding pose (pose A) for **1** in solution.

In fact, residues 16-20 fit poorly to the density observed (Figure 3.4A). Similarly, portions of NADPH and inhibitor have weak density, indicating that both cofactor and inhibitor sample multiple binding poses. Electron density for the 2,4-diaminoquinazoline moiety of **1** is well ordered, which overlays nicely with the corresponding moiety in MTX. However, the thiophenyl substituent is much less well defined (Figure 3.3B and 3.4B).
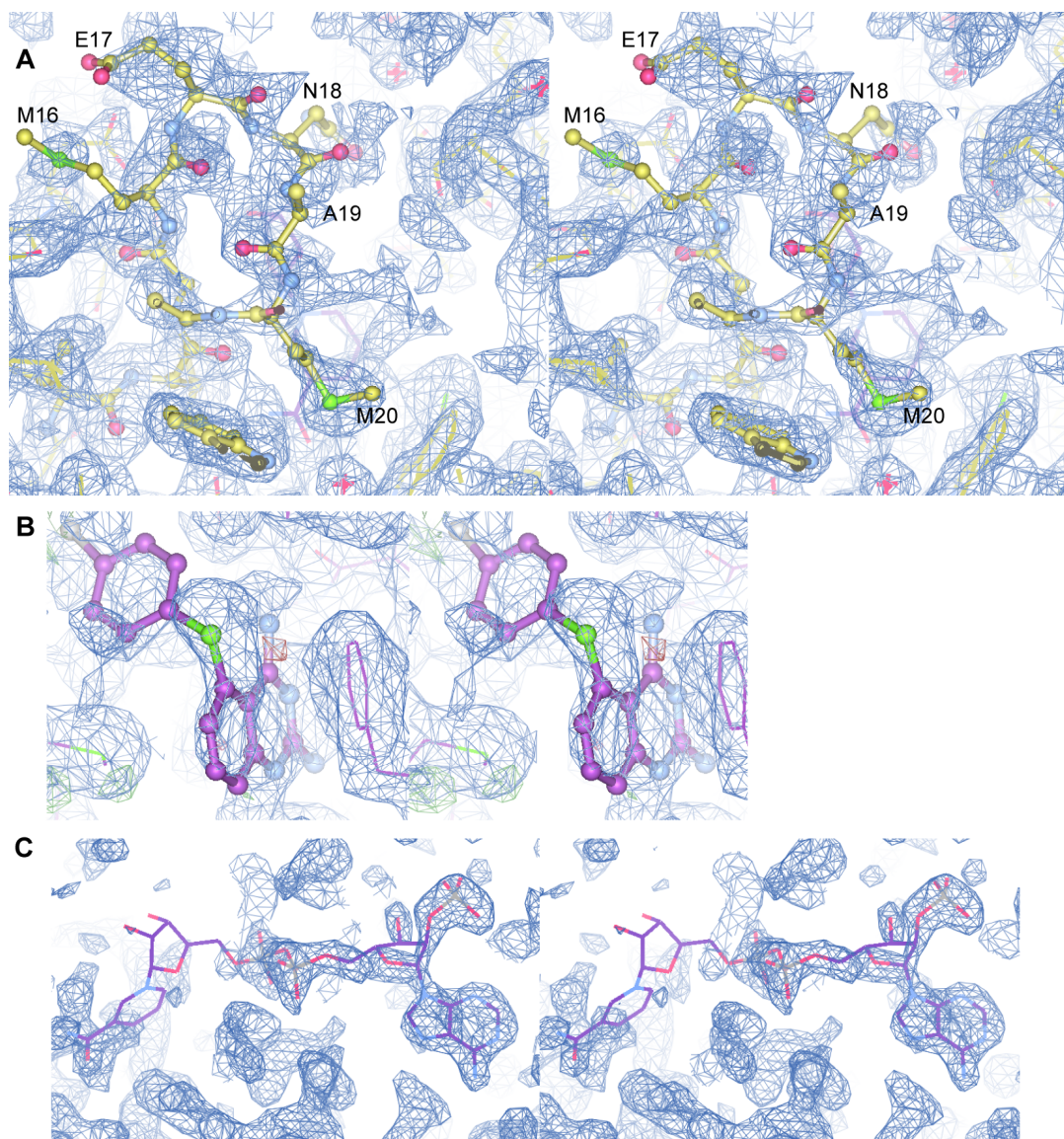
Figure 3.4. Electron density maps for the Met20 loop and bound ligands. (A) Residues 16-20 of the Met20 loop fit poorly to the observed density (shown in divergent stereo view). (B) Divergent stereo view of the electron density for **1**. (C) Well-ordered electron density is observed for the adenosine and pyrophosphate portion of NADPH; however, the density for the nicotinamide-ribose is much less well-defined.

Inspection of the density led to the only feasible conclusion, namely, that the thiophenyl group samples a previously unobserved pose for *E. coli* DHFR in which it is oriented towards the nicotinamide binding pocket of the active site (Figure 3.3A-B). Such a pose has been observed for an analogous inhibitor bound to *C. albicans* DHFR (123). The binding pose of

1 was studied further via induced fit docking (120) against the E:NADPH:**1** crystal structure, but with NADPH removed. The lowest energy docking pose observed shows the thiophenyl bound within the nicotinamide binding site (Figure 3.5A). A second thiophenyl pose is not observable from the electron density within the active site region, suggesting a sampling of an unknown number of additional poses.
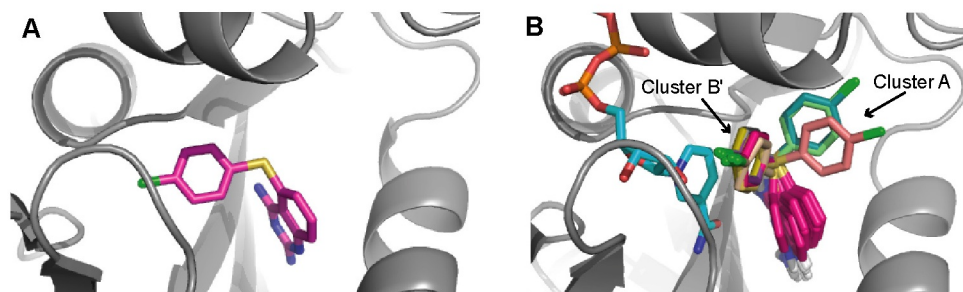
Figure 3.5. The outcome of Induced Fit Docking (IFD) of **1**. (A) The top-ranked docking pose of **1** in the absence of NADPH. Protein coordinates were taken from the starting E:NADPH:**1** crystal structure. (B) Ten top-ranked docking poses are illustrated in stick model, with quinazoline moiety in magenta and thiophenyl colored differently for each model. Protein coordinates were taken from the starting E:NADPH:**1** crystal structure and rendered as ribbon. Local structural changes to protein brought about by the IFD were omitted in both figures.

Consistent with **1** and cofactor sampling the same binding site, the nicotinamide-ribose moiety of NADPH samples multiple conformations. As mentioned above, poor electron density for nicotinamide-ribose is observed within the active site (Figure 3.4C). Surprisingly, electron density from both nicotinamide and thiophenyl groups overlay in this pocket, showing that the calculated density must result from the sum of different conformational poses within the crystal. Presumably, the nicotinamide-ribose group also samples a solvent exposed state, similar to that observed when the Met20 loop is occluded (e.g. bound to 5,10-dideazatetrahydrofolate) (42), to make room for the binding of **1**'s thiophenyl ring.

To add structural insight into the ambiguities within the crystal structure, NMR chemical shifts within the Met20 loop were analyzed. Nearly all residues within the Met20 loop are broadened, suggesting conformational exchange (Appendix 3.3); yet, the chemical shift values are indicative of a closed Met20 loop (Figure 3.6).
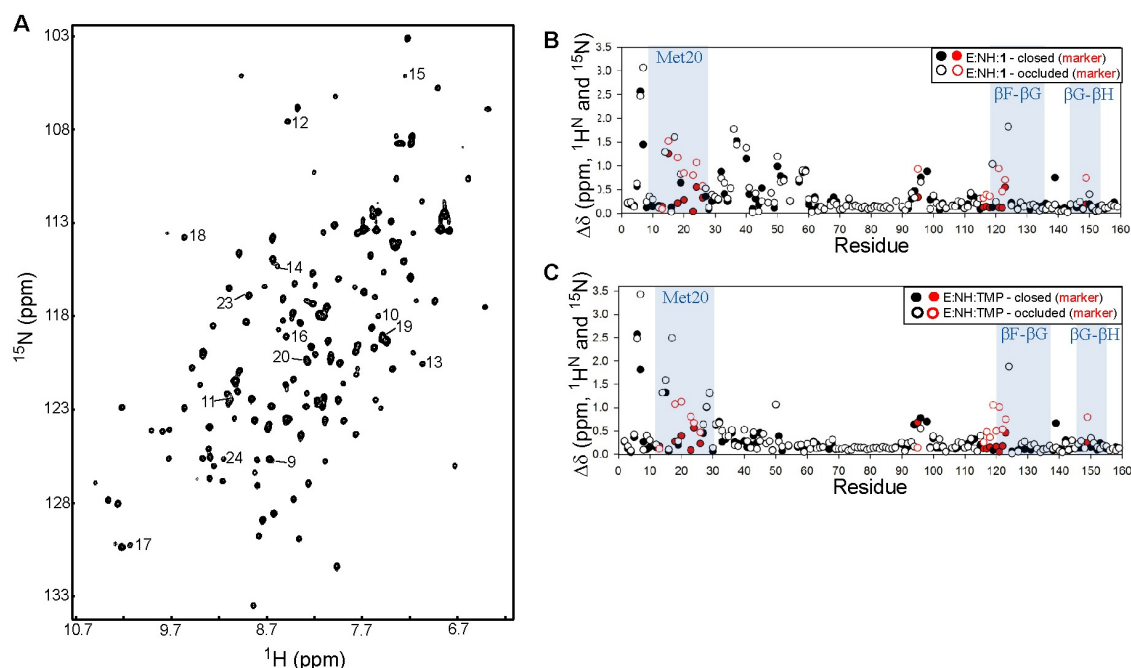
Figure 3.6. Chemical Shift Perturbations relative to closed and occluded chemical shifts. (A) ^{1}H-^{15}N HSQC of E:NADPH:**1** recorded at 700 MHz. Met20 loop resonances are labeled by residue number. In case of partial to complete overlap of resonances, lines are used to indicate resonance assignments. (B) CSPs of E:NADPH:**1** relative to Met20 closed and occluded shifts obtained from the BMRB suggest that all marker residues have chemical shifts more similar to a closed Met20 loop form, except V13. However, the difference between closed and occluded for V13 is very small (~0.06 ppm). Met20 loop conformation marker residues are shown in red. NADPH is abbreviated as NH. (C) Chemical shift perturbations of E:NADPH:TMP relative to Met20 closed and occluded shifts obtained from the BMRB. Met20 loop conformation marker residues are shown in red.

Chemical shift perturbations (CSPs) were calculated relative to model complexes with closed (E:NADP^{+}:folate, access. no. 5470) or occluded (E:5,6-dihydroNADPH:folate, access. no. 5471) loops, using data deposited in the Biological Magnetic Resonance Bank (BMRB). Of the nearly twenty resonances with ^{1}H^{N} and/or ^{15}N chemical shifts sensitive to the conformation of the Met20 loop (i.e. 'markers') (97), only V13 possessed a shift more

56

similar to an occluded loop conformation (Figure 3.6B). In other words, essentially all chemical shift markers indicate that the Met20 loop is primarily closed in E:NADPH:**1**. Furthermore, calculating CSPs for (E:NADPH:**1** – E:NADPH) and (E:NADPH:trimethoprim (TMP) – E:NADPH) allowed for the identification of site-specific changes elicited by the two inhibitors (Figure 3.7A).
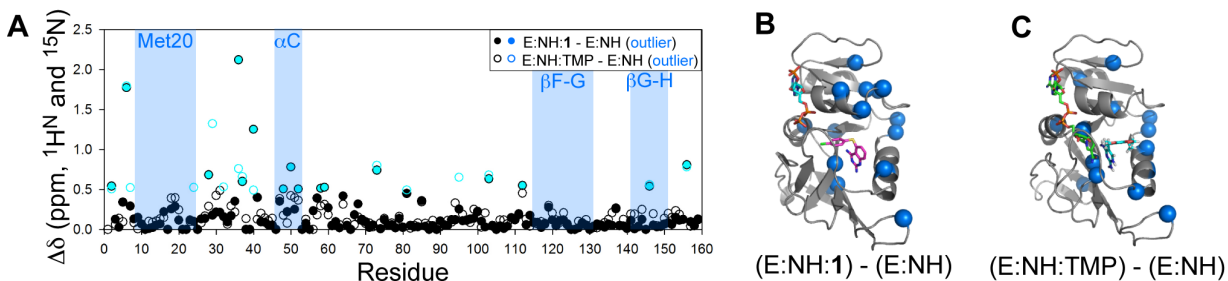
Figure 3.7. CSPs of Inhibitor Binding. (A) CSPs of E:NADPH:**1** and E:NADPH:TMP relative to E:NADPH. Outliers, shown in blue, were identified using a standard box plot function. (B) CSP outliers upon the binding of **1**, highlighted in blue spheres, do not localize to the Met20, F-G, or G-H loops. Significant CSPs are noted in α-helix C and β-sheet B above this helix, suggesting that thiophenyl could bind in this region. (C) Outliers upon the binding of TMP do not localize to the Met20, F-G, or G-H loops, nor to α-helix C or β-sheet B.

The Met20 loop of the E:NADPH holoenzyme complex is known to be predominantly closed in solution (6, 79). Relative to this closed complex, no significant changes in chemical shift were observed for any residues within the Met20 or F-G loops in the presence of either inhibitor (Figure 3.7B-C). The one outlier found in the G-H loop in binding both inhibitors is distal to the hydrogen bonds that form and break during Met20 loop switching motions. Since our previous analysis of the E:NADPH:TMP complex using residual dipolar couplings (RDCs) demonstrated that its Met20 loop is closed in solution, the current chemical shift comparisons indicate that the Met20 loop in E:NADPH:**1** is predominantly closed (79). This is further supported by measurements of RDCs for E:NADPH:**1** (mentioned in 3.2.6).

Interestingly, CSPs upon binding of **1** are seen above the inhibitor binding site, in the C-terminus of helix C and residues 40 and 41 of β-strand B (Figure 3.7B). Closer inspection of the crystal structure shows that, relative to E:NADPH:MTX, helix C is shifted about 1 Å away from the folate binding site (Figure 3.3C). In addition, significant CSPs upon binding **1** were not seen for the majority of residues lining the nicotinamide binding pocket. This raises the possibility of a preferred binding pose for the thiophenyl ring of **1** in solution, in which the substituent could be pointing toward α-helix C above the folate binding site (Figure 3.3D). Such a pose has been observed for an analog of **1** when bound to *C. albicans* DHFR (PDB ID 1IA2), in which the active site is several angstroms wider than in *E. coli* (124).

3.3.3. Intermolecular NOEs reveal the bound inhibitor conformation

Given the suggestion from CSPs of a solution-preferred orientation of **1** different from the crystal structure, a 3D ^{13}C-edited/filtered NOESY spectrum was collected on E:NADPH:**1** to obtain intermolecular NOEs and determine the solution conformation of **1** within the active site. Five bound ^{1}H chemical shifts of **1** (1-5 in Table 1) were observed to have NOEs to protein. 2D ^{15}N,^{13}C-filtered TOCSY showed that these five protons subdivided into two groups of *J*-coupled networks (Figure 3.8), corresponding to three signals for the quinazoline and two for the thiophenyl group (Table 1). Strong and medium intensity NOEs to the quinazoline moiety were consistent with the crystal structure, implicating ^{1}H(3), ^{1}H(4), and ^{1}H(5) signals as arising from quinazoline (Table 1).

	^{1}H(1)	^{1}H(2)	^{1}H(3)	^{1}H(4)	^{1}H(5)
DHFR ^{1}H					
A7 – ^{1}H$^\beta$	-	-	-	vw	-
M20 – ^{1}H$^\varepsilon$	vw	w	m	s	s
D27 – ^{1}H$^\beta$	-	-	-	w	-
^{1}H$^\alpha$	-	-	-	vw	-
L28 – ^{1}H$^{\delta 1}$	-	-	s	s	s
^{1}H$^{\delta 2}$	m	-	s	s	s
F31 – ^{1}H$^\beta$	w	w	-	w	-
T35 – ^{1}H$^{\gamma 2}$	w	w	-	w	-
M42 – ^{1}H$^\varepsilon$	m	w	-	-	-
I50 – ^{1}H$^{\delta 1}$	s	s	-	-	s
^{1}H$^{\gamma 2}$	s	m	-	-	-
L54 – ^{1}H$^{\delta 1}$	s	s	-	-	-
^{1}H$^{\delta 2}$	s	m	-	-	-
I94 – ^{1}H$^{\delta 1}$	m	m	-	-	-
^{1}H$^{\gamma 2}$	w	w	-	-	-

Table 1. Observed intermolecular NOEs for E:NADPH:**1**. Abbreviations: very weak (vw), weak (w), medium (m), and strong (s). Gray shading indicates residues expected to have medium to strong NOEs to protons on the quinazoline moiety of **1**. Bound chemical shifts of **1** (denoted 1-5) are 7.5, 7.1, 7.3, 6.93, and 6.88 ppm, respectively.
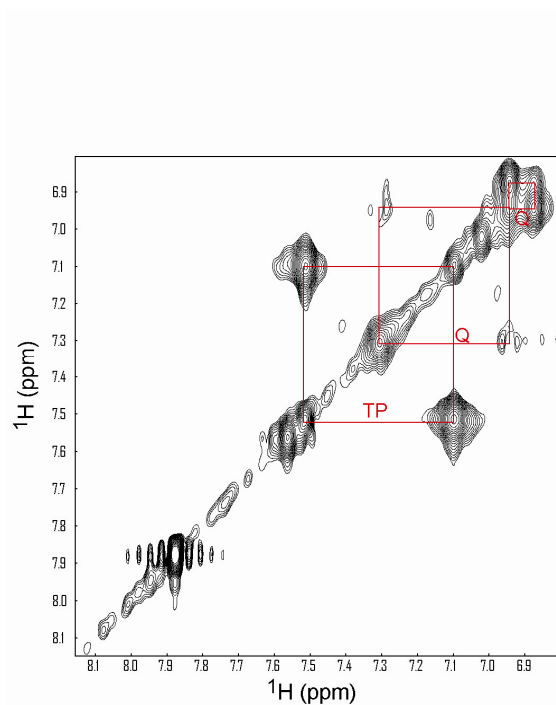
Figure 3.8. ^{15}N,^{13}C-filtered TOCSY spectrum of E:NADPH:**1**. The aromatic region of a 2D ^{15}N,^{13}C-filtered TOCSY experiment, in combination with the filtered NOE data, allowed for the determination of the chemically unique protons of bound **1** and to distinguish between thiophenyl (TP) and quinazoline (Q) protons.

For the thiophenyl substituent, two binding orientations were considered: (A) bound above the substrate binding site, directed towards α-helix C, as suggested by CSPs perturbations (Figure 3.3D), or (B) bound within the nicotinamide site, as observed in the crystal structure (Figure 3.3B). Amino acids expected to be within 5-6 Å of **1** in these two conformations were identified for poses A and B. No pose B residues were observed to have NOEs to **1**, except M20, whose side-chain is typically highly flexible (79). By contrast, five pose A residues showed mostly strong and medium NOEs to ^{1}H(1) and ^{1}H(2) (Table 1, non-shaded residues). This solidified the chemical shift assignments of **1** and strongly suggested that in solution the thiophenyl group exists primarily pointed in the direction of α-helix C (Figure 3.3D). Induced fit docking (120) against the E:NADPH:**1** crystal structure in the presence of NADPH shows binding pose A to be the lowest energy conformation for the thiophenyl ring (Figure 3.5B). The interproton distance patterns between receptor and the lowest energy docked conformation of **1** (Appendix 3.4) were found to agree well with most intermolecular NOEs in Table 1.

3.3.4. Extensive μs-ms motions in the E:NADPH:1 complex

What is the true nature of **1**'s side-chain orientation if it appears well-positioned in solution and disordered in the crystal form? Proteins exist in multiple conformations and thus there may be no single "correct" conformation for **1**. Protein motional dynamics occur over a broad range of timescales and include both small-scale bond rotations and large-scale conformational rearrangements (14, 125). The latter often occur on the "slow", or μs-ms timescale and have been implicated in the biological functions of proteins, including ligand binding and release, allosteric regulation, and catalysis-related events (6, 7, 51, 126). Indeed,

μs-ms dynamics are critical for movement of DHFR through its catalytic cycle (6). NMR relaxation studies of E:NADP$^+$:folate, proposed as a surrogate for the reactive complex of DHFR, have shown that the Met20 loop closed-to-occluded switching event occurs in solution on the μs-ms timescale (39, 51).

For the E:NADPH:**1** ternary complex, extensive μs-ms motion was detected by ^{15}N Carr-Purcell-Meiboom-Gill (CPMG)-relaxation dispersion experiments. These experiments allow for decomposition of the transverse relaxation rate R_2 into R_{ex}, the relaxation rate component due to slow timescale conformational exchange, and R_2^o, the remaining contributions to transverse relaxation on a faster timescale (27). Assuming a two-state exchange process, R_2 depends on the exchange rate constant (k_{ex}), the populations of ground state A and excited state B (p_A and p_B), and the difference in chemical shift between states A and B ($\Delta\omega$) (27). Thus, kinetic, thermodynamic, and structural information, respectively, are potentially obtained to describe the dynamic sampling of two states.

R_{ex} was identified at 55 residues in E:NADPH:**1** (Figures 3.9A-B). This is more extensive than any other reported complexes of DHFR. Motions are observed only on the front face of the enzyme, seen throughout the active site (folate + nicotinamide binding site) and at many residues within the Met20 (8 sites), F-G (6 sites), and G-H loops (4 sites), including G121 which is an important marker of Met20 loop conformational switching (51). All 55 sites were grouped together for global fitting, yielding shared k_{ex} and p_B values of 844 ± 59 s^{-1} and 2.6 ± 0.1 %, respectively (Appendix 3.5) (30). As will be described further below, the overall pattern of residues is consistent with two coupled motions: (i) switching of the thiophenyl group from preferred pose A above the substrate binding site (Figure 3.3D), as supported by NOEs, to alternative pose B observed in the crystal structure and (ii) switching

of the Met20 loop from closed to occluded, in order to accommodate the multiple poses of the inhibitor's thiophenyl moiety. This model of structural dynamics reconciles the X-ray and NMR data, suggesting that the crystal structure captures a minor, transient state for the thiophenyl ring, whereas the NOEs and chemical shifts reflect the major state in solution.
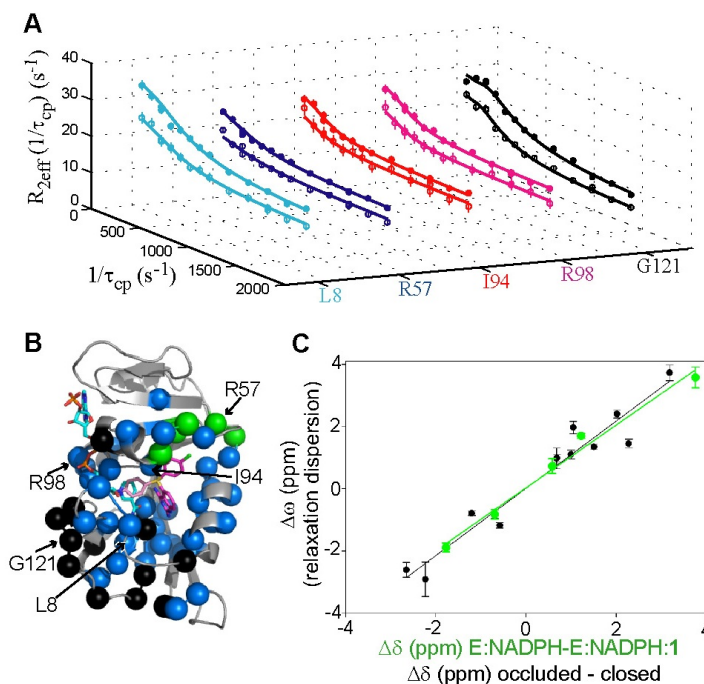
Figure 3.9. ^{15}N Relaxation Dispersion of E:NADPH:**1**. (A) Relaxation dispersion curves generated from 700 (closed circles) and 500 MHz (open circles) data are shown for several residues. Standard errors were determined by peak intensity analysis of duplicate experiments for specific $1/\tau_{cp}$ values. (B) Residues that exhibit R_2 dispersion are highlighted in colored spheres. NADPH and **1** are shown in cyan and magenta sticks, respectively. Thiophenyl poses A and B are shown as dark and faded sticks, respectively. (C) Sites surrounding the thiophenyl moiety of **1** show a linear correlation of $\Delta\omega$ to $\Delta\delta$ for the loss of thiophenyl in the excited state, with a slope of 1.01 and $R = 0.99$ (green correlation and spheres in (B)). The comparison of $\Delta\omega$ to $\Delta\delta$ for the sites participating in Met20 loop switching motion fit to a line with a slope of 1.08 and $R = 0.97$ (black correlation and spheres in (B)). Errors in $\Delta\omega$ were determined from Monte Carlo simulations in the global fitting procedure.

3.3.5. Concerted small-molecule and receptor conformational switching

In contrast to our previous study of DHFR dynamics in the presence of MTX and TMP (79), a number of residues surrounding the solution-preferred pose of **1**'s thiophenyl

group exhibit R_{ex}. These sites (residues 37, 40, 50, 52, and 57) were speculated to be undergoing exchange due to the switching of the thiophenyl from pose (A) above the substrate binding site to pose (B) within the nicotinamide binding site. Therefore, an analysis of chemical shift changes was undertaken. Dynamic chemical shift changes ($\Delta\omega$) from the relaxation dispersion analysis were plotted against changes in single-state chemical shifts ($\Delta\delta$). Values of $\Delta\delta$ representative of loss of inhibitor (E:NADPH – E:NADPH:**1**) for all residues experiencing slow motions were calculated using assignments of E:NADPH:**1** and E:NADPH. A correlation plot of $\Delta\omega$ and $\Delta\delta$ for 5 sites surrounding the thiophenyl group (green correlation in Figure 3.9C) yields a Pearson coefficient of 0.99, indicating a two-state motion of the thiophenyl from pose (A) in the ground state to a different pose in the excited state, likely pose B as is discussed below. We interpret these to be motions occurring while **1** is bound (i.e., not from dissociation) based on thermodynamic and kinetic grounds (see section 3.2.10), and also because residues surrounding the anchored quinazoline moiety do not show this correlation.

A similar chemical shift analysis was undertaken for the residues known to be markers of the closed-to-occluded transition of the Met20 loop (6, 51, 97). Values of $\Delta\delta$ for all residues experiencing slow motions were calculated using the deposited resonance assignments mentioned previously (E:DHNADPH:folate – E:NADP$^+$:folate) (97). The correlation of $\Delta\omega$ and $\Delta\delta$ for 13 sites (black correlation in Figure 3.9C) resulted in a Pearson coefficient of 0.97, indicating a concerted, two-state motion of the Met20 loop from closed to occluded in the E:NADPH:**1** ternary complex. Using the shared k_{ex} and p_B values from the global fit, the switching motion of the Met20 loop and the movement of the thiophenyl group away from pose (A) occurs at a forward rate (k_f) of 21.9 ± 1.6 s^{-1}. This rate translates into a

$\Delta G^\dagger_{\text{f}}$ of 15.6 kcal/mol, and an overall ΔG of 2.2 kcal/mol for the transition from ground to excited states, based on the populations. This value matches well with what has been observed previously by NMR for the transition, and also with what has been determined via simulation (127).

Because the two motions are coupled, we hypothesize that the excited state pose of the thiophenyl group is one in which it occupies the nicotinamide binding site (pose B). This pose was (i) observed in the crystal structure and is further supported by (ii) the poor electron density for both the nicotinamide of NADPH and the Met20 loop, (iii) the relaxation dispersion results, and (iv) induced fit docking of **1** to DHFR *in the absence of NADPH* (Figure 3.5A). The combination of these results strongly suggests that, in the excited state, the thiophenyl ring of **1** occupies the nicotinamide binding site. Regardless of the precise thiophenyl orientation in the excited state, it is clear that the binding of **1**, unlike MTX and TMP (79), drives reversible Met20 loop switching from the closed to the occluded conformation. Despite the fact that **1** is an inhibitor, from a mechanistic point of view **1** can be considered a 'dynamics agonist'. Upon binding (and thiophenyl insertion), **1** elicits a functional loop motion in a distal loop by competitively displacing nicotinamide, which allows adoption of the occluded conformation of the Met20 loop. Met20 loop motion was previously detected in E:NADP$^+$:folate (51); however, motion of folate was not observed. Direct observation of movement of a non-biological inhibitor while bound to its target has implications for drug design.

In summary, the E:NADPH:**1** complex is presented as a highly dynamic complex on the μs-ms timescale. Ligand, receptor, and cofactor are in a continuous state of shared conformational flux, with the ligand dynamics driving the cofactor and receptor dynamics.

The thiophenyl group of **1** prefers to bind at the upper end of the active site, but it also samples a higher energy pose in the nicotinamide binding pocket, which expels cofactor nicotinamide. This, in turn, allows the Met20 loop to move between closed and occluded conformations.

3.4. Discussion

Protein flexibility and dynamics represent a complication to drug design that has just begun to attract major efforts to tackle this problem. Although the problem is complex, one clear reason for this is that accurately characterized examples of receptor-ligand dynamics are needed from which to build upon, and such examples are essentially non-existent (5, 101). Here, we demonstrate that the ternary complex of DHFR, NADPH, and the drug-like compound **1** exists in at least two conformational states that are dynamically interconverting on a timescale of ~1 ms. The structural, temporal, and population aspects of the dynamics were captured by use of crystallography and NMR. This complex could therefore serve as a useful benchmark for the refinement and future development of modeling methods that incorporate receptor and ligand dynamics. This should lead to improvements in predicting binding affinities and provide insight into targeting dynamics (103).

The application of both NMR and crystallography was critical to reveal the true nature of this ligand-receptor complex. The resultant picture of this dynamic complex is that, in solution, the dominant state (~97%) has DHFR in the closed conformation, with cofactor fully bound and thiophenyl of **1** directed towards helix C. The minor state (~3%) has DHFR in the occluded conformation, nicotinamide-ribose of cofactor ejected into solvent, and thiophenyl inserted into the nicotinamide binding site. These states represent actual

65

dynamics within the complex since dissociation is slow relative to these conformational changes. Ligand structural heterogeneity has been observed previously in *E. coli* DHFR complexes. A recent ternary crystal structure of DHFR complexed with a novel inhibitor (K_i = 11 nM) showed the inhibitor with diminished electron density for half of the molecule (43). A second structure with a shorter inhibitor corresponding to the anchored region of the first inhibitor also showed evidence for multiple conformations. The second inhibitor has substantially reduced affinity, showing that even flexible portions of ligands can make large contributions to binding affinity (43).

Despite the motion of this small molecule while bound to DHFR, the binding affinity of **1** for holoenzyme is still high. Do the multiple binding poses of **1** limit its clinical potential? It may be possible for drug resistant mutations to limit one binding pose while not affecting the other. Thus, two dynamically sampled ligand binding poses for one drug could limit drug resistance if protein inhibition is preserved in either binding mode. This was specifically observed in crystal structures of inhibitor TMC278 (rilpiverine) in complex with HIV-1 reverse transcriptase mutants (128). In principle, **1** would be valuable as an inhibitor of trimethoprim (TMP) resistant strains of bacteria due to its sampling of a non-canonical binding pose within the active site. Known mutations that confer TMP resistance would not affect the binding of the thiophenyl substituent of **1** within the nicotinamide binding site, as many of these mutations are concentrated in the folate binding site (76).

The findings reported here, along with innumerable crystallographic studies, suggest that multiple ligand poses may be sampled more often than expected (11, 101). This may be especially true for small, lipophilic ligands encountered in drug discovery. In most instances of apparent single-mode binding, minor conformers that are actually sampled to a significant

66

extent would not be expected to crystallize or would lie below the noise threshold for NOE detection; the only way to detect these conformers would be from NMR relaxation dispersion experiments (as reported here) or MD simulations (129, 130). An important class of receptors for signal transduction and pharmaceuticals is that of the ligand activated G-protein coupled receptors (GPCRs). The degree of conformational flexibility and dynamics in these receptors is impressive (131) and likely to be more extensive than in DHFR. Germane to the results here, biophysical studies on the β2-adrenergic receptor (β2AR) show that agonist binding (at saturating levels) produces structural heterogeneity (132), rather than locking the receptor into a single conformation. Thus, although it remains to be seen if single GPCR *ligands* adopt multiple bound configurations, dynamic receptor-ligand complexes are likely to be of broad relevance for understanding mechanisms of signal transduction and their perturbation by drugs (102).

It is instructive to compare the dynamic characterization here to one of the only other target-drug systems characterized in detail by crystallography and NMR: the Bcr-Abl fusion kinase in complex with the kinase inhibitor dasatinib (133). Dramatic line-broadening was observed in the activation and P-loops of Bcr-Abl, suggesting allosteric loop switching motions. Even though inhibitors imatinib and nilotinib stabilize different loop conformations, they also show some line-broadening in a few loops residues, although significantly less than in the dasatinib complex (133). Further detail on the μs-ms timescale dynamics from relaxation dispersion experiments were not available. We also note that dynamics in a small molecule was previously shown to exist on multiple timescales when bound to matrix metalloproteinease-1 (MMP-1) (82). Thus, dynamics in both ligands and receptors clearly exist across very different classes of drug targets.

It has recently been suggested that many underexploited protein target classes are avoided due to the flexibility inherent to their function, such as ion channels and nuclear hormone receptors (5). However, these more challenging targets are likely to become important in future drug design efforts, as we continue to exhaust the less complex targets. Identification of multiple ligand conformations and flexibility within the active site for the E:NADPH:**1** complex is an example that stresses the importance of continuing efforts toward an understanding of protein dynamics and how they are modulated by small molecules. Given the scarcity of studies identifying specific ligand-induced protein flexibility, the results of this study may find use in the advancement of computational docking methods that include protein dynamics (100). The transient, excited states detected in this approach could also be targeted and stabilized by small molecules, leading to new high-affinity modulators of protein function for disease treatment.

Chapter 4

Evidence for Dynamic Motion in Proteins as a Mechanism for Ligand

Dissociation

4.1. Introduction

A long-sought goal in the biochemistry of receptor-ligand interactions is to gain an understanding of what molecular forces contribute to binding affinity and kinetics. A fundamental question is how does dissociation occur once a ligand (e.g., peptide or small molecule) is bound to its receptor? One model for dissociation is simple diffusion of ligand from the target. A more mechanistic reasoning would be that something happens to physically disrupt the interaction between ligand and receptor, leading to ligand release or ejection. Indeed, myoglobin requires structural deformations to bind and release oxygen (134, 135); however, this can be viewed as a special case since ligand is completely buried from solvent. We postulate that protein structural fluctuations could be a more generally utilized mechanism for weakening intermolecular interactions and effectively "pushing" or "shearing" a ligand away from its receptor. Experimental studies towards this question should benefit structure-based drug design and protein (enzyme) engineering. From a biological perspective, because signal transduction is driven by countless cycles of ligand binding and release (136), insight into mechanisms of ligand release mechanisms could also

make possible the drawing of fundamental connections between internal protein dynamics and cell signaling.

To probe the intra- and intermolecular dynamics of protein and small molecule inhibitor complexes, we took a medicinal chemistry approach to relate basic ligand binding properties to dynamic motion in these complexes. Enzymes are common pharmaceutical targets and exhibit considerable dynamics that are amenable to characterization by NMR relaxation dispersion (6, 137-141). We characterized *E. coli* dihydrofolate reductase (DHFR) in complex with eight different antifolate inhibitors (three reported previously) spanning an affinity range of six orders of magnitude (40, 79). Five tetrahydroquinazoline inhibitors were designed to bind with reduced affinity for the purpose of loosening the ligands to allow detection of rare motions related to ligand dissociation. Different levels of switching motion on the μs-ms timescale were observed in each complex, although a cluster of residues around the active site exhibits identical motion in all eight of the complexes. From the analysis of relaxation dispersion curves, the kinetics of conformational switching in DHFR were found to scale with both K_i and k_{off}, though the conformational switching was always faster than k_{off}. These data implicate a common dynamic mechanism for ejection of ligands within this series, and suggest that internal protein motion may be a critical event for ligand dissociation in general. The medicinal chemistry approach taken allows focused and methodical perturbations within the active site; this is in stark contrast to global systematic perturbations such as temperature variations or the addition of chemical denaturants. Recent studies have linked conformational dynamics with catalytic timescales through coincidental values of rate constants (6, 7). We show here – through use of a ligand series – that linkage can also be made for events on different timescales.

4.2. Materials and Methods

4.2.1. Synthesis of the tetrahydroquinazoline series

Compound **3** (6-methyl-5,6,7,8-tetrahydroquinazoline-2,4-diamine) was prepared by a one-step condensation reaction, similar to that described previously (142). Briefly, dicyandiamide (10.19 g, 0.12 moles) and 4-methylcyclohexanone (11.33 g, 0.10 moles) were combined in a round bottom flask fitted with a Dean-Stark trap and a condenser. The reaction was heated in an oil bath at 180 °C for three hours. Boiling water was added to the reaction as it was transferred to a separatory funnel for extraction. The desired compound was extracted from the aqueous layer with hot chloroform. The chloroform washes were dried over anhydrous magnesium sulfate before solvent was removed via rotary evaporation. A golden yellow liquid with white precipitate remained. Additional white solid was precipitated via addition of hexanes to the yellow liquid. The solid was isolated via filtration.

Similarly to **3**, compounds **4** and **6** (7- or 5-methyl-5,6,7,8-tetrahydroquinazoline-2,4-diamine, respectively) were prepared from dicyandiamide (10.19 g, 0.12 moles) and 3-methylcyclohexanone (11.33 g, 0.10 moles). Reverse-phase HPLC purification using a water and acetonitrile buffer system was used to separate the two products. A combination of very small volumes of the mixture loaded per run along with a very shallow acetonitrile gradient was useful in accomplishing the separation. To avoid isolation of a TFA-salt of each compound, NaOH base was added to the separate compound pools and each was treated with hot chloroform to extract the compounds free of TFA, which remains in the water layer. Extracts were dried over sodium sulfate and rotary evaporation was used to remove the chloroform to yield white powders for each compound. A standard 2D ^{1}H-^{1}H NOESY

experiment was used to distinguish between the two methyl products: only in **6** would

NOESY cross peaks between the methyl protons and the amine protons be observed. In

addition, the benzylic methine proton of **6** would be expected to be shifted further downfield

(~2.7 ppm) than the methine of **4** (~1.3 ppm).

Analogously, **2** and **5** (8-methyl- and 5,6,7,8-tetrahydroquinazoline-2,4-diamine,

respectively) were prepared from the combination of dicyandiamide (10.19 g, 0.12 moles)

and 2-methylcyclohexanone (11.33 g, 0.10 moles) or cyclohexanone (9.91 g, 0.10 moles).

The compounds were purified via HPLC and isolated via chloroform extraction to yield

white powders. Spectroscopic data for all five compounds is summarized in Appendix 4.1.

4.2.2. K_i determination

As described previously (section 3.2.3), biochemical competition assays using a 96-

well plate reader were used to determine the inhibition constant (K_i) for **2-6** (40, 77). The

decrease in absorbance at 340 nm was monitored over time in a 2D titration of inhibitor and

substrate.

4.2.3. Protein expression and purification

Isotopically labeled wild-type *E. coli* DHFR was over-expressed and purified as

described previously (section 2.2.1) (79). Purified apo-DHFR was flash frozen, lyophilized,

and stored in a desiccator at 4 °C until use.

4.2.4. NMR Spectroscopy

For ternary inhibitor complexes, samples contained 1 mM DHFR in NMR buffer (70 mM HEPES, 20 mM KCl, 1 mM EDTA, 1 mM DTT [pH 7.6]), 15 mM NADPH, 2.5-10 mM antifolate (E:NADPH:**2** – 10 mM; E:NADPH:**3** – 2.5 mM, E:NADPH:**4** – 8-10 mM; E:NADPH:**5** – 10 mM; E:NADPH:**6** – 10 mM), 10 mM glucose-6-phosphate, 10 U glucose-6-phosphate dehydrogenase, and 10% D2O for spectrometer locking purposes. All samples were protected from light and air exposure by containment in amber NMR tubes flame-sealed under argon. Stock solutions of **2-6** were prepared in 10% D_2O/H_2O and PULCON was used to determined the concentration of each stock, relative to either valine or trimethoprim standards (110). NMR experiments were performed as described previously, using both room temperature (500, 600, and 700 MHz) and cryogenic (500 and 700 MHz) probes (40, 79). NMRPipe was used to process NMR data, and data visualization was accomplished with the combination of NMRDraw and NMRView (87, 88).

Resonance assignments – Standard triple-resonance experiments were used to assign the backbone of the ternary complexes with compounds **3**, **4**, and **5**. E:NADPH:**2** and E:NADPH:**6** assignments were contingent upon knowledge of the first three ternary complexes. Specifically, HNCACB and CBCA(CO)NH experiments collected at 700 MHz allowed for the assignment of $^1H^N$, ^{15}N, $^{13}C_\alpha$, and $^{13}C_\beta$ resonances in these complexes (89). Common residues that could not be assigned include K38, T46, D87, and A145.

Chemical shift perturbations (CSPs) – To demonstrate that the solution conformation of the Met20 loop in each of the five complexes is predominantly closed, the approach described previously was used(40), in which CSPs were calculated for each complex relative to model Met20 loop closed (E:NADP$^+$:folate, BMRB access. no. 5470) and occluded (E:5,6-dihydroNADPH:folate, BMRB access. no. 5471) chemical shifts (97). Of the ~20

resonances considered makers for the conformation of the Met20 loop in $^1H^N$ and/or ^{15}N, all except V13 and I94 have chemical shifts more similar to a Met20 loop closed conformation (Fig. 4.4) consistent with our previously analysis of E:NADPH:**1** (40).

Site-specific chemical shift perturbations (CSPs) that result upon binding of each inhibitor (E:NADPH:antifolate – E:NADPH) confirm the ligand orientations observed in the crystal structures. The five inhibitors elicit both similar magnitudes of perturbations and patterns of residues affected (Fig. 4.5a), with mild differences observed due to the specific location of the methyl substituent on the THQ ring. Using a box plot function, outlying CSPs were identified on a per residue basis for each inhibitor (Fig. 4.5b). The majority of outliers are the same amongst the five ternary complexes, with one unique outlier in each complex due to the positioning of the methyl substituent (**2** – F31, **3** – I50, and **4** – F31). Additionally, one residue in each complex (light blue spheres in Fig. 4.5b) shows a perturbation in chemical shift, although not considered an outlier (**2** – A29, **3** – G51, **4** – T35, and **6** – I94 is split in two). E:NADPH:**5** does not possess any unique outliers, which is not surprising as it lacks a methyl substituent. The splitting of I94 in the presence of **6** may be due to switching motions of the protein and/or small molecule, or may also be due to the binding of both enantiomers of **6**.

4.2.5. Relaxation dispersion analysis

^{15}N CPMG relaxation dispersion experiments were conducted on highly deuterated (>80%) DHFR for the E:NADPH:**2** and **4-6** complexes while protonated DHFR was used for E:NADPH:**3**. Complexes with bound **2-4** were examined using a TROSY relaxation dispersion experiment at 700 MHz with a room temperature probe. Data collection at 700

74

MHz for complexes with bound **5-6** utilized a cryogenic probe and the regular non-TROSY experiment. Collection and analysis of the data was completed as described previously (40, 79).

As mentioned above, protonated DHFR was used for relaxation dispersion experiments on E:NADPH:**3**. At the time this data was collected, deuteration was not a common technique used in our lab, and the data from using protonated protein was deemed sufficient for analysis and not recollected using deuteration. It is possible, however, that additional residues with R_{ex} would be detected in E:NADPH:**3** if highly deuterated protein were to be used in preparation of the complex. This could explain why an increase in the number of sites with slow motion is not seen in E:NADPH:**3** relative to E:NADPH:MTX or E:NADPH:TMP (79).

Residues undergoing slow timescale exchange can often move together, or in a concerted fashion, with shared k_{ex} and p_A values. Aside from the residues used in group fitting (described below), DHFR is known to possess ligand-independent motions at regions containing residues 128-134 and 154-159 (30). Exchange at these residues was also identified in the current study, but the sites were excluded from global analysis of the data. These C-terminal residues have been group fitted together, and indeed prove to be ligand-independent in the case of bound inhibitors, as k_{ex} and p_A are identical for all complexes studied (Appendix 4.10).

For global fittings, all residues exhibiting slow motion (excluding the C-terminal residues) were grouped together. Residues found to have a significantly improved local fit relative to the global fit (i.e., having a $\chi^2_{global}/\chi^2_{local}$ ratio of >2) are reported with local $\Delta\omega$ values. In the case of E:NADPH:**2** and E:NADPH:**4**, global fits of all residues together

would not converge. Upon removal of four residues with increased local k_{ex} values (37, 50, 54, and 58), group fitting for E:NADPH:**4** converged and the residues appeared to fit together based on χ^2 ratios. This same approach for E:NADPH:**2** resulted in convergence (40, 44, 48, 50, 54, 57, 98, 115, and 119 removed); however, the residues did not group well together based on χ^2 ratios. Group fits for complexes with bound **2** and **4** are reported, but it should be noted that the fits were not conducted in the same fashion as for the rest of the series. One interesting point to mention is that E:NADPH:**2** and E:NADPH:**4** resulted in equivalent group fitting for both the 'slow' and 'fast' moving sets of residues. We speculate that the structural similarity of these two inhibitors may underlie why they appear to cause faster switching motions in DHFR. Also, the possibility that both *R* and *S* enantiomers of these two inhibitor bind could also result in different switching than for the remainder of the series.

The increased number of residues experiencing backbone conformational exchange in the E:NADPH:**6** complex are due in part to suspected motion of the Met20 loop. Several residues within the F-G and G-H loops known to undergo reliable changes in chemical shift upon switching of the loop from closed to occluded have been observed to possess slow timescale motion in the presence of **6** (Fig. 4.8). Although a crystal structure for E:NADPH:**6** has not been determined, the structure of E:NADPH:**3** serves as an excellent model (Fig. 4.3a). If one envisions the methyl group positioned on C5 (instead of C6 in the structure), the methyl group likely comes within steric contact of the nicotinamide of NADPH in the active site. Unlike the switching motion of **1** characterized previously (40), the methyl group on C5 does not sample an alternate binding pose that differs enough to move the group away from nicotinamide. This proposed steric clash between nicotinamide

and the methyl group on C5 likely accounts for the significant reduction in binding affinity for **6** relative to the other tetrahydroquinazoline compounds.

The sign of $\Delta\omega$ was determined from peak positions in HSQC and HMQC spectra (111). Sign determination for $\Delta\omega$ was completed on six of the eight ternary complexes (E:NADPH:**2** and E:NADPH:**4** excluded). Given the strong pattern of $\Delta\omega$ sign observed for the antifolate consensus residues (Fig. 4.11a), the signs for the complexes with **2** and **4** were assumed to agree with the pattern. Additionally, the sign of $\Delta\omega$ determined for the three other THQ compounds (**3**, **5-6**) should be representative of **2** and **4**. Fitted parameters and the sign of $\Delta\omega$ are summarized for each complex in Appendices 4.5-4.9.

In order to compare to the average $\Delta\omega$ values fitted for the consensus antifolate residues with R_{ex}, the sign of $\Delta\omega$ was determined for the E:NADPH holoenzyme complex, as it has not been previously reported by Wright and colleagues (6). In Figure 4.12, we report the sign for three sites in E:NADPH in comparison to our data on the current series of inhibitors. The sign for D11 is not reported for E:NADPH because we have been unable to assign that residue.

4.2.6. Protein crystallization, data collection and structure determination

Crystals of E:NADPH:**3**, E:NADPH:**4**, and E:NADPH:**5** were grown using similar conditions as described previously (40, 42, 43).

Crystallization conditions – For all three complexes, NADPH and inhibitor were present at three-fold molar excess relative to the concentration of DHFR. Briefly, E:NADPH:**3** was crystallized via the hanging drop vapor diffusion method under the following conditions: 20 mg/mL DHFR, 20 mM imidazole at pH 8, 300 mM $CaCl_2$, and 30% PEG-6000. E:NADPH:**4** was crystallized via the hanging drop vapor diffusion method

under the following conditions: 20 mg/mL DHFR, 20 mM imidazole at pH 8, 325 mM CaCl$_2$, and 34% PEG-6000. E:NADPH:**5** was crystallized via the sitting drop vapor diffusion method under the following conditions: 10 mg/mL DHFR, 20 mM imidazole at pH 8, 325 mM CaCl$_2$, and 34% PEG-6000. Each hanging or sitting drop was a mixture of 5 μL mother liquor and 5 μL of the prepared ternary complex in 20 mM imidazole. Crystals were allowed to grow at room temperature for several days before harvesting. The mother liquor contained a high concentration of PEG-6000, which was sufficient as a cryoprotectant. To mount the crystals, 10 μL of mother liquor was added to the hanging or sitting drops. Mounted crystals were flash frozen in liquid nitrogen.

Data collection – Diffraction data were collected in-house at UNC using a RU300 rotating copper anode (Rigaku/MSC) and Saturn 944+ CCD detector at ~100 K. Data were processed using HKL2000 (116).

Structure determination – All three structures were determined using molecular replacement methods. The CCP4 program suite and the MR program Phaser was used (117). The search model was *E. coli* DHFR bound to NADP$^+$ in the C_2 space group (PDB code 1RA9). This search model did not possess a Met20 loop closed conformation. Manual model building was accomplished using Coot (118). Final rounds of refinement used BUSTER and MOSFLM (119, 143). The placement of ligands was accomplished via examination of fo-fc difference maps generated in the absence of ligand. Atomic coordinates have been deposited in the PDB under access code 3R33, 3QYL, and 3QYO.

4.2.7. Determination of k_{off}

A stopped-flow fluorescence competitive binding assay, as described previously (section 3.2.10), was used to determine k_{off} for **2-6** from the E:NADPH holoenzyme (36, 40). Briefly, E:NADPH:antifolate (20 μM DHFR, 400 μM NADPH, and 200 μM antifolate in NMR Buffer) was preformed and loaded into the drive syringe of the stopped-flow housing of a Fluorolog spectrofluorometer (Jobin Yvon Horiba, Inc). Methotrexate (MTX) (400 μM in NMR Buffer) was loaded in a second syringe.   Intrinsic tryptophan fluorescence was excited at 290 nm while FRET emission (Trp to bound nicotinamide of NADPH) was monitored at 427 nm. Because MTX is a higher affinity inhibitor than **2-6**, upon rapid mixing via the stopped-flow apparatus, MTX displaces **2-6**, leading to a non-fluorescent ternary E:NADPH:MTX complex. The exponential decrease in fluorescence of E:NADPH:inhibitor to E:NADPH:MTX is fit to determine k_{off} for **2-6** (Fig. 4.1) (36). The experiments were repeated at a second MTX concentration (600 μM), as k_{off} is independent of the concentration of the trapping ligand. The reported k_{off} values are the average of multiple runs at both MTX concentrations. Reported errors are the standard deviations of all runs.
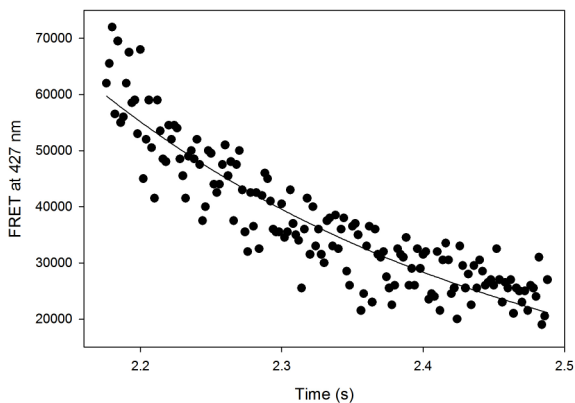
Figure 4.1. Sample exponential decay curve from stopped-flow fluorescence experiments.

4.3. Results

4.3.1. A series of structurally similar antifolates covers a range of K_i and k_{off}

When studying the dynamics of DHFR in the presence of the high affinity ($K_i \leq 1$ nM) inhibitors methotrexate (MTX) and trimethoprim (TMP) (Fig. 4.2c), it was found that both inhibitors elicited essentially identical patterns of slow motion in the enzyme (79). We wondered whether that same pattern of dynamics would be observed for any bound inhibitor to the same site, regardless of binding affinity or chemical structure. To address this question, a series of substrate-competitive DHFR inhibitors, or antifolates (compounds **2-6**), with K_i values greater than 1 nM were chosen to study while bound to the holoenzyme (Fig. 4.2a).
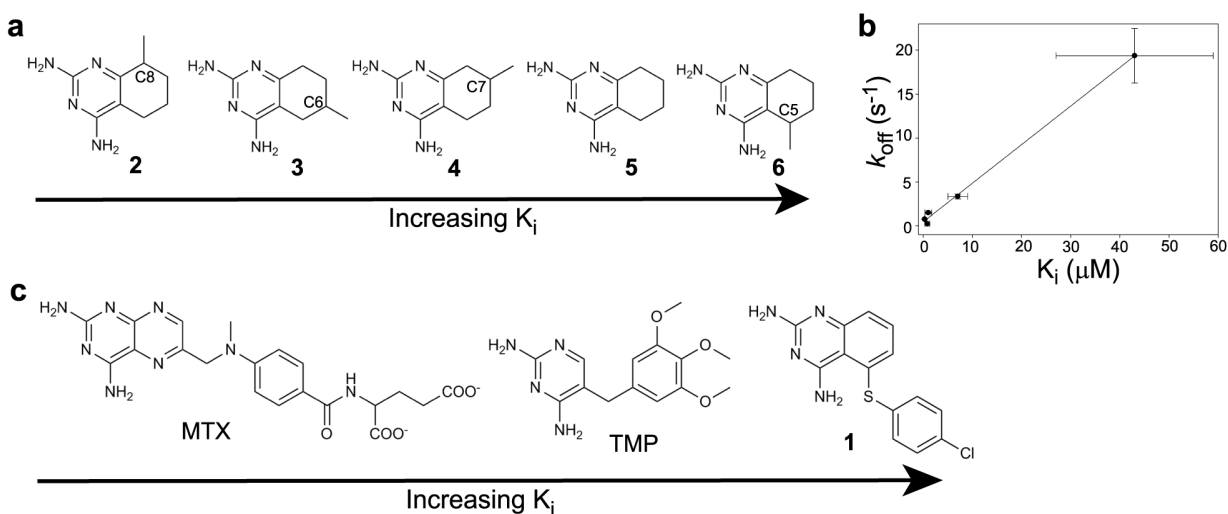
Figure 4.2. The series of reduced-affinity and previously characterized antifolates. (a) Chemical structures of the reduced-affinity antifolates. (b) The relationship between k_{off} and K_i for the series of reduced-affinity antifolates ($R = 0.99$). (c) Chemical structures of the previously characterized antifolates – methotrexate, trimethoprim, and **1**.

This series of five tetrahydroquinazoline-2,4,-diamine compounds is highly homologous. Compounds **2**, **3**, **4**, and **6** are constitutional isomers and differ only in the placement of the

methyl substituent on the tetrahydroquinazoline (THQ) ring. Inhibitor **5** lacks the methyl

substituent entirely, but it serves as a reference in that it is not a racemic mixture.

Compounds **3** and **4** were identified as competitive inhibitors of DHFR from a high-

throughput screen of 50,000 small molecules (77). To complement these two reduced-

affinity antifolates, the previously unstudied compounds **2**, **5**, and **6** were synthesized. We

postulated that **2**, **5**, and **6** would have K_i values similar to those published for **3** and **4** on the

basis of structural similarity.

Cmpd	K_i (μM)	k_{off} (s^{-1})
2	0.3 ± 0.03	0.76 ± 0.05
3	0.8 ± 0.5	0.23 ± 0.01
4	1 ± 0.7	1.49 ± 0.08
5	7 ± 2	3.35 ± 0.27
6	43 ± 16	19.37 ± 3.11

Table 1. Binding affinities and kinetic off-rates for the series of THQ antifolates.

K_i values for the inhibitors were determined to confirm the previously determined

values and establish values for the new compounds (77). The K_i values covered a range of

two orders of magnitude ($0.3 - 43$ μM) (Table 1). Interestingly, while **2-4** have similar

structures and K_i values, the structurally similar **6** has a 40-fold increase in K_i relative to **4**,

making **6** even weaker than **5**, which has no methyl substituent. Overall, the methyl

substituent contributes positively to the binding affinity of the antifolates, resulting in the

>10-fold increased K_i value of **5** relative to **2**. The further increased K_i of **6** relative to **2-5** is

discussed in section 4.2.5. From this analysis of binding affinities, it is clear that DHFR is

very sensitive to minor changes in bound ligand structure.

Next, the binding kinetics for the series were determined. The off-rate (k_{off}) for each

inhibitor was determined using competitive stopped-flow fluorescence measurements. The

series was found to span two orders of magnitude in k_{off} ($0.2 - 20$ s^{-1}), similar to the trend in

K_i (Table 1). In fact, the relationship between K_i and k_{off} for these five antifolates is linear (Fig. 4.2b). The calculated kinetic on-rates for the THQ series are similar, being approximately $3 \times 10^5 - 3 \times 10^6$ $M^{-1}s^{-1}$. In the context of the entire antifolate series (MTX, TMP, and **1-6**), K_i scales by 10^6, k_{off} scales by 10^5, and k_{on} scales by 10^2. Thus it follows that if binding affinity is equivalent to the ratio of k_{off}/k_{on}, and k_{on} is the essentially the same for the ligand series, binding affinity is determined largely by the rate of dissociation. Within the THQ series alone, the effect of k_{off} on K_i is larger than k_{on}, but not as dominant as when considering all eight antifolates.

4.3.2. Structural differences induced by the series are minimal

In characterizing the protein dynamics of a series of receptor-small molecule complexes, any structural differences must be considered, as large changes can underlie differences in observed dynamics. Large structural changes in DHFR were not expected, given the chemical similarity of the antifolates. High-resolution crystal structures were determined for E:NADPH:**3**, E:NADPH:**4**, and E:NADPH:**5** in the $P2_12_12_1$ space group (Fig. 4.3a and Appendices 4.2-4.4). As expected, the overall structures are highly similar (largest backbone rmsd = 0.28 Å). The THQs bind in the folate binding pocket of DHFR, which forms a small crevice in the structure but is not closed off by the protein. The 2,4-diamine moieties of **3-5** overlay closely to that of MTX (42, 44), although the orientation is slightly tilted such that the saturated ring of the THQs shift ~1 Å towards the side chain of Phe31. Subtle differences are observable at N23 in the Met20 loop, in helix C above the antifolate binding site, and in the loop that follows helix C. The difference in orientation of helix C is particularly noteworthy. Shifting of this helix was identified previously in the presence of a

highly flexible quinazoline inhibitor (**1**, Fig. 4.2c), and the shift was thought to occur in order

to accommodate the bulky side chain of the inhibitor (40).
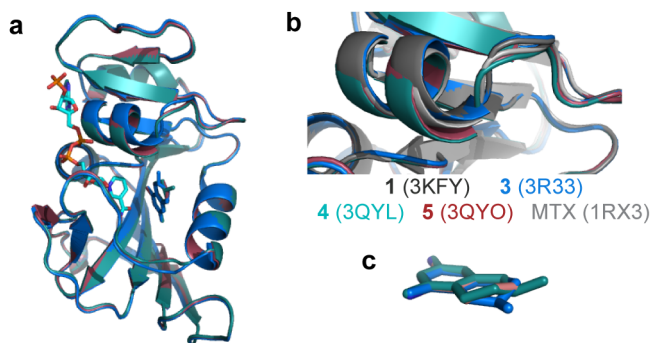
Figure 4.3. High resolution crystal structures for the THQ series. (a) Overlay of the crystal structures for E:NADPH:**3** (blue), ENADPH:**4** (teal), and E:NADPH:**5** (maroon). NADPH is shown in cyan and bound antifolate in the colors designated per complex. (b) Expansion of the C-helix, now overlaying five inhibitor-bound complexes (E:NADPH:**1** in dark grey and E:NADPH:MTX in light grey). PDB IDs are listed parenthetically. (c) Differential puckering of the saturated ring in the bound inhibitors, colored as in (a).

In the present structures, helix C is shifted away from the antifolate binding site in the

presence of **3**, which is not surprising, as the methyl substituent on the THQ ring points in

that direction. This helix appears to be very plastic in order to broaden the substrate binding

site to accommodate the binding of various ligands, as noted previously (42). When

overlaying the current three structures (PDB IDs 3R33, 3QYL, and 3QYO) with previously

determined inhibitor complexes E:NADPH:**1** and E:NADPH:MTX (PDB IDs 3KFY and

1RX3), we find that the shifted positioning of helix C in E:NADPH:**3** and E:NADPH:**1** is the

same while E:NADPH:**4**, E:NADPH:**5** and E:NADPH:MTX represent the unshifted

positioning (Fig. 4.3b). This effect appears to be a consequence of bound ligand structure, as

there is no correlation between the magnitude of C-helix shifting with K_i of the bound

antifolate.

Unlike the structure of E:NADPH:**1** determined previously (40), the ternary

complexes with **3**, **4**, and **5** show strong electron density within the Met20 loop. The loop is

modeled in the closed conformation, similar to that observed in the presence of MTX. The

closed Met20 loop conformation is also observed in solution for all five ternary complexes

via analysis of NMR chemical shift perturbations (CSPs) (section 4.2.4 and Fig. 4.4). In all

three crystal structures, strong electron density is observed for NADPH and bound antifolates

(Fig. 4.3c and Fig. 4.5a-b).
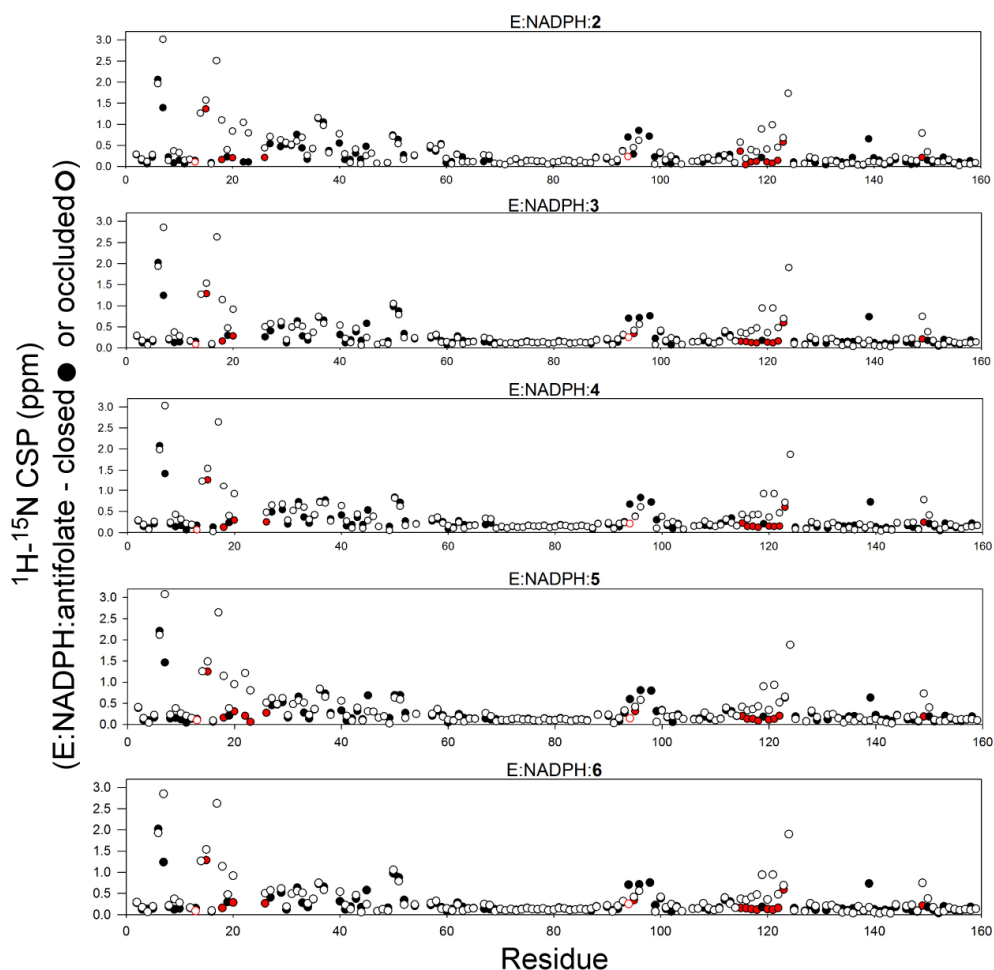
Figure 4.4. Closed Met20 loop analysis for the THQ series of complexes. CSPs of each
E:NADPH:antifolate complex relative to model closed (E:NADP$^+$:folate) and occluded
(E:DHNADPH:folate) complexes. Residues considered chemical shift markers of the conformation of
the Met20 loop are highlighted in red. Closed red circles indicate that the E:NADPH:antifolate
complex is more similar to a closed Met20 loop in solution, while open red circles indicated that the
ternary complex is more similar to an occluded Met20 loop conformation.
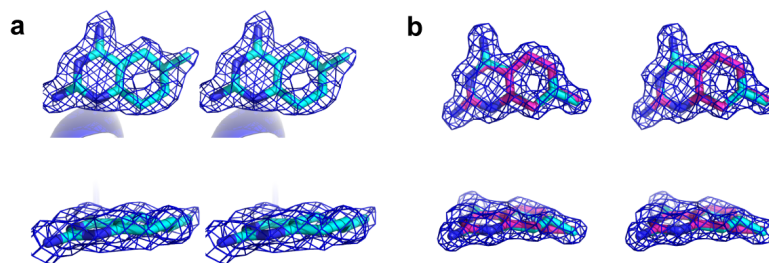
Figure 4.5. Ligand electron density maps for E:NADPH:**3**-**4**. (a) Divergent stereoview of the electron density map (2fo-2fc) for the binding of **3** in E:NADPH:**3**. (b) Similar to (a), the electron density map (2fo-2fc) for the binding of **4** in E:NADPH:**4**.
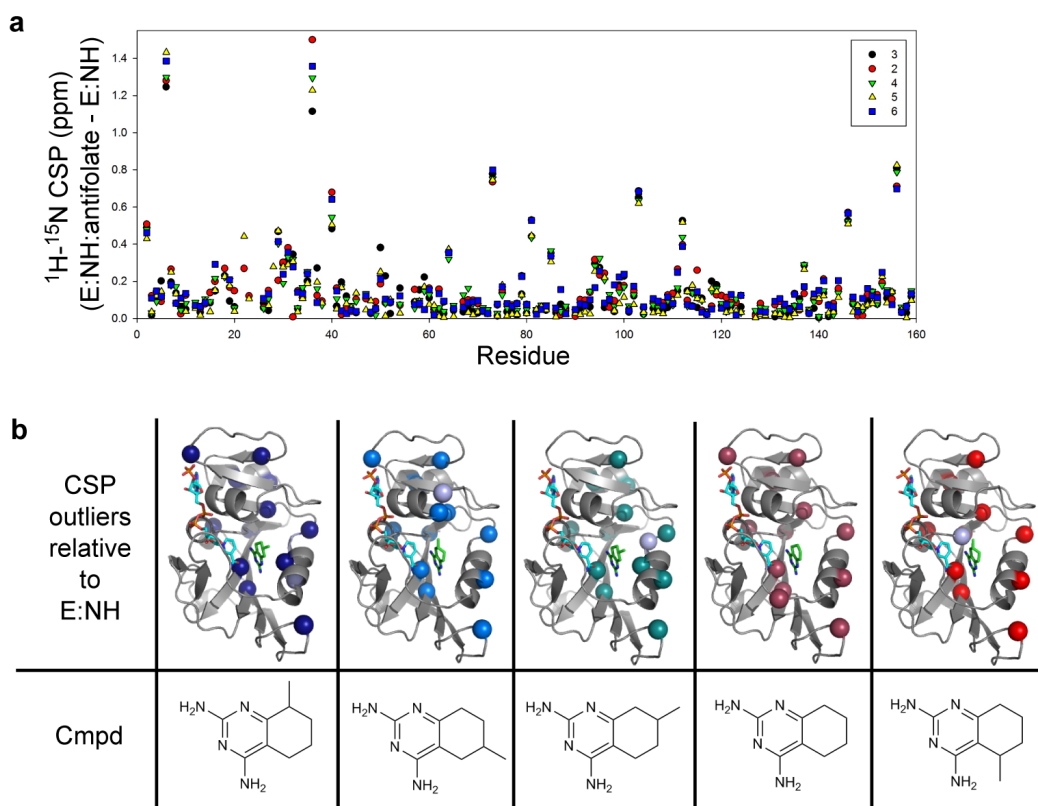
Figure 4.6. CSPs upon antifolate binding. (a) CSPs for each E:NADPH:antifolate complex relative to the absence of inhibitor (E:NADPH). (b) A box plot function was used to identify outlying CSPs in (a), and these outliers have been highlighted with colored spheres for each complex. Light blue spheres indicate sites with significant CSPs that lie below the outlier threshold, yet are sensitive to small molecule inhibitor binding.

Ligand orientations are confirmed to be identical in solution by CSPs (Fig. 4.6a-b). Regarding the C6 methyl substituent of **3**, it should be noted that electron density is observed for only one enantiomer (*R*) (Fig. 4.5a), suggesting that DHFR preferentially binds one enantiomer of the racemic mixture. The binding of *R* is preferred over *S* because the *S* configuration could result in steric clash in the active site between the nicotinamide of NADPH and the methyl substituent of **3**. On the contrary, electron density in the E:NADPH:**4** structure suggests that both *R* and *S* enantiomers of **4** bind (Fig. 4.5b).

In summary, no significant differences in structure are observed among these five ternary inhibited complexes. A straightforward comparison of differential dynamics of complexes in this series is therefore possible.

4.3.3. Slow timescale dynamics structure-activity relationships

In recent years, proteins have been revealed as highly dynamic, especially in the case of enzymes (24, 42, 144-146). In some cases dynamics has been linked with function (6, 22, 138, 147-150). While these motions occur over a broad timescale range, micro-millisecond (μs-ms) or "slow" timescale motions have been shown to correlate directly with biological function (6, 7, 126, 151). The dynamics of DHFR on this timescale have been shown to occur as a sequence of loop motions important to catalytic function when bound to endogenous ligands (6). In addition, interesting differences in slow motions are observed in "off-cycle" binary complexes compared to the "on-cycle" binary product complex, confirming the enzyme's innate sensitivity to different ligands (50). When in complex with inhibitors, DHFR still retains flexibility on the slow timescale, showing motional quenching when bound to MTX or TMP (79) and motional activation when bound to compound **1** (40).

Here, we report slow timescale dynamics of the five reduced-affinity DHFR:THQ complexes. Together with the slow dynamics of three high-affinity inhibitor complexes (40, 79), this set of data comprises a "dynamics structure-activity relationship" (DSAR) series. In other words, this approach probes whether the dynamics of DHFR are sensitive to structural differences in small molecule ligands. This set affords an opportunity to observe trends between dynamics and ligand binding activities. Because the compounds of the series are highly similar in structure, some biophysical activities of the enzyme may be conserved and hence more easily recognized. This DSAR approach is distinct from, yet complementary to, flexibility-activity relationships (FAR), which focuses on dynamics of the bound ligand as shown previously for peptide ligands of Pin1 (152).

For each of the five ternary complexes, μs-ms motion was detected by ^{15}N Carr-Purcell-Meiboom-Gill (CPMG)-relaxation dispersion experiments (28). These experiments allow for the determination of R_{ex}, a component of transverse relaxation due to conformational exchange processes that increases the intrinsic rate of R_2. Assuming a two-state exchange process, these experiments provide kinetic, thermodynamic, and structural information about the transition: R_{ex} depends on the exchange rate constant (k_{ex}), the populations of ground state A and excited state B (p_A and p_B), and the difference in chemical shift between states A and B ($\Delta\omega$) (27).

In contrast to the high similarity of μs-ms dynamics that result upon MTX or TMP binding (79), the THQ inhibitors elicit a more heterogeneous distribution of sites showing R_{ex} (Fig. 4.7). There are, however, among the eight complexes, twelve consensus residues with slow motions regardless of the inhibitor bound (Fig. 4.11a). Thus, the pattern of slow motion elicited by MTX and TMP is not restricted to high-affinity antifolates. In addition to the

consensus 'antifolate sites', new motions are detected near the hinge region (residues 38 and 88) and in α-helices C and F as K_i increases. Although within the THQ series there appears to be no significant correlation between K_i and number of sites with R_{ex}, as a whole this series has a greater amount of R_{ex} compared with MTX and TMP, which bind with much higher affinity. None of these motions in the series are suspected to be the result of association-dissociation cycles effects, as k_{off} values are slow (Table 1) and complexes are saturated to ≥ 99.5%.
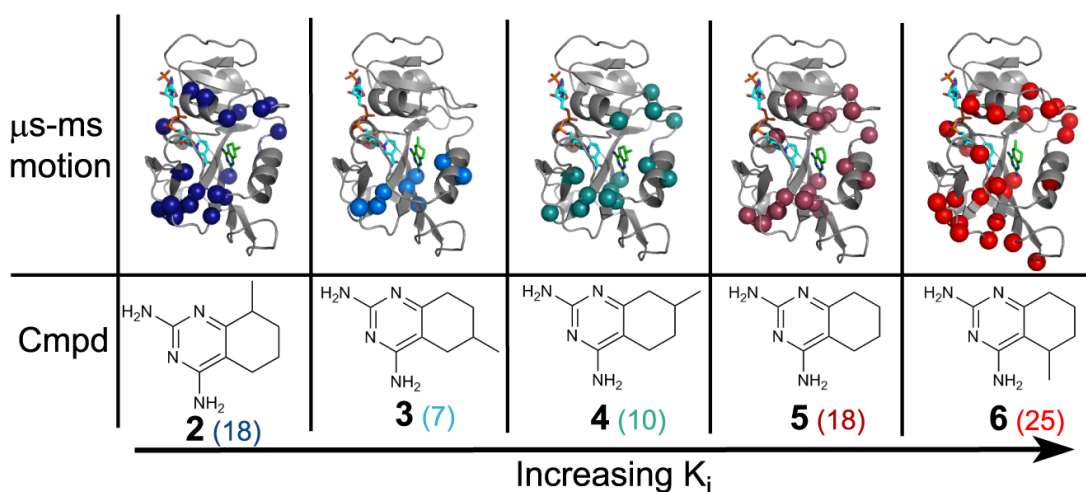
Figure 4.7. Slow timescale dynamics for the reduced-affinity inhibitor series. Sites along the backbone with detectable µs-ms motion are highlighted in colored spheres for each complex, ordered from left to right by increasing K_i value. The number of residues with significant R_{ex} is given parenthetically.

The E:NADPH:**6** complex has additional motions at Met20 loop switching markers, suggestive of a functional switch from closed to occluded (97). However, only five sites show a correlation between Δω fitted from relaxation dispersion and Δδ for closed-to-occluded motion of the loop (Fig. 4.8; residues 12, 115, 118, 120, and 149).
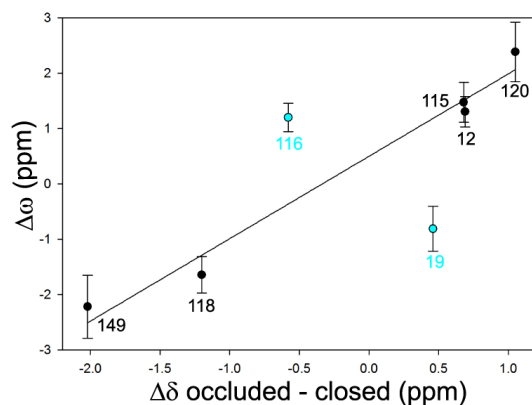
Figure 4.8. Plot of $\Delta\omega$ vs. $\Delta\delta$ (occluded – closed) for Met20 loop marker residues in E:NADPH:**6**. A linear correlation is seen for the points in black ($R = 0.99$). Points in cyan do not lie along this line, but would be expected to if the correlation were very strong.

While the loop appears to be mobile, its motion is not as clear and coherent as observed previously in the presence of **1** (13 sites in the correlation) (40). We believe this Met20 loop motion to be the result of steric clash between nicotinamide of NADPH and the C5 methyl group of **6** within the active site (section 4.2.5). Residues within the F-G and G-H loops are the best markers of Met20 loop switching (e.g., 115, 116, 118, 119, 120, 121, 122, 149, and 150), not those within the Met20 loop itself. It should be noted that, for the large part, the Met20 loop marker residues within the F-G and G-H loops are not observed to undergo μs-ms motion in the presence of compounds **2**-**5** of the series (Appendices 4.5-4.9 and 4.11). Even the best examples of closed complexes (with bound MTX or TMP) exhibit exchange broadening at some of the marker residues. In further support of E:NADPH:**6** being different from the other complexes regarding its Met20 loop mobility, G121 is severely broadened in the presence of **6** but not for the remaining compounds of the series.

4.3.4. Rate of conformational switching is correlated with K_i and k_{off}

For the ternary complexes of **3**, **5** and **6**, global fits of k_{ex} for all residues with R_{ex} range from 1000-1500 s^{-1}, and p_B is fixed at approximately 2% (Table 2).

Cmpd	k_{ex} (s^{-1})	p_A (%)	$k_{conf,forward}$ (s^{-1})
2[a]	1658.5 ± 167.7	95.9 ± 1.0	68.0 ± 7.6
3	1041.4 ± 292.3	98 ± 0.5	20.8 ± 6.0
4[b]	1841.2 ± 189.3	96.3 ± 2.2	68.1 ± 8.6
5	1448.2 ± 422.8	97.9 ± 1.0	30.4 ± 9.2
6	1514.9 ± 206.1	97.7 ± 1.1	34.8 ± 5.1

[a]Sites were split into two groups. The best fit for the slower group is given, despite the observation that many sites possess high χ^2 ratios.
[b]Sites were split into two groups. The best fit for the slower group is given. All residues 'fit' well into this group based on χ^2 ratios.

Table 2. Relaxation dispersion global fitted parameters for the series of THQ complexes.

It follows that the forward rate of conformational exchange ($k_{conf,forward}$) ranges from 20-35 s^{-1} for this series. Initial plots of $k_{conf,forward}$ versus K_i suggested a correlation for these three protein-inhibitor complexes. To further test this correlation, $k_{conf,forward}$ and K_i for MTX, TMP, and **1** were added to the plot (40, 59, 79). For these six complexes, covering six orders of magnitude in binding affinity, we find that $k_{conf,forward}$ scales exponentially with K_i (Fig. 4.9a). As binding affinity decreases (larger K_i), $k_{conf,forward}$ increases (Table 2). Unfortunately, global fitting for complexes **2** and **4** did not converge and thus are not further supportive of this trend, although an alternative fit for **4** was obtained (see section 4.2.5). Based on the exponential relationship between $k_{conf,forward}$ and K_i and the linear correlation between K_i and k_{off} (Fig. 4.2b), $k_{conf,forward}$ vs. k_{off} was plotted and found to scale exponentially (Fig. 4.9b) (52).
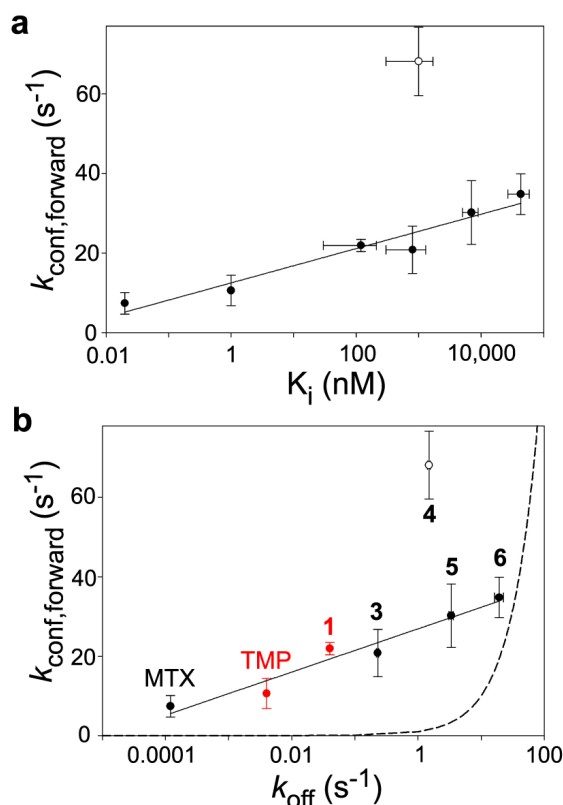
Figure 4.9. Internal motions vary with K_i and k_{off}. (a) The forward rate of motion ($k_{conf,forward}$) fit from relaxation dispersion data for each complex varies exponentially with the K_i value for the bound inhibitor ($R = 0.97$). The open circle represents the best fit for E:NADPH:**4**. (b) An exponential correlation is also seen between $k_{conf,forward}$ and k_{off} ($R = 0.97$). Data points in red have predicted k_{off} values, as described in the text. k_{off} for TMP and **1** were calculated based on estimated values for k_{on}. For **1**, the average k_{on} for the THQ series was used. For TMP, because of its greater similarity to MTX, k_{on} was taken to be intermediate between MTX and the average value for the THQ series. The data point for E:NADPH:**4** (unfilled circle) does not fall along this exponential correlation, suggesting that this correlation may not always be predictive. The dashed curve represents what would be expected if the correlation were linear.

We note that $k_{conf,forward}$ is always greater than k_{off} by at least a factor of two for each complex, providing further evidence against k_{ex} resulting from association-dissociation cycles. This scaling of $k_{conf,forward}$ and k_{off}, with $k_{conf,forward} > k_{off}$, is highly suggestive of a mechanistic role for the ground-to-excited state conformational change in ligand release. In Figure 4.9b, because k_{off} for TMP and **1** are too slow for detection via the assay employed, they were calculated from K_i and their approximate k_{on} value for the series. The k_{off} value for MTX was taken from the literature (52). The best fitted $k_{conf,forward}$ for **4** has been included in

Figure 4.9b, even though global fitting was more challenging in this case; its position off the main correlation line suggests that additional factors may contribute to release for a particular ligand, even if it is part of a structurally constrained series. Nevertheless, the fact that the remaining ligands fall on the line suggests that the millisecond structural fluctuations potentiate dissociation over the entire ligand series, including MTX and TMP.

A correlation between $k_{conf,forward}$ and k_{off} is shown above. A similar exponential relationship also exists between $k_{conf,reverse}$ and k_{off} ($R = 0.97$) (Fig. 4.10a). To a lesser degree is the agreement between k_{ex} and k_{off} ($R = 0.89$) (Fig. 4.10b).
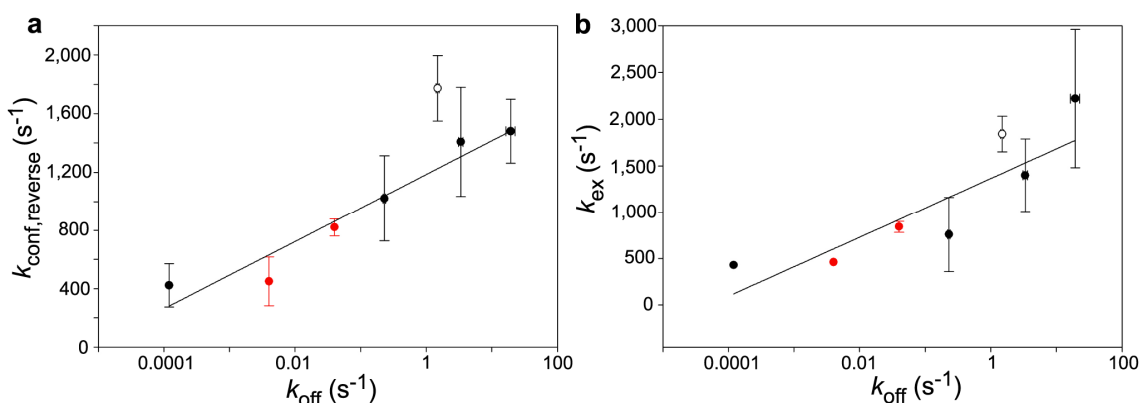
Figure 4.10. The correlation of k_{off} to (a) $k_{conf,reverse}$ and (b) k_{ex}. Red circles for TMP and **1** indicate k_{off} values calculated based on k_{on} for the series. The open circle indicates the best fit for E:NADPH:**4** despite a difference in the method of global fitting.

4.3.5. Antifolate complexes sample a structurally identical excited state

Relaxation dispersion experiments can also provide structural information about the excited state. As mentioned previously, from data on the eight drug/inhibitor complexes, there are twelve consensus residues undergoing µs-ms motion irrespective of the inhibitor bound to the holoenzyme (Fig. 4.11a).
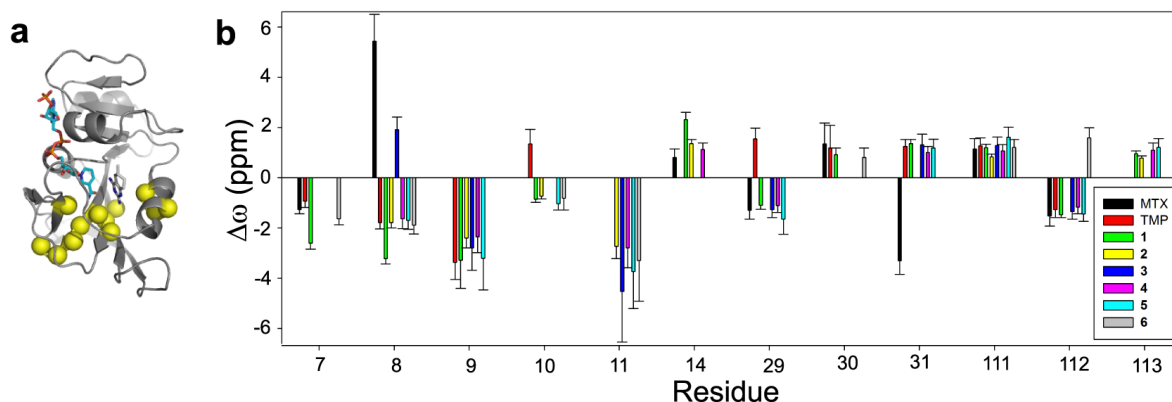
Figure 4.11. Antifolate consensus sites sample a structurally similar excited state. (a) The twelve antifolate consensus sites are highlighted in yellow colored spheres. (b) Dynamic $\Delta\omega$ values fitted from relaxation dispersion for these twelve sites cluster for each residue. The eight complexes are colored by the bound inhibitor, as indicated in the legend. No bar is shown if that residue did not exhibit significant slow motion while bound to a particular inhibitor. Error bars result from Monte Carlo simulations.

These sites were initially identified from the least dynamic complexes, those with MTX or TMP bound (40, 79). Here, we define a residue as a consensus site if slow motion is detected at that position (when assignable) in (a) $\geq 2/3$ of the eight complexes (residues 8-11, 14, 29, 31, 111-113), or (b) $\geq \frac{1}{2}$ of the complexes when ΔR_{ex} is significant in the other half but lies just below our stringent requirement of 2 s^{-1} (residues 7 and 30). The dynamic change in chemical shift ($\Delta\omega$) at these consensus sites fitted from relaxation dispersions for each complex were analyzed. For each individual residue, the fitted $\Delta\omega$ parameter clusters around the same value, despite changes in chemical structure and binding affinity for the different inhibitors (Fig. 4.11b). This clustering of $\Delta\omega$ values indicates that the same excited state is being sampled by the consensus residues in each of the eight antifolate complexes. This pattern of $\Delta\omega$ values does not correlate with $\Delta\omega$ fitted from previous studies of DHFR bound to physiological, folate-derived ligands (Fig. 4.12) (6) and hence is unique to the antifolates studied here.
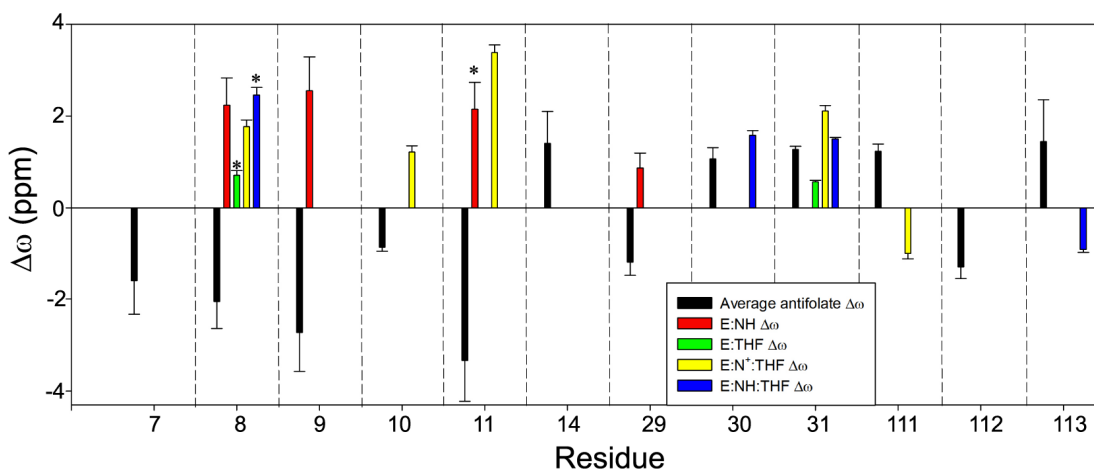
Figure 4.12. Comparison of average fitted E:NADPH:antifolate $\Delta\omega$ value to those fitted in physiological complexes. For the twelve consensus antifolate sites, an average fitted $\Delta\omega$ value was calculated along with the standard deviation in that fitted value. Complexes that do not follow the pattern of sign for $\Delta\omega$ were excluded. This average and standard deviation are plotted per residue against $\Delta\omega$ values fitted for physiological complexes studied previously. An asterisk indicates that the sign of $\Delta\omega$ was not determined. Note that the pattern of sign and values of $\Delta\omega$ are distinct in the presence of the antifolates relative to endogenous, folate-derived ligands.

In addition, because poor correlations between $\Delta\omega$ fitted from the dispersion data and $\Delta\delta$ from chemical shift changes (E:NADPH – E:NADPH:antifolate) were observed for the consensus sites (Fig. 4.13), the antifolates appear to be bound in the excited state. We propose that these residues sampling a novel excited state mediate dissociation of antifolate ligand. This state is sampled at somewhat different rates, but the concerted motion of the consensus residues is conserved across these antifolate complexes.

We note that while these complexes share this common dynamic sampling, differences in slow motions remain among the different complexes (40, 79) (Fig. 4.7, Appendices 4.5-4.9). Thus, this "shared" motion appears to be able to exist in the context of additional motions (or lack thereof) in other regions of the enzyme.

94
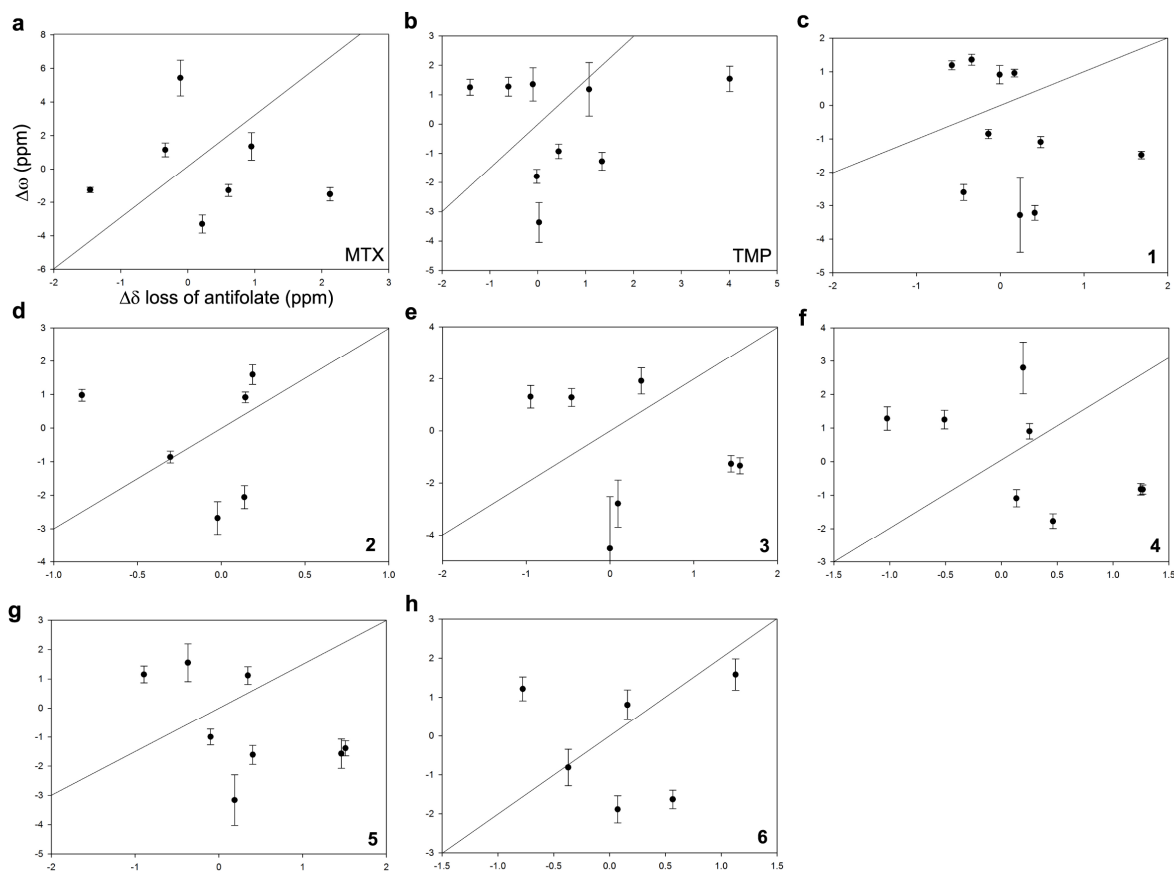
Figure 4.13. Dynamic chemical shift analyses. (a-h) Attempts to correlate the loss of drug in the excited state of the antifolate consensus residues in the presence of each studied inhibitor are shown, where $\Delta\omega$ is the dynamic ^{15}N chemical shift change fitted from relaxation dispersion and $\Delta\delta$ is the steady-state difference (E:NADPH - E:NADPH:antifolate): (a) E:NADPH:MTX, (b) E:NADPH:TMP, (c) E:NADPH:**1**, (d) E:NADPH:**2**, (e) E:NADPH:**3**, (f) E:NADPH:**4**, (g) E:NADPH:**5**, and (h) E:NADPH:**6**. A line with a slope of 1 is drawn on each plot, demonstrating the lack of correlation. At most, two residues out of the twelve could suggest loss of drug in the excited state.

4.3.6. Mechanism of ligand dissociation: gating or ejection?

The scaling of the rate constant for forward conformational change with k_{off} implicates a millisecond timescale motion in the mechanism for ligand dissociation. At what point during the conformational sampling does release actually occur? We can envision two different mechanisms for release. The first is a "gating" model. Upon transitioning to the excited state, ligand remains initially bound but is subject to release while the gate is open.

In this model, release might be dependent on sub-millisecond motions that essentially kick out the ligand or break non-covalent interactions through shearing motions. Release from the open gate could also occur in a stochastic manner based on the overall strength of interactions. For the specific 2,4-diaminopyrimidine series studied here, adding substituents beyond the second ring (e.g., methyls in THQ series, methoxy groups in TMP, etc.) could have a dual effect: (i) these groups could serve to slow switching, as observed, due to stabilization of both ground and excited states, and (ii) by providing additional contacts to protein, these substituents would reduce the probability of stochastic release from the excited state, as observed (Fig. 4.11b, Table 2). The second model is an "ejection" model. Here, the actual act of switching would "throw" the ligand off the binding site. In principle, ligand could also be released on the return conformational change back to the ground state. For simple ejection behavior, matching of the conformational exchange rate with k_{off} is expected. In the inhibitor series studied here, the fact that the efficiency of ejection decreases rapidly as the switching slows is discussed below.

4.4. Discussion

Here we show that, for a series of homologous antifolates binding to DHFR, binding affinity (K_i) is determined largely by k_{off}. We also demonstrate that the rate of internal motions in the enzyme ($k_{conf,forward}$) is related to both binding affinity and k_{off} for the series of substrate competitive ligands. The data suggest that DHFR samples an identical excited state in solution regardless of which particular antifolate is bound, and that this state is novel because it differs in structure from absence of ligand and from the excited states sampled by physiological complexes (Fig. 4.12). It is also worth noting that the THQ complexes

undergo switching ~3 times faster than the physiological complexes. Because ligand is still

bound in the excited state and the rate of internal motion is correlated with k_{off}, we propose

that this excited state is en route to dissociation of inhibitor and is the primary determinant of

k_{off}.

In previous work, connections between internal motions and protein activity have

been drawn when an internal switching rate precisely matches a macroscopic rate constant (6,

7). We show here, through the use of a homologous ligand series, that such matching need

not be required to mechanistically connect two functional events. The "function" of ligand

dissociation is fundamental in macromolecular interactions, and insights into what stimulates

dissociation have potentially broad implications for manipulating biological systems. The

main insight revealed here is that dissociation can be driven by defined, protein internal

motion, presumably at the interface, rather than by a fully stochastic process scaled by the

overall strength of interaction. This inference of motions driving dissociation might seem

expected for a buried binding site in which a 'lid' must open for release; however, in this

particular case, the ligand binding site is exposed, and yet dissociation appears to not be

stochastic.

What is somewhat surprising from the correlation of $k_{conf,forward}$ to K_i or k_{off} is that the

relationship is log-linear. In addition, DHFR is not productive at releasing inhibitors each

time it reaches the excited state, as $k_{conf,forward}$ is always faster than k_{off}. Thus, the enzyme

appears to be more efficient at release as the rate of internal motion increases. For the gating

model (discussed above), this may be explained by a loss of substituents. For the ejection

model, we propose an alternate explanation. As inhibitors (in the series) bind with greater

affinity (and longer residence times), the ~1 ms spent in the excited state is less efficient at

ejecting ligand, as if the slightly slowed switching introduces a molecular "stickiness" to the interaction. To be effective, the motions must approach a critical frequency to weaken the intermolecular forces sufficiently to allow for ligand release. Because the probability of release from the excited state is highly dependent on the time spent in the ground state (in a non-linear manner), there is a memory effect. Hence, this is a high-resolution example of hysteresis, a well-known property of enzymes (59, 153).

It is important to stress that any ligand bearing resemblance to the series or (or that binds to the same active site) should not necessarily obey the correlation in Figure 4.9b. Indeed, **2** and **4** do not (see section 4.2.5). It is reasonable to expect that numerous mechanisms for ligand release could compete with one another, and some ligands may trigger specific mechanisms over others due to their chemical structure. We have been fortunate here in using a panel of ligands that share a common mechanism that is distinct from release of folate-derived ligands. It will be interesting to see whether other ligand series against different proteins show similarity in behavior as was observed here.

As mentioned previously, gaining an understanding of the molecular basis of k_{off} has implications for structure-based drug design. If protein dynamics are found to correlate with k_{off} in other systems, this type of analysis may be useful in optimizing ligand residence times to meet the desired pharmaceutical modulation of disease states. The DSAR methodology provides more than just a correlation between the rate of internal motions and k_{off} – it also potentially provides structural information on residues sampling multiple conformations and even what the structure of the excited state(s) may be (154, 155). This combined information would be useful in directing medicinal chemistry efforts toward modulating the stability of excited states that promote efficient ejection of inhibitors.

Chapter 5

Reduced-Affinity Antifolate Binding Alters ps-ns Dynamics within the Closed Conformation

5.1. Introduction

Proteins are structurally dynamic, existing in an ensemble of conformations in solution that are important for biological functions such as folding, ligand binding, and catalysis. As mentioned previously, μs-ms protein dynamics have been directly linked to function. While a relationship between ps-ns dynamics and protein function has been reported in only a few cases (25, 149, 150), it is thought that fast timescale motions may "lubricate" those motions on the slow timescale which are relevant to biology (15). A systematic study of dynamics on both the slow and fast timescales for a model system known to possess slow motions important to function is necessary to implicate fast motions in slow, functional motions. DHFR serves as an excellent system to probe for a relationship between slow and fast motions, as studies of complexes bound to endogenous ligands link its slow timescale motions to progression through the catalytic cycle (6, 51).

In addition to extensive characterization of μs-ms motions, the flexibility of DHFR on the ps-ns timescale has also been characterized previously within the context of the catalytic cycle. An analysis of two complexes possessing the occluded Met20 loop conformation

showed significant backbone flexibility within the hinge region (residues 38 and 88), the adenosine binding loop (residues 67-69), and several sites in the Met20 and F-G loops (46, 47). Closure of the Met20 loop in the Michaelis model complex (E:NADP$^+$:folate) results in quenching of ps-ns backbone flexibility within the Met20 and F-G loops, but an increase in flexibility is observed in the adenosine binding loop (47). These observations of backbone dynamics are mirrored on the side chains, in which dynamics appear to be quenched upon the Met20 loop transitioning from occluded to closed (48). From these studies, it was postulated that DHFR's ps-ns timescale flexibility is dictated by the global conformation of the Met20 loop (50, 108).

We are interested in studying whether dynamics change significantly within the same structural state (closed Met20 loop) upon binding a series of antifolates. Given the correlation of DHFR slow motions with binding affinity and the kinetic rate of dissociation for antifolates shown in Chapter 4, we were also interested in looking for patterns of ps-ns motions that vary with K_i, with the possibility of drawing a connection between dynamics on the two timescales. To expand upon the timescale range of dynamic modulation by reduced-affinity antifolates, ^{15}N and ^{2}H spin relaxation experiments have been conducted. Here we report an analysis of ps-ns timescale flexibility in DHFR while bound to NADPH and three reduced-affinity inhibitors from the series (**1**, **3**, and **5** in Figure 1.8). Together with data collected previously in the Lee Lab (section 2.3.3) (79, 156), the fast timescale dynamics of DHFR have been characterized for seven complexes, including the absence of inhibitor, five E:NADPH:antifolate complexes covering a K_i range of 10^6, and one mutant E:NADPH:antifolate complex. The site specific changes in dynamics relative to the absence of inhibitor demonstrate that reduced-affinity inhibitors modulate dynamics differently than

100

observed for MTX and TMP binding. While dynamics in the adenosine binding loop are perturbed in these reduced-affinity complexes, the magnitude of perturbation is less dramatic. Flexibility of the backbone and side chains appear to balance one another to maintain a constant level of flexibility across the binding affinity range of the series. Two ternary complexes stand out as ps-ns dynamic anomalies, consistent with μs-ms motions. The dataset suggests three dynamic groupings of complexes: (1) high-affinity antifolates, (2) reduced-affinity antifolates and mutant, and (3) highly skewed groups.

5.2. Materials and Methods

5.2.1. Protein Expression and Purification

Isotopically labeled DHFR was expressed and purified as described in 2.2.1. Samples used for ^{2}H relaxation experiments were made with uniform ^{15}N and ^{13}C labeling, as well as 60% ^{2}H, for which the percentage of D_2O used in M9 preparation is approximately 60% to maximize the population of CH_2D methyl isotopomers.

5.2.2. NMR Spectroscopy

NMR samples contained 1 mM isotopically labeled *E. coli* DHFR in NMR Buffer, 15 mM NADPH, 2.5-10 mM antifolate (2.5 mM antifolate for E:NADPH:**1** and E:NADPH:**3**, 10 mM antifolate for E:NADPH:**5**), 10 mM glucose-6-phosphate, 10 units glucose-6-phosphate dehydrogenase, and 10% D_2O for spectrometer locking purposes. The concentrations of DHFR and NADPH were determined spectrophotometrically (36). Stock solutions of the antifolates in 90% H_2O/10% D_2O were prepared and concentrations were determined by PULCON relative to tyrosine, valine, or trimethoprim standards (110). All samples were

protected from light and air exposure by containment in argon-purged, flame-sealed, amber coated NMR tubes.

NMR experiments were conducted at 298 K on Varian spectrometers equipped with room temperature (500, 600, and 700 MHz) or cryogenic probes (700 MHz). Backbone assignments for E:NADPH:**1**, E:NADPH:**3**, and E:NADPH:**5** have been described previously in 3.2.4. and 4.2.4. Assignments of side-chain methyl resonances were accomplished by use of the HCCH$_3$-TOCSY experiment and the HMBC for methionine resonances at 600 MHz (90, 91). Stereospecific methyl assignments for leucine and valine were determined via the method of Neri *et al*. (92). Data were processed using NMRPipe while analyzed using NMRDraw and NMRView (87, 88).

As described previously in 2.2.2., standard backbone ^{15}N R_1, R_2, and NOE experiments were conducted at 500 and 600 MHz to probe backbone flexibility in the studied complexes. T_1 sampling delay times were as follows: 49[*], 139, 254, 389[*], 544, 709, 894, 1004[*], and 1304 ms. T_2 sampling delay times were as follows: 7.8[*], 15.7, 23.5, 39.2[*], 62.7, 78.3, 94.0, 109.6[*], and 125.3 ms. Side-chain flexibility was examined by conducting ^{2}H D_z and D_y experiments at 600 and 700 MHz (for improved peak separation). D_z sampling delay times were as follows: 4.15[*], 10.9, 19.6, 30.0[*], 41.8, 54.8, 68.9, 84.1[*], and 100.4 ms. D_y sampling delay times were as follows: 0.7[*], 2.1, 3.8, 5.9[*], 8.3, 10.9, 13.7, 16.8[*], and 20.0 ms. Three duplicate planes were collected for both ^{15}N and ^{2}H relaxation, as indicated by asterisks, for the purpose of error estimation. With the exception of ^{15}N relaxation analysis of E:NADPH:**5** (500 MHz only), two fields of data were acquired for both backbone and side-chain relaxation experiments for all three complexes. As a result, E:NADPH:**5**

backbone relaxation data were fitted only to models 1-3 of the Lipari Szabo model-free

formalism, to be described below.

5.2.3. Lipari-Szabo Model-Free Analysis

As described in 2.2.4., ps-ns ^{15}N and ^{2}H dynamics were characterized via the Lipari-

Szabo model-free formalism (17). An anisotropic rotational diffusion tensor was fitted for all

three new ternary complexes studied using the local D_i method (94) and the crystal structure

of E:NADPH:MTX (PDB ID 1RX3). Because of the significant effect anisotropy can have

on model selection (93), rotational anisotropy corrections ($D_{par}/D_{perp} \approx 1.15$) were used for all

three complexes. Backbone relaxation data were fit to all five model-free models in the case

of E:NADPH:**1** and E:NADPH:**3**, using Akaike's information criterion to guide model

selection (95). However, because only three datasets were collected for E:NADPH:**5**, fitting

to models 4 and 5 was not justified (more parameters to fit than datasets collected). In the

case of E:NADPH:**5**, the best fit model substitution for models 4 and 5 were models 3 and 2,

respectively. For all complexes, side-chain relaxation data were fitted to model 2 with no

correction for rotational anisotropy.

5.2.4. Calculating Conformational Entropy

The conformational entropy of a protein can be perturbed significantly by changes

such as temperature variations and ligand binding (22, 25, 157, 158). Because NMR

dynamics studies provide a measure of site-specific determination of flexibility or disorder,

order parameters from spin-relaxation experiments can be converted into local entropy

values, or conformational entropies (159, 160). Side chain order parameters can be translated

into conformational entropy values using the method of Li and Bruschweiler (161). This approach depends heavily on the amino acid type, as the number of side-chain dihedral angles is found in the conversion equation:

$$S = k_B M \left[A + Bf \left(1 - S^2{}_{NMR} \right) \right],$$ (5.1)

where M is the number of side-chain dihedral angles, A and B are fitted parameters that depend on amino acid type groupings, and either

$$f(x) = x \ \text{or}$$ (5.2)

$$f(x) = \log(x) \ .$$ (5.3)

In the current study, conformational entropies can be used to determine how ligand binding impacts the thermodynamic stability of DHFR on a site-specific level. These values can possibly be related to inhibitor binding affinities or to the thermodynamics of binding determined by isothermal titration calorimetry (ITC). For example, if ligand binding is entropically driven from ITC measurements, one could dissect the local conformational entropies to determine which sites in particular are responsible for the observed effect.

5.3. Results and Discussion

5.3.1. Analysis of backbone ps-ns dynamics for the series

Backbone dynamics have been fitted similarly for all three ternary inhibited complexes with bound **1**, **3**, and **5**. From the anisotropic rotation diffusion tensor and Lipari-Szabo analyses, very similar rotational tumbling (τ_m) and anisotropic corrections have been found for the three complexes, extending to E:NADPH:TMP discussed in Chapter 2 (Table 5.1).

Complex	τ_m (ns)	D_{par}/D_{perp}
E:NADPH:**1**	10.60	1.132[*]
E:NADPH:**3**	10.77	1.144
E:NADPH:**5**	10.55	1.181
E:NADPH:TMP (reference)	10.69	1.132

[*] Monte-Carlo simulations from the qfit program jump between slightly prolate and oblate anisotropic diffusion corrections. The correction fitted from E:NADPH:TMP was thus used to approximate a prolate diffusion tensor.

Table 5.1. Rotational tumbling times and anisotropic diffusion corrections. Relative to E:NADPH:TMP presented in Chapter 2, the fitted tumbling time and anisotropic diffusion parameters are given for three reduced-affinity complexes.

The raw S^2 values fit for the three complexes have been compared to each other and to several complexes studied previously in the Lee Lab (Table 5.2) (79, 156). To make comparisons amongst the seven total complexes with characterized ps-ns backbone dynamics, correlation plots were made with the "reference complex" on the y-axis and the "comparison complex" on the x-axis. A total of 63 reporters (out of 148 possible) were used for the correlation, where a reporter is a residue with measurable backbone dynamics in all seven complexes. A line of best fit was found for the 63 backbone sites in the pair-wise comparisons shown below, with the R correlation value indicating how similar the compared order parameters are for each pair. From the pair-wise comparisons, it is noted that the analyzed ternary complexes are equivalently dissimilar to the E:NADPH complex ($R \approx 0.75$), indicating significant changes in order parameters upon binding of the small molecule inhibitors. Additionally, the three newly presented complexes in this study (ENADPH:**1**, E:NADPH:**3**, and E:NADPH:**5**) are both quite similar to each other and surprisingly similar to the M42W mutant E:NADPH:MTX complex ($R \approx 0.92$). These three complexes are also well correlated dynamically with E:NADPH:TMP ($R \approx 0.93$); however, E:NADPH:MTX is less like the reduced-affinity antifolate complexes along the backbone. This highlights a

significant difference in raw S^2 between wild-type E:NADPH:MTX and the M42W mutant of

the complex, as noted previously (156).

Reference complex	Comparison complex	R value
E:NADPH:MTX[a]	E:NADPH[a]	0.60
	E:NADPH:TMP[a]	0.76
E:NADPH:TMP	E:NADPH	0.79
E:NADPH:**1**	E:NADPH	0.77
	E:NADPH:MTX	0.78
	E:NADPH:TMP	0.92
	E:NADPH:**3**	0.97
	E:NADPH:**5**	0.89
	M42W E:NADPH:MTX[b]	0.96
E:NADPH:**3**	E:NADPH	0.76
	E:NADPH:MTX	0.81
	E:NADPH:TMP	0.94
	E:NADPH:**5**	0.92
	M42W E:NADPH:MTX	0.96
E:NADPH:**5**	E:NADPH	0.75
	E:NADPH:MTX	0.82
	E:NADPH:TMP	0.91
	M42W E:NADPH:MTX	0.87

[a]Complexes studied and reported previously (79).
[b]Complex studied and reported previously (156).

Table 5.2. Pair-wise comparisons of raw S^2 values for seven DHFR complexes studied in the Lee Lab.

Another interesting observation from the raw S^2 values is the dynamics of residues

67-69 in the adenosine binding loop. We reported previously that MTX and TMP perturb the

flexibility at these residues that are quite distal to the substrate binding site (79). While S^2

values were perturbed, they were not considered significant by our strict criterion. MTX and

TMP cause a mild rigidification of the adenosine binding loop relative to the absence of drug,

as seen by the increase in order parameters (Figure 5.1).
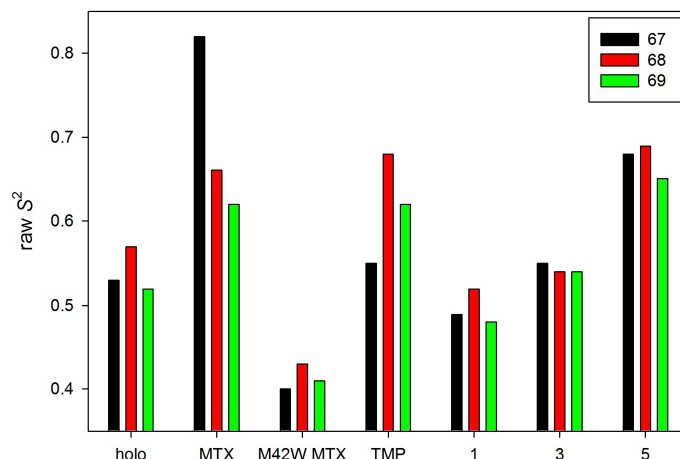
Figure 5.1. S^2 values for residues 67-69 of the adenosine binding loop for all seven complexes, arranged by ligand K_i values.

With the addition of data on the reduced-affinity antifolate complexes and the M42W mutant, new patterns emerge. The M42W E:NADPH:MTX and E:NADPH:**1** complexes both cause an increase in flexibility at residues 67-69 (decreased S^2). S^2 values in E:NADPH:**3** are approximately equivalent to E:NADPH, suggesting that perhaps a certain binding affinity is needed to cause rigidification at these sites and **3** is below that threshold. The apparent increase in S^2 values in E:NADPH:**5** is likely an artifact of model selection, in that model 5 was not used in fitting due to having collected data at only one field strength. Residues 67-69 have been fit to model 5 in all other complexes studied. Fitting to model 5 results in lower order parameters, as the reported S^2 is calculated by multiplying the slow and fast order parameter components (see Equation 1.10).

Given the dissimilarity of these ternary inhibited complexes relative to the absence of drug (i.e., E:NADPH), differences in S^2 were calculated to identify site-specific changes in flexibility upon ligand binding. Perturbations in flexibility are considered significant when the difference in S^2 is greater than two times the error in the fitted parameter. These

107

calculated differences are shown below in Figure 5.2, with significant perturbations indicated

by colored bars. Overall, the changes in backbone dynamics are modest. The sites with

significant differences in backbone flexibility are highlighted on the structure of DHFR in

Figure 5.3, shown relative to the three complexes reported on previously by our group.
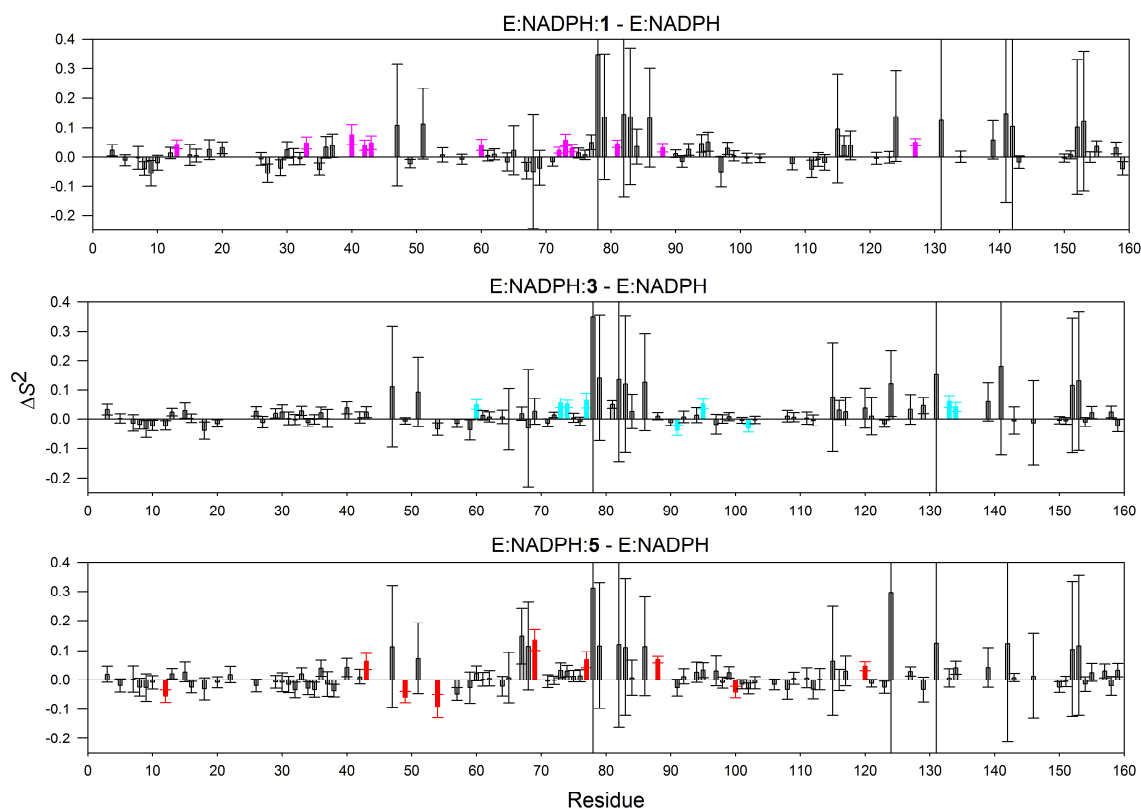
Figure 5.2. Differences in S^2 for the three ternary complexes relative to the absence of inhibitor. Significant changes are noted at sites with colored bars.
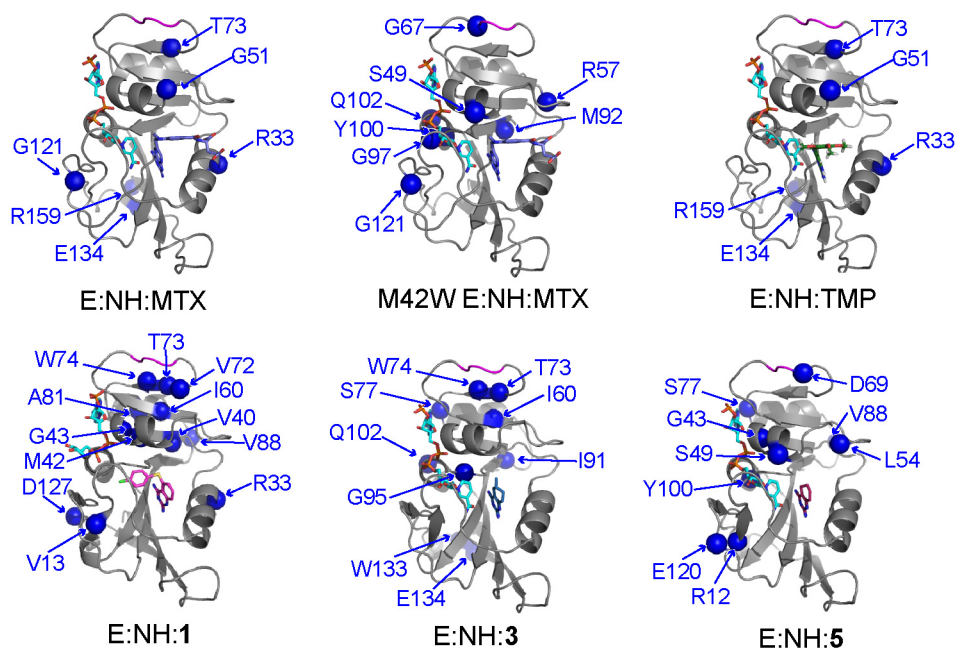
Figure 5.3. Residues with significant changes in S^2 for all DHFR complexes studied. Significant changes are highlighted with blue spheres and perturbed residues 67-69 of the adenosine binding loop are colored magenta.

Several interesting points can be made from the pattern of these differences in backbone flexibility. Firstly, as reported previously, MTX and TMP binding dynamically perturb the same set of residues (79). While there is a conservation of some of these residues in the case of the reduced-affinity antifolate complexes, for the most part, compounds **1**, **3**, and **5** cause changes in flexibility at different sites than the high-affinity inhibitors. If the M42W E:NADPH:MTX and E:NADPH:**1** complexes are excluded (considered anomalous for reasons to be described later), a general pattern is noticed for the remaining complexes: the number of sites with significant differences in flexibility increases with inhibitor K_i values. Of the sites with significant changes in flexibility for these four complexes, MTX and TMP binding causes rigidification at all sites perturbed, whereas a mix of increases (2 and 4 sites, respectively) and decreases (7 and 5 sites, respectively) in flexibility are noted for the binding of **3** and **5**. In other words, reduced-affinity inhibitors elicit a greater number of

small-scale changes in backbone flexibility. The greater number of sites showing changes in backbone S^2 correlates with the greater amount of μs-ms switching described in Chapter 4. This trend on the ps-ns timescale may possibly be due to the enzyme dynamically rejecting these weaker inhibitors. For all backbone sites, it turns out that there is a exponential decrease ($R = 0.95$) in the average ΔS^2 with K_i for the series (Figure 5.4). Although the range of ΔS^2 is small, this suggests that DHFR's ps-ns timescale motions are sensitive to ligand binding affinities, as shown in Chapter 4 for μs-ms motions.
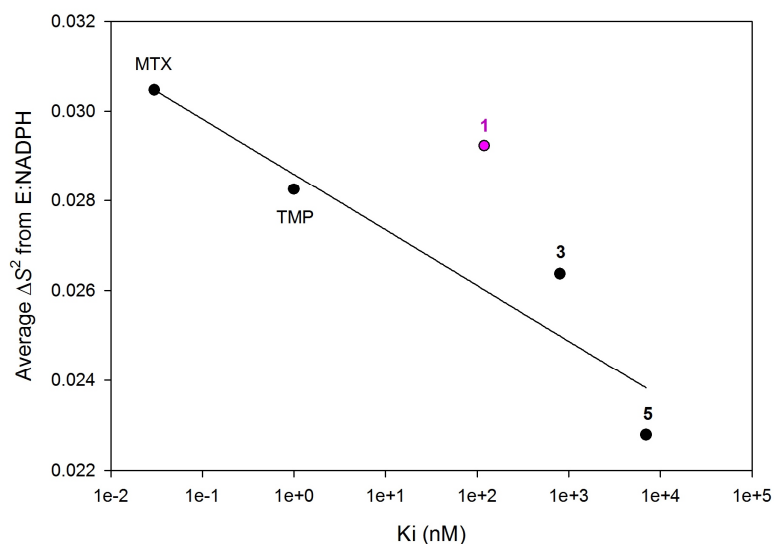
Figure 5.4. The correlation of ΔS^2 for antifolate binding. Outlier E:NADPH:**1** is shown in magenta.

E:NADPH:**1** does not fit this correlation well, to be discussed in section 5.3.5. One final note on the pattern of residues perturbed is that the M42W mutation confers significant changes in flexibility at an entirely different set of residues than the wild-type enzyme bound to MTX. This anomaly will be described in section 5.3.5.

Similar to the pair-wise correlations made between the seven complexes based on raw S^2 values, correlations can be made based on the differences in S^2 from E:NADPH (ΔS^2). The same 63 reporters with measurable order parameters mentioned previously have been

used for these correlation plots. The pair-wise correlation coefficients are given below in

Table 5.3.

Reference complex	Comparison complex	R value
E:NADPH:MTX	E:NADPH:TMP	0.79
E:NADPH:**1**	E:NADPH:MTX	0.59
	E:NADPH:TMP	0.80
	E:NADPH:**3**	0.92
	E:NADPH:**5**	0.70
	M42W E:NADPH:MTX	0.91
E:NADPH:**3**	E:NADPH:MTX	0.72
	E:NADPH:TMP	0.87
	E:NADPH:**5**	0.80
	M42W E:NADPH:MTX	0.88
E:NADPH:**5**	E:NADPH:MTX	0.84
	E:NADPH:TMP	0.74
	M42W E:NADPH:MTX	0.58

Table 5.3. Pair-wise comparisons of ΔS^2 values for seven DHFR complexes studied in the Lee Lab.

The differences in dynamics relative to holoeznyme for two of the reduced-affinity antifolate complexes, E:NADPH:**1** and **3**¸ are highly similar to the M42W E:NADPH:MTX complex. This is interesting, given that E:NADPH:**1** and E:NADPH:**3** are not highly correlated with the wild-type E:NADPH:MTX complex. On the contrary, E:NADPH:**5** is most similar to E:NADPH:MTX. The correlation of backbone dynamics in the reduced-affinity antifolate ternary complexes with the M42W mutant complex is seen for both raw S^2 and ΔS^2 values.

5.3.2. Analysis of side-chain ps-ns dynamics for the series

Similar to the backbone dynamics discussed in the previous section, ps-ns timescale side-chain dynamics have been characterized for seven different DHFR complexes. Three new reduced-affinity antifolate complexes are reported herein – holoenzyme bound to **1**, **3**, and **5** – and are compared to complexes on which we have reported previously (79, 156).

Correlation plots have been made for these data, using only methyl groups with measurable dynamics in all seven complexes (38 reporters out of 92 possible). Correlation coefficients for the pair-wise comparisons of raw S^2_{axis} values are given below in Table 5.4.

Reference complex	Comparison complex	R value
E:NADPH:MTX[a]	E:NADPH[a]	0.96
	E:NADPH:TMP[a]	0.93
E:NADPH:TMP	E:NADPH	0.90
E:NADPH:**1**	E:NADPH	0.88
	E:NADPH:MTX	0.82
	E:NADPH:TMP	0.82
	E:NADPH:**3**	0.85
	E:NADPH:**5**	0.82
	M42W E:NADPH:MTX[b]	0.86
E:NADPH:**3**	E:NADPH	0.90
	E:NADPH:MTX	0.93
	E:NADPH:TMP	0.89
	E:NADPH:**5**	0.92
	M42W E:NADPH:MTX	0.91
E:NADPH:**5**	E:NADPH	0.93
	E:NADPH:MTX	0.97
	E:NADPH:TMP	0.91
	M42W E:NADPH:MTX	0.96

[a]Complexes studied and reported previously (79).
[b]Complex studied and reported previously (156).

Table 5.4. Pair-wise comparisons of raw S^2_{axis} values for seven DHFR complexes studied in the Lee Lab.

All ternary inhibitor complexes agree with the dynamics of the holoenzyme to a similar degree ($R \approx 0.9$). This is interesting, given the greater variability in methyl side-chain order parameters relative to the backbone. The similarity may be due to the greater dynamic range for side-chain order parameters. E:NADPH:**1** is less similar to the other complexes, as its R values are only in the range of 0.82-0.86. Two of the three reduced-affinity antifolate complexes (with **3** and **5** bound) show high correlations with both wild-type and M42W mutant E:NADPH:MTX. Recall that this similarity was also noted for backbone dynamics.

Calculating the difference in S^2_{axis} relative to the absence of inhibitor allows for the determination of site-specific changes in flexibility upon binding of the small molecule. Similar to the analysis of backbone dynamics, significant ΔS^2_{axis} values must be greater than two times the error in the fitted parameter. The calculated ΔS^2_{axis} values are shown below in Figure 5.5 for the ternary complexes with bound **1**, **3**, and **5**, where significant differences are highlighted with colored bars.
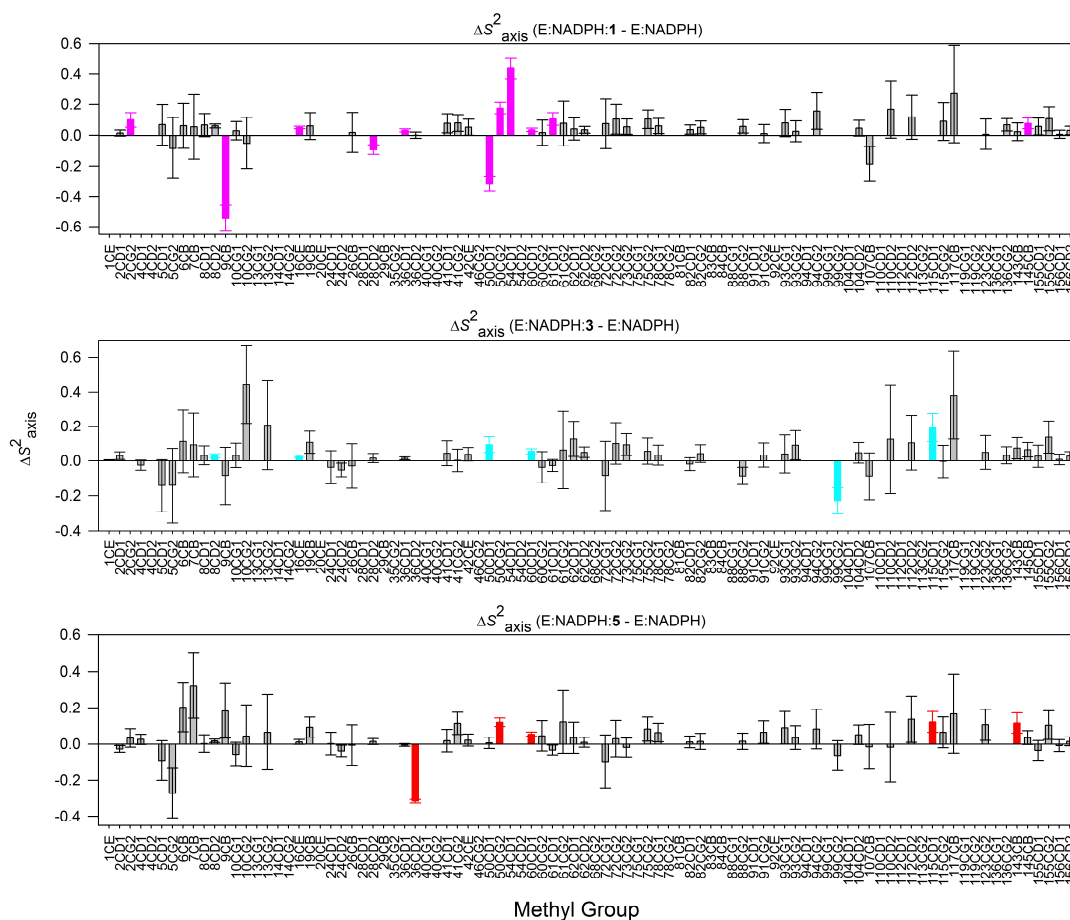
Figure 5.5. Changes in S^2_{axis} for three reduced-affinity antifolate complexes relative to E:NADPH. Significant changes in flexibility are highlighted in colored bars.

The majority of differences in side-chain flexibility upon inhibitor binding are positive, meaning a rigidification of ps-ns motions occurs. Methyl groups with significant

perturbations in flexibility are highlighted on the structure of DHFR in Figure 5.6, and shown

relative to previously studied complexes in the Lee Lab (79, 156).
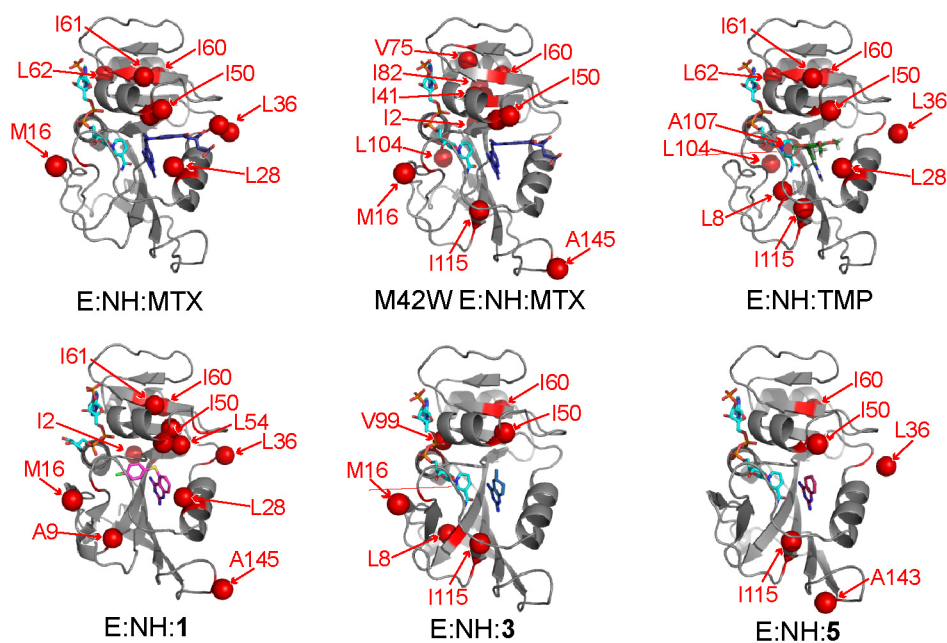
Figure 5.6. Significant changes in S^2_{axis} are highlighted in red spheres for six ternary antifolate complexes.

Several interesting observations should be noted. As mentioned in Chapter 2, the methyl

sites perturbed by MTX and TMP binding are essentially identical. In addition, I50 and I60

undergo significant changes in flexibility relative to the holoenzyme regardless of the

inhibitor bound. In many cases, M16, L36, I61, and I115 are also perturbed. Considering the

number of methyl groups with changes in flexibility, fewer sites are perturbed as K_i

increases. Therefore, reduced-affinity inhibitors do not quench as much side-chain flexibility

as those of high affinity. This trend is opposite of what was observed along the protein

backbone. When the dynamics of all methyl groups are considered, an increase in the

average ΔS^2_{axis} is observed with increasing K_i (Figure 5.7). So, although the number of

residues with significant changes in S^2_{axis} are fewer with reduced affinity, the magnitude of

ΔS^2_{axis} increases. This is opposite of what was observed for ps-ns backbone dynamics, possibly suggesting that backbone and side-chain dynamics on this timescale compensate for one another.
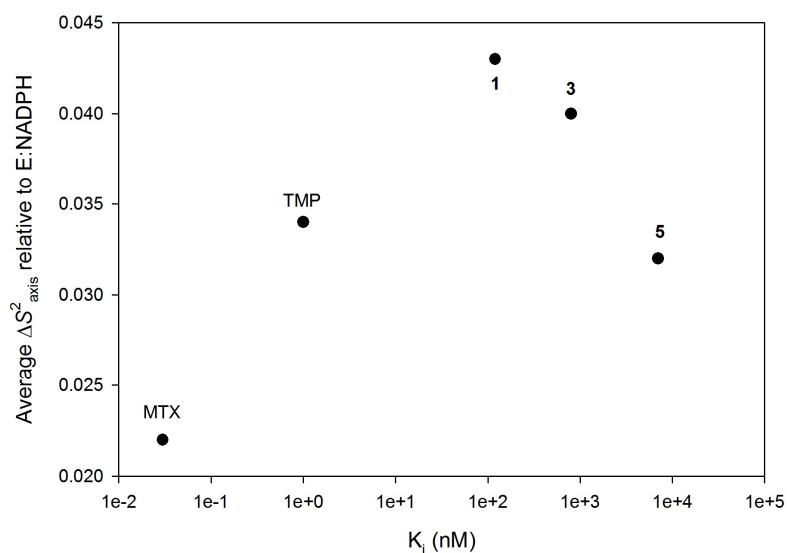
Figure 5.7. The correlation of ΔS^2_{axis} upon antifolate binding to K_i for the series.

It is instructive to compare the ΔS^2_{axis} values in a pair-wise fashion for all complexes studied (Table 5.5). Similar to the analysis of backbone flexibility, only methyl sites with measurable dynamics in all seven complexes were used in the correlations (38 reporters out of 92 possible sites) As noted previously (79), there is a correlation between the differences in dynamics caused by MTX and TMP binding ($R = 0.6$). Therefore, not only are the same sites perturbed by these two inhibitors, but the magnitudes of perturbation are similar. E:NADPH:**1** is not similar to any of the other complexes studied, which will be discussed further in section 5.3.5. The reduced-affinity complexes with **3** and **5** bound are most similar to wild-type and M42W E:NADPH:MTX, as noted for the backbone correlations and also for the raw S^2_{axis} values. In fact, E:NADPH:**5** is more similar to the M42W mutant than E:NADPH:MTX is to E:NADPH:TMP.

115

Reference complex	Comparison complex	R value
E:NADPH:MTX	E:NADPH:TMP	0.60
E:NADPH:**1**	E:NADPH:MTX	0.10
	E:NADPH:TMP	0.14
	E:NADPH:**3**	0.29
	E:NADPH:**5**	0.04
	M42W E:NADPH:MTX	0.13
E:NADPH:**3**	E:NADPH:MTX	0.55
	E:NADPH:TMP	0.44
	E:NADPH:**5**	0.47
	M42W E:NADPH:MTX	0.39
E:NADPH:**5**	E:NADPH:MTX	0.66
	E:NADPH:TMP	0.43
	M42W E:NADPH:MTX	0.66

Table 5.5. Pair-wise comparisons of ΔS^2_{axis} values for seven DHFR complexes studied in the Lee Lab.

5.3.3. Conformational entropy analysis

Side-chain order parameters for the seven DHFR complexes have been used to calculate conformational entropies in a site-specific manner (161). The average conformational entropy and standard deviation in the calculations are shown below in Figure 5.8. The greatest entropy values are observed for methionine methyl groups (residues 1, 16, 42, and 92). No large deviations in local entropies are seen across the protein sequence, which is not surprising as the correlations of raw S^2_{axis} values were quite high for the series of complexes studied (Table 5.4). This analysis of conformational entropy is incomplete at present; however, future work with this data will be discussed in section 6.5.
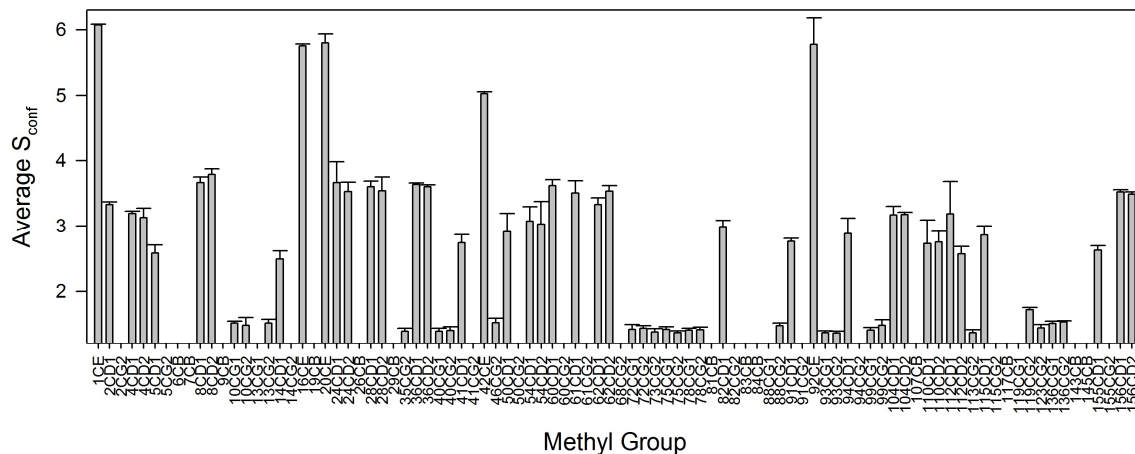
Figure 5.8. Average conformational entropies for the seven DHFR complexes.

5.3.4. A dynamics balancing act on the fast timescale

A summary of backbone and side-chain sites with significant changes in flexibility upon inhibitor binding are shown in Figure 5.9 for all six ternary complexes.

E:NH:MTX   M42W E:NH:MTX   E:NH:TMP

E:NH:**1**   E:NH:**3**   E:NH:**5**
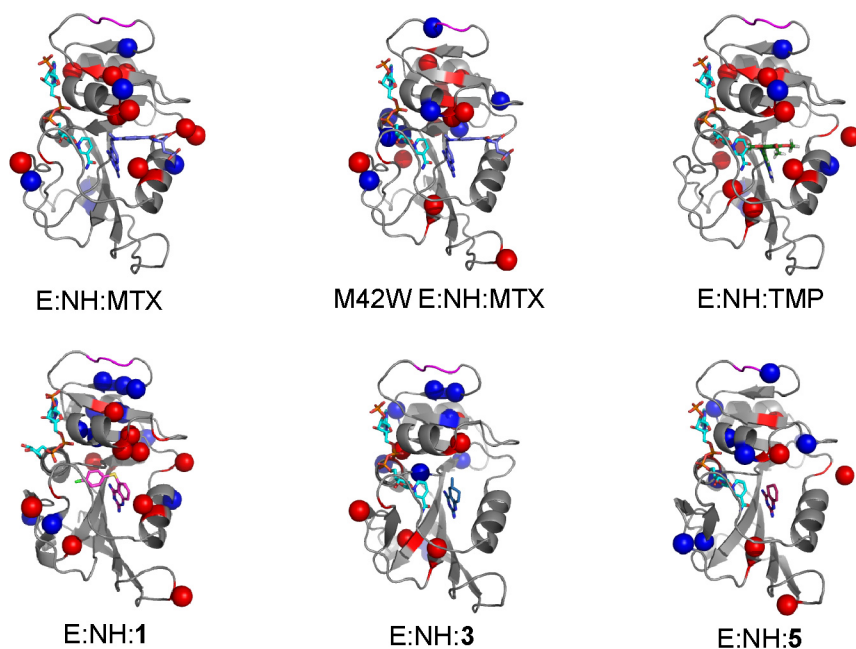
Figure 5.9. The combined significant differences in S^2 (blue) and S^2_{axis} (red) relative to E:NADPH for the six inhibitor complexes.

117

It is interesting to point out that the number of backbone and side chain sites perturbed remain constant (~15 sites) in the presence of MTX, TMP, **3**, and **5**. This is not the case for the M42W mutant (24 sites) and E:NADPH:**1** (23 sites). Bringing together observations mentioned in sections 5.3.1-2, the data suggest that backbone and side chain dynamics on the ps-ns timescale may compensate for one another: (i) the number of sites with significant deviations in S^2 increases with K_i with an overall decrease in the magnitude of rigidification versus K_i, and (2) the number of sites with significant deviations in S^2_{axis} decreases with K_i with an overall increase in the magnitude of rigidification versus K_i. This balancing act of ps-ns dynamics is contradictory to μs-ms dynamics, in which the number of sites with motion and the rate of motion increases with K_i. The compensatory motions suggest that DHFR has evolved to maintain a constant level of flexibility on the fast timescale within the closed state. From studying both backbone and side-chain dynamics across the series of inhibitors, we speculate that backbone dynamics correlate with kinetic movement of DHFR (increased flexibility with K_i) while side-chain dynamics correlate with ligand binding thermodynamics (decreased flexibility with K_i).

5.3.5. The anomalous M42W E:NADPH:MTX and E:NADPH:1 complexes

As mentioned previously, the E:NADPH:**1** and M42W E:NADPH:MTX complexes are dynamically different from the remainder of those studied. Both complexes have about ten more backbone and side-chain sites that are significantly perturbed relative to E:NADPH. Additionally, both complexes show decreases in S^2 at residues 67-69 of the adenosine binding loop. Their differences from the rest of the series and from each other necessitate a description of these anomalies.

In the M42W E:NADPH:MTX complex, a number of sites near to the site of mutation show differences in dynamics both along the backbone and side chains. This observation is expected, given that methionine and tryptophan are structurally very different, likely resulting in local protein packing differences (in spite of minimal changes in backbone structure (156)). Analysis of the changes in backbone flexibility in the M42W complex leads to a very surprising observation: all sites significantly perturbed relative to absence of inhibitor become more flexible. On the contrary, the differences in S^2 elicited by MTX are all rigidifications. In addition to this, the change in S^2 at residues 67-69 of the adenosine binding loop relative to E:NADPH is quite large in the M42W mutant – a greater than 0.1 reduction in S^2 values (Figure 5.1). Thus, the mutant complex causes a great increase in flexibility at the adenosine binding loop. This effect is about equal and opposite of the rigidification at residues 67-69 caused by MTX binding to wild-type DHFR.

As was observed on the μs-ms timescale, the ps-ns dynamics of E:NADPH:**1** are anomalous relative to the remainder of the inhibitor complexes studied herein. Firstly, the binding of **1** increases flexibility in the adenosine binding loop. Additionally, from the order parameter correlations made amongst the seven complexes, E:NADPH:**1** was found to be less similar to the other complexes studied, particularly in side-chain flexibility. In studying the structure and slow timescale dynamics of this complex, it was found that the bulky thiophenyl ring of **1** samples two different binding sites within the active site region of DHFR (40). However, this substituent had a preferred binding orientation in solution, in which it was oriented in the substrate binding site and pointed toward helix-C and the loop following said helix. Interestingly, ps-ns motions in this region show significant rigidification. More specifically, all significant backbone perturbations from the absence of

119

drug are increases in S^2, including V40 which closely contacts the thiophenyl ring in its solution-preferred pose. Side chain rigidification is also seen in this region for L36, I50, and L54. This is somewhat surprising since we know these sites are undergoing motion on the μs-ms timescale. However, ps-ns dynamics studies only capture motions within the ground state of the conformational ensemble. On this note, no residues within close vicinity of the solution-preferred thiophenyl binding pose were fit to models 3 or 4 during the Lipari-Szabo analysis.

5.3.6. Reduced-affinity antifolates dynamically mimic M42W mutation

When comparing the backbone and side-chain sites significantly perturbed by the binding of reduced affinity inhibitors **1**, **3**, and **5** relative to the M42W mutant (Figure 5.9), no great similarities are observed. However, the pair-wise correlations of order parameters, both raw values and differences from the holoenzyme, suggest a similarity between the M42W mutant and the binding of reduced affinity antifolates.
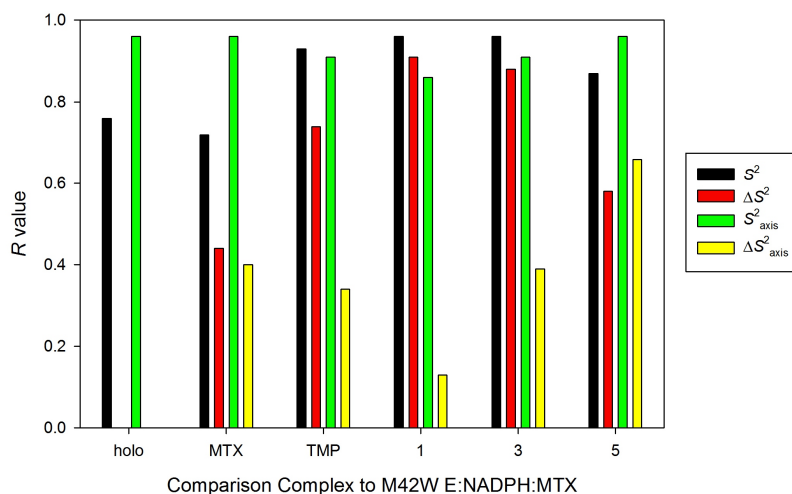
Figure 5.10. Correlation coefficients for comparing order parameters to M42W E:NADPH:MTX.

120

When comparing raw backbone S^2 values, ternary complexes with TMP, **1**, **3**, and **5** agree well ($R > 0.8$) with the M42W mutant. This similarity narrows to only E:NADPH:**1** and E:NADPH:**3** when comparing ΔS^2 relative to the holoenzyme. All six complexes have highly similar raw S^2_{axis} values when compared to M42W E:NADPH:MTX. The best agreement with the M42W complex when considering ΔS^2_{axis} values is E:NADPH:**5**.

Considering the large discrepancy in ps-ns flexibility between M42W and wild-type E:NADPH:MTX, the reduced-affinity inhibitor complexes are better approximations to mimicking the mutation. This leads to the possibility of whether the binding affinity of MTX to M42W is significantly reduced, similar to **3** and **5** for wild-type DHFR. E:NADPH:**3** and E:NADPH:**5** are arguably the best matches dynamically to M42W E:NADPH:MTX. The reverse is also true – M42W E:NADPH:MTX is generally the best matched complex to both E:NADPH:**3** and E:NADPH:**5** compared to the other studied complexes. This dynamic grouping of complexes with similar fast timescale dynamics is reiterated in slow timescale studies, in which the sites with R_{ex} in E:NADPH:**5** (Chapter 4) are highly similar to those identified in M42W E:NADPH:MTX (156).

5.4. Concluding Remarks

It has been previously suggested that the fast timescale dynamics of DHFR are invariable within the context of the same Met20 loop conformation (47, 48, 50). This claim comes from analysis of backbone and side-chain order parameters on physiological complexes in either the Met20 loop closed or occluded conformation. However, a systematic study of ps-ns dynamics in a series of complexes all within the same structural state has not been previously reported to question the above hypothesis. From the data, it is clear that

DHFR does dynamically sense differences in bound ligand on the ps-ns timescale. A different pattern of sites is perturbed dynamically by each antifolate, with only several sites in common amongst all studied complexes. While the magnitudes of changes in flexibility are rather small, the effects appear to correlate with ligand binding affinity: (1) more sites with significant changes in backbone flexibility were observed with increasing K_i, (2) the magnitude of backbone rigidification decreases exponentially with K_i, (3) fewer sites with significant changes in side-chain flexibility were observed with increasing K_i, and (4) the magnitude of side-chain rigidification generally increases with increasing K_i. Additionally, backbone flexibility at residues 67-69 of the adenosine binding loop are perturbed by the binding of small molecule antifolates, with higher affinity inhibitors causing the greatest quenching of motion.

From the initial analysis of the data presented, three functional dynamic groupings are suggested: (1) the MTX and TMP group, (2) the reduced-affinity antifolate and M42W mutation group, (3) the highly perturbed E:NADPH:**1** group. Group 1 is based on the high similarity in sites perturbed and the magnitude of perturbations caused by MTX and TMP binding, both along the backbone and side chains. Group 2 is based on the dynamic similarity of reduced-affinity complexes with bound **3** and **5** relative to M42W E:NADPH:MTX (*R* value correlations tabulated in this chapter). Group 3 represents the most anomalous complex, which differs greatly in both the identity of sites perturbed and the magnitude of perturbations, especially in ΔS^2_{axis}. These groupings are further supported on the slow timescale: Group 1 complexes show identical patterns of slow motions and rates of conformational exchange; Group 2 complexes are similar in the identity of flexible residues and have faster rates of exchange; The group 3 complex is very different on the slow

122

timescale, with widespread motions that are not present in the other studied antifolate

complexes. This similarity of complex groupings on the two timescales suggests a link

between fast and slow motions in DHFR within the closed state.

Chapter 6

Outlook and Future Directions

In this study, we have taken a medicinal chemistry approach to probing the dynamics of dihydrofolate reductase when bound to inhibitors that cover a broad range of binding affinities. Three main questions were to be addressed: (1) Would the dynamics of DHFR be affected by the chemical structure of bound ligands within the same conformational state, (2) would dynamics be modulated by the binding affinity of bound ligands, and as a result, (3) could we identify a link between internal motions of the enzyme and binding affinity or kinetics of binding?

Regarding question (1), we clearly demonstrate in Chapter 3 that the dynamics of DHFR are sensitive to bound ligand structure. This case is extreme, in that the inhibitor itself is mobile; however, we show that widespread changes in μs-ms dynamics are evident in the presence of this particular small molecule. Differences in motion depending on bound ligand are also reported in Chapter 4, where the binding of a series of tetrahydoquinazolines effects similar residues, but the pattern is not identical. This point is also noted in Chapter 5, as ps-ns dynamics vary with bound inhibitor. These observations are in stark contrast to Chapter 2, in which TMP and MTX binding were shown to elicit essentially identical motions in DHFR. The main difference observed between TMP and MTX binding was on the fast timescale,

where inhibitor binding is 'sensed' at the same sites, but the correlation between the changes in flexibility is not very strong.

To probe point (2), the combination of data from Chapters 2-4 demonstrates that DFHR's μs-ms dynamics are indeed sensitive to inhibitor binding affinity. Particularly in Chapter 4, we bring together all of this data to show that a strong correlation exists between the rate of conformational switching in DHFR and the K_i of bound ligands across the entire series of inhibitors studied. Although additional data and further data analysis is needed, the suggestion of a correlation between ps-ns dynamics and bound inhibitor K_i is reported in Chapter 5. Here we observed a balancing act of backbone and side-chain flexibility and the thought of fast motions compensating for those on the slow timescale.

Question (3) is elegantly discussed in Chapter 4, in which we show that a structurally similar excited state is sampled by a common grouping of residues in DHFR in the presence of the series of small molecule inhibitors studied. The structure was found to be novel, relative to the excited state of the same grouping of residues in physiological complexes (bound to folate-derived ligands). Additionally, this excited state is sampled at different rates depending on the bound inhibitor, and this rate of conformational switching correlates well with both binding affinity and the kinetic dissociation rate of the ligands.

A number of questions for further probing come from this body of work, as discussed below.

6.1. Probing the utility of 1 against TMP-resistant bacterial strains

In Chapter 3, the 2,4-diaminoquinazoline compound **1** was shown to elicit μs-ms dynamics in DHFR consistent with its thiophenyl moiety inserting into the nicotinamide

binding site to a small degree in solution. This excited state pose, also observed crystallographically and through use of molecular modeling techniques, is made possible by the concomitant switching of the Met20 loop from closed to occluded. The excited state binding pose of **1**'s thiophenyl moiety is novel for inhibitors of *E. coli* DHFR. This binding pose was observed for an analogous inhibitor of *L. casei* DHFR, but unlike our results, it was found there to be the predominant binding pose based on strong electron density for both ligand and protein in the ternary complex (123). Numerous studies have shown the existence of mutations within the substrate binding site that result in resistance to TMP (75, 76). Because **1** samples two different binding poses within the active site and is still a high affinity inhibitor, it would be interesting to examine whether **1** would be effective against mutations that confer TMP resistance. As discussed in Chapter 3, the ability of a small molecule to sample multiple bound conformations has lead to overcoming drug resistance in several cases (e.g., HIV reverse transcriptase) (162). Although **1** is not as high in affinity for DHFR as TMP, its sampling of a novel binding pose could prove useful against TMP-resistant bacterial strains. Mutations that confer resistance to anitfolates concentrate within the substrate binding site, not the cofactor binding site. It is reasonable to believe that mutations within the nicotinamide binding site are unlikely to occur, as DHFR necessitates the binding of reduced cofactor for catalysis.

6.2. Expanding the correlation of $k_{conf,forward}$ to K_i and k_{off}

The data presented in Chapter 4 show an exponential relationship between internal motions in DHFR and both K_i and k_{off}. This relationship appears to hold over a range of six and five orders of magnitude for K_i and k_{off}, respectively. However, only six points

constitute the correlation. Several methods could be used to increase the number of data points. Two related methods are global, systematic perturbations to the complexes: temperature variations and the use of chaotropic agents. Since the stopped-flow assay described for k_{off} determination is faster to perform that K_i assays, initial tests of varying temperature and the addition of urea have been conducted as part of this work, although the data has not been presented herein, to modulate k_{off}. My preliminary work with temperature variations (using compound **3** and **5**) demonstrated slight modulations (~ 10% increase) in k_{off} over the range of 25-30 °C. Studies of k_{off} in the presence of urea over a 0-2 M range (using compound **5**) showed that k_{off} could be increased up to 65% under such conditions. The combination of approaches, using increased temperature and urea can serve to double k_{off} (using compound **5** at 35 °C and 2 M urea). However, in conducting relaxation dispersion experiments on E:NADPH:**5** at 35 °C in 2 M urea/NMR buffer, we find that degradation of DHFR occurs more rapidly and becomes significant over the four day course of data collection at 700 MHz. Slow timescale motions were identified at residues very similar to what was reported in Chapter 4; however, global fitting of the data was challenging and yielded a vastly increased $k_{conf,forward}$ that was far from expected. Therefore in the future, such an extreme change in conditions should be avoided. Aiming to only mildly modulate k_{off} via temperature and chaotropic agents is likely a wiser strategy. The use of urea and increases in temperature both serve to increase k_{off}. One might also be interested in slowing dissociation, for which, decreases in temperature would be valuable. For example, k_{off} for **6** could be decreased by lowering the temperature at which data is collected. This change in condition would likely be better tolerated by DHFR than the extreme case presented above. Although not extending the dynamic range of the correlation, slowing k_{off} for **6** could

contribute a data point between that of **5** and **6** under standard conditions on the $k_{conf,forward}$

versus k_{off} plot.

A third method to increase the number of data points in the correlation of internal

motions to binding affinity or off-rate is mutagenesis. For example, one may choose to work

with one inhibitor reported herein, but study that small molecule while bound to several

DHFR mutants that increase or decrease K_i or k_{off}. Mutations are not as straight forward as

other approaches, in that structural changes could result in the protein, and these structural

changes could underlie differences in observed dynamics. For example, the R44L mutant of

DHFR has been reported to cause a six-fold increase in dissociation of H_4F (163). Although

not presented herein, k_{off} of **3** from R44L E:NADPH:**3** was studied by stopped-flow

fluorescence experiments. The off-rate for **3** was found to be unchanged from wild-type

DHFR. It turns out that a number of chemical shift changes in E:NADPH:**3** also occur upon

mutation of R44L, suggestive of structural change. In addition, it has been determined that

the R44L mutation modulates kinetics of the catalytic cycle with possible differences in

conformations sampled (163). Thus, the reported increase in k_{off} was calculated and not

directly observed via competition experiments. This example speaks to the issues that can be

encountered when using mutagenesis as a biochemical tool, thus suggesting that this method

of modulating k_{off} should be attempted with caution. In addition, the effect of a mutation on

k_{off} is not predictable whereas other suggestions mentioned (temperature and chaotropic

agents) do provide a degree of expected modulation of K_i or k_{off}.

A fourth method for increasing the number of points on the correlation plot would be

to study different inhibitors, and not necessarily inhibitors that are highly similar in structure.

The antifolates used in the study were of different structural classes, although still quite

similar in chemical structure (i.e., of the pteridine, pyrimidine, quinazoline and tetrahydroquinazoline classes, but all containing the 2,4-diaminopyrimidine pharmacophore). It would be interesting to expand the correlation by studying molecules with larger structural differences. For example, MJC-7 shown in Figure 1.8 is structurally different than the antifolates used in the $k_{conf,forward}$ correlations. This inhibitor would be interesting to study, although there are several issues with it: (1) it samples a novel portion of the active site and thus might result in structural changes that overlie changes in dynamics, and (2) it is a very high affinity inhibitor that doesn't expand the dynamic range of the correlation. Trimextrexate or MJC-8 could be studied to add a data point in the correlation between TMP and **1**, although they are structurally similar to compounds already used for the correlation. MJC-9 offers a somewhat different structure, but it is still of the pyrimidine class. Triazole antifolates could pose as an interesting suggestion for a different class of inhibitor. Since MTX and TMP are generally regarded as the highest affinity inhibitors of DHFR, antifolates with weaker K_i values would be helpful to expand the dynamic range of the correlation. Identifying poor inhibitors from the literature can be challenging.

6.3. Determining the structure of the novel excited state

In Chapter 4, fitting of relaxation dispersion data on the series of complexes studied yields essentially identical $\Delta\omega$ values for a set of twelve residues within the active site region, regardless of the inhibitor bound. We discussed previously that this state is of novel structure relative to the excited state sampled by complexes bound to folate-like ligands. Future work toward identifying the structure of the excited state sampled in the presence of antifolates would be interesting, as the novel excited state could be exploited in structure-

based drug design. Significant differences in the excited state structure could drive design of inhibitors that would destabilize such a conformation, thus increasing residence times of ligands. Much effort by Kay and co-workers has been devoted to the issue of determining structures for excited states sampled in solution on the μs-ms timescale (154, 155). Following their work, we may be able to identify the structure of the novel excited state and compare it to the ground state.

If this group of antifolate consensus residues is indeed en route to inhibitor dissociation, perturbations to this small network would affect k_{off}. Therefore, an interesting perspective on future work would be to study mutations within the antifolate consensus group. Assuming that the chosen mutations do not preclude antifolate binding, differences in both the rate of conformational exchange and the structure of the excited state could be expected. Making mutations to each of consensus sites individually could even help to identify if one of the sites is the keystone of the correlation we observed.

6.4. How is product released from the occluded state?

The excited state structure sampled by ternary antifolate complexes differs from those sampled by physiological complexes, in particular the E:NADPH:H_4F product release complex, suggesting that product release and antifolate dissociation occur via different mechanisms. This is not entirely surprising, as all of the complexes studied herein are within the context of the Met20 loop closed conformation while the product release complex possesses the occluded conformation. Based on the exact matching of $k_{conf,forward}$ for Met20 loop switching in E:NADPH:H_4F with k_{cat}, it is highly possible that the Met20 loop actively participates in the dissociation of H_4F (125). In further support of differing mechanisms for

product and antifolate dissocation, only three residues within the antifolate consensus group also possess slow motion in the E:NADPH:H_4F complex. Of these three in common, residues 30 and 31 do show similar fits for $\Delta\omega$ relative to the antifolate complexes. However, similar $\Delta\omega$ fits are seen for other complexes in which ligand is bound within the substrate binding site (E:H_4F and E:N^+:H_4F), suggesting these motions are connected to the occupancy of that binding site. From this it is possible, however, for Met20 loop motion to be necessary for H_4F release in conjunction with some causative motion within the antifolate consensus group. This would suggest that the causative motion is all that is required for antifolate dissociation.

To approach answering the question of how product dissociation occurs, the methodologies described previously in section 6.1 would be useful. Specifically, temperature variations, addition of chaotropic agents, and mutagenesis would be useful in modulating k_{off} for H_4F. Some preliminary work towards this goal has been completed, although not reported herein.

6.5. Thorough analysis of ps-ns data

As mentioned in Chapter 5, ps-ns timescale flexibility of DHFR in the presence of reduced-affinity antifolates have only been characterized for complexes with **1**, **3**, and **5** bound. Thus, backbone and side-chain dynamics could be studied for the additional complexes with **2**, **4**, and **6** bound. However, working with the data has been collected at present, a more thorough analysis is needed toward the idea of functional or dynamic groupings of complexes. Parameters fitted from the Lipari-Szabo analysis should be analyzed for all complexes on a per residue and grouping of residues basis to look for

patterns that correlate with K_i. This would point to sites, on an atomic level, that are perturbed by inhibitor binding in a predictable manner.

Side-chain order parameters can be converted into local entropy values based on the method described in Chapter 5 (161). While this conversion has been done for all seven complexes discussed herein (E:NADPH bound to nothing, MTX, TMP, or **1**-**6**, and M42W MTX), no comparisons or correlations in the data have been made. Furthermore, the data are more meaningful when compared to data on the thermodynamics of ligand binding. Some work with isothermal titration calorimetry (ITC) was performed as part of this work, but the results were not reliable or useful. Thus, a serious collection of ITC data for inhibitor binding would be valuable to the study. From ITC data, one can determine if ligand binding is entropically or enthalpically favored. Given the great structural similarity of the series of ligands studied, particularly the THQ compounds, we expect binding to be driven entirely by either enthalpy or entropy, and not a mix of the two across the series. Interestingly, local entropies calculated from side-chain order parameters can be compared to global entropy of binding from ITC. This type of comparison could allow for the identification of sites directly involved in modulating the thermodynamics of inhibitor binding.

ITC data would be particularly valuable in the case of E:NADPH:**1**. As described in Chapter 5, large increases in order parameters are observed for both backbone and side-chain sites. This is in great contrast to the extensive motion observed on the slow timescale, reported in Chapter 3. Thus, it appears that flexibility on the fast timescale decreases to compensate for the extreme slow motions. This would be more definitively shown by looking at ITC data and conformational entropies calculated from S^2_{axis}.

6.6. Binding affinity and kinetics of MTX binding to M42W DHFR

Randall Mauldin previously characterized the μs-ms and ps-ns timescale dynamics of M42W E:NADPH:MTX in the Lee Lab (156). His results were compared directly to the wild-type E:NADPH:MTX complex. Herein, I have compared his M42W data to wild-type complexes bound to inhibitors other than MTX. It is interesting to note that slow motion was observed at two groupings of residues in M42W E:NADPH:MTX – (1) the antifolate consensus sites, fitting to a slower rate of exchange, and (2) sites within helix C and loop proceeding this helix, fitting to a faster exchange rate. The fitted $\Delta\omega$ values for the antifolate consensus group are essentially identical to what is reported in Chapter 4 for the eight wild-type inhibitor complexes studied. Thus, it is tempting to add the M42W E:NADPH:MTX mutant as a point in the $k_{conf,forward}$ vs. K_i or k_{off} plots. Binding affinity and kinetics of binding studies for MTX and the M42W mutant have not been conducted, but would be useful for this study. Based on the relationship between $k_{conf,forward}$ and K_i, one would expect MTX to have a K_i value of about 5 μM for M42W E:NADPH ($k_{conf,forward} = 30$ s^{-1}). From this, it follows that k_{off} for MTX from the mutant would be expected to be ~3 s^{-1}.

Additionally, M42W E:NADPH:MTX ps-ns dynamics relative to wild-type holoenzyme and various ternary antifolate complexes are compared in Chapter 5. Some correlations between wild-type complexes and K_i values have been made. Although M42W E:NADPH:MTX appears to be an anomaly on this timescale, it would be interesting to know the K_i value for MTX for the purpose of making more meaningful correlations about patterns of backbone and side-chain flexibility. This would especially useful if a large matrix of all DHFR dynamics data collected within the Lee Lab were to be constructed, as discussed below. The speculated K_i and k_{off} values for M42W could also explain why the mutant

E:NADPH:MTX complex appears so dynamically similar to E:NADPH:**5** on both the fast

and slow timescales.

6.7. An exclusive matrix of data toward multi-timescale correlations of motion

Taken together, the new data presented herein, in combination with the work of

Randall Mauldin, represents a unique set of data that compares to what exists in the literature

for only calmodulin (22, 24, 25, 158, 164, 165). Because only ps-ns dynamics data have

been published for calmodulin, our data is even more distinctive in that we have

characterized μs-ms <u>and</u> ps-ns dynamics in the same system. As mentioned previously, slow

timescale motions are important to and implicated in biological function of proteins and

enzymes. It has been suggested that, while fast timescale motions are not directly relevant to

function, they may lubricate or form a foundation for those motions that occur on the slow

timescale (15). We are in the unique position of being able to search for such a correlation

between fast and slow motions. For further analysis and drawing of correlations within the

two timescales of motion or across timescales, one would ideally construct a large matrix

with the data. We envision this matrix would include information from general biochemistry

studies (K_i, k_{off}, ΔG, ΔH, and $T\Delta S$), slow timescale dynamics studies (k_{ex}, p_A, p_B, $k_{conf,forward}$,

$k_{conf,reverse}$, and $\Delta\omega$) and fast timescale dynamics studies (S^2, S^2_{axis}, ΔS^2, ΔS^2_{axis}, R_{ex}, τ_e, and

$\tau_{e,axis}$). Related to demonstrating a correlation between fast and slow timescale dynamics, we

may also be able to show functional and/or dynamic grouping of complexes. This idea was

introduced in Chapter 5, given the suggestion that reduced-affinity antifolates appear to

dynamically mimic the M42W mutation, while being different from MTX and TMP

responses and also from the response of binding **1**. The all-inclusive matrix of data could

link complexes functionally or dynamically on multiple timescales. The approach could also

link just subsets or groupings of residues in a similar manner across timescales.

Appendices

Chapter 2

2.1. ^{15}N Relaxation dispersion fitted parameters for E:NADPH:TMP.

Residue	k_{ex} (s^{-1})			p_B (%)			$\pm \Delta\omega$	$|\Delta\omega|$ (ppm)			χ^2
7	458.7	$\pm$	165.2	2.3	$\pm$	0.4	-	0.929	$\pm$	0.251	7.60
8^a	1357.6	$\pm$	362.5	2.7	$\pm$	0.5	-	1.789	$\pm$	0.237	6.90
9	458.7	$\pm$	165.2	2.3	$\pm$	0.4	-	3.370	$\pm$	0.677	9.67
10	458.7	$\pm$	165.2	2.3	$\pm$	0.4	+	1.351	$\pm$	0.570	16.6
28	458.7	$\pm$	165.2	2.3	$\pm$	0.4	-	0.950	$\pm$	0.207	18.6
29	458.7	$\pm$	165.2	2.3	$\pm$	0.4	+	1.541	$\pm$	0.431	12.2
30	458.7	$\pm$	165.2	2.3	$\pm$	0.4	+	1.175	$\pm$	0.913	9.27
31	458.7	$\pm$	165.2	2.3	$\pm$	0.4	+	1.247	$\pm$	0.273	9.74
111	458.7	$\pm$	165.2	2.3	$\pm$	0.4	+	1.267	$\pm$	0.324	12.5
112	458.7	$\pm$	165.2	2.3	$\pm$	0.4	-	1.270	$\pm$	0.312	8.33

^{a}Local fit reported.

2.2. ^{15}N relaxation model-free parameters fit for the backbone of E:NADPH:TMP.

Residue	S^2_s	$S^2_{s\,err}$	τ_e (ps)	τ_e err	S^2_f	$S^2_{f\,err}$	R_{ex}	R_{ex} err	χ^2
1									
2	0.8629	0.0129	14.60	13.70					1.82
3	0.8628	0.0112	0.53	2.12					3.96
4	0.8767	0.0155					0.70	0.45	1.27
5	0.905	0.01	24.00	17.60					1.34
6	0.9067	0.0175	3.29	8.96					1.50
7	0.8301	0.0147	2.05	5.13					2.67
8	0.8601	0.0133					1.01	0.36	1.57
9	0.8401	0.0218					2.71	0.64	2.66
10	0.871	0.0124					1.71	0.35	1.85
11									
12	0.8658	0.0098	7.40	9.49					0.70
13	0.8704	0.0092					0.70	0.25	1.37
14	0.8838	0.0167	14.00	18.50					1.14
15	0.8923	0.0111	0.11	1.27					8.69
16	0.89	0.0085	5.54	7.98					1.58
17	0.7953	0.0067	6.48	3.77			0.37	0.18	14.50
18	0.8763	0.0129	1.96	5.26					1.27
19	0.8627	0.0057	19.30	8.32					2.33

Residue	S^2_s	$S^2_{s\,err}$	τ_e (ps)	τ_e err	S^2_f	$S^2_{f\,err}$	R_{ex}	R_{ex} err	χ^2
20	0.8314	0.0068	4.94	5.82					1.30
21									
22									
23	0.8284	0.0388	14.70	18.50					2.48
24	0.7969	0.0132	19.00	10.70					3.63
25									
26	0.9057	0.0084	8.93	11.20					10.30
27									
28	0.8989	0.0114	0.48	2.54					4.95
29	0.916	0.0099	9.06	13.90					5.54
30	0.8743	0.0126	14.80	14.50					1.03
31	0.9189	0.0148	19.20	23.00					0.58
32									
33	0.9021	0.0077	0.41	1.97					3.62
34	0.953	0.0187	1860	22000	0.9035	0.1085			5.79
35	0.877	0.01	2.84	6.00					2.96
36	0.8735	0.0129					1.21	0.43	0.15
37	0.8593	0.0136	25.40	15.60					3.82
38	0.8289	0.0068	14.20	6.67					5.02
39									
40	0.8787	0.01	7.67	9.91					2.00
41	0.8223	0.0148					0.66	0.41	0.65
42	0.9249	0.0091	2.02	6.08					4.52
43	0.868	0.0102	1.07	3.45					5.86
44	0.8694	0.012					0.92	0.28	0.33
45	0.885	0.0122					1.85	0.31	3.03
46	0.8436	0.0145					0.62	0.34	2.06
47	0.8913	0.0125					0.67	0.30	1.95
48	0.8688	0.0119					0.84	0.29	8.09
49	0.8537	0.0069	8.43	7.44					1.70
50	0.8907	0.0048	4.14	5.64					1.62
51	0.8744	0.008	3.31	5.89					2.23
52	0.8394	0.0055	18.70	6.85					2.00
53									
54	0.8429	0.0115	6.23	8.04					1.80
55									
56									
57	0.893	0.0068	0.08	0.76					9.97
58	0.8042	0.0089	4.12	5.37					11.40
59	0.8279	0.0209	2.21	5.36					1.33
60	0.845	0.0088	4.95	6.89					0.37
61	0.8776	0.0086	2.61	5.56					1.39
62	0.8635	0.0094	20.60	12.10					1.05
63	0.8682	0.0065	11.80	8.57					8.70
64	0.8518	0.0141	8.82	9.66					0.44

Residue	S^2_s	$S^2_{s\,err}$	τ_e (ps)	τ_e err	S^2_f	$S^2_{f\,err}$	R_{ex}	R_{ex} err	χ^2
65	0.8707	0.0078	10.50	8.92					0.78
66									
67	0.7913	0.009	2100.00	152.00	0.6998	0.0103			2.61
68	0.9323	0.0797	700.00	456.00	0.727	0.0276			0.30
69	0.9152	0.0854	248.00	352.00	0.6794	0.0359			5.94
70	0.7855	0.0339	6.55	10.30					3.19
71	0.8737	0.009	3.57	6.15					11.10
72	0.8532	0.0059	20.40	7.89					0.83
73	0.8541	0.0089	3.98	6.12					5.00
74	0.8171	0.0067	3.84	4.66					1.21
75	0.8827	0.0075	2.09	4.82					2.85
76	0.8361	0.0078	23.10	9.59					2.33
77	0.9522	0.0202	46.40	20.40	0.9212	0.0231			8.26
78	0.8945	0.0098	13.80	13.80					3.39
79	0.8833	0.0059	0.04	0.45					25.10
80	0.9057	0.0071	3.62	6.96					5.17
81	0.9023	0.0052	12.40	9.53					4.71
82	0.8602	0.009	18.50	12.20					2.24
83	0.9039	0.0062	2.32	5.32					3.89
84									
85	0.8558	0.0079	2.68	5.06					0.56
86	0.8406	0.0063	0.97	2.42					3.53
87	0.6693	0.0695	9.97	11.50					1.05
88	0.774	0.0988	453.00	667.00	0.7649	0.0609			204.00
89									
90									
91	0.8619	0.0133	2.25	5.76					3.53
92	0.8832	0.0106	10.70	11.80					1.16
93	0.85	0.0099	1.47	3.76					2.54
94	0.8902	0.012	2.75	6.81					1.46
95	0.8969	0.0076	13.10	11.80					1.02
96	0.8498	0.0088	0.92	2.80					3.05
97	0.8687	0.0109	22.10	14.80					0.53
98	0.8934	0.0073	7.16	8.84					8.60
99	0.8892	0.0074	16.00	11.90					1.99
100									
101	0.8881	0.006	1.02	3.10					4.41
102	0.8628	0.0071	0.96	2.82					5.84
103	0.8372	0.0081	1.05	2.89					9.89
104	0.8921	0.0071	17.50	12.50					5.04
105									
106	0.899	0.0248	6580.00	43100.00	0.8669	0.4759			12.50
107	0.8667	0.0064	10.80	8.85					5.55
108	0.8729	0.0147	7.89	12.00					1.91
109	0.8683	0.0129					0.66	0.40	0.34

Residue	S^2_s	$S^2_{s\,err}$	τ_e (ps)	τ_e err	S^2_f	$S^2_{f\,err}$	R_{ex}	R_{ex} err	χ^2
110									
111	0.8473	0.0173	10.70	13.10					2.10
112	0.8588	0.012	7.25	9.43					6.03
113									
114									
115	0.8387	0.014	33.70	15.80					0.15
116	0.8848	0.0084	1.30	3.87					10.20
117	0.8118	0.0052	2.56	3.81					4.10
118	0.7968	0.006	3.62	4.36					11.90
119	0.7197	0.0108	20.00	6.26			0.52	0.26	1.86
120	0.9366	0.0094	44.80	6.50	0.7996	0.006			34.70
121	0.7515	0.0044	30.20	3.99					8.86
122	0.8584	0.0127	17.50	15.30					1.34
123	0.8414	0.0067	7.05	6.77					5.77
124	0.7192	0.0561					3.18	1.59	4.69
125	0.8788	0.0116	2.30	5.70					2.27
126									
127									
128	0.5873	0.0092	37.10	3.03			3.84	0.26	5.15
129	0.8438	0.0154	13.50	13.70					5.07
130									
131	0.8107	0.0083	28.40	9.00					2.28
132	0.8443	0.0082	22.40	10.20					5.14
133									
134	0.8367	0.0084	13.90	9.45					0.56
135									
136									
137	0.8446	0.0066	16.10	8.65					8.35
138	0.8496	0.0068	20.70	7.98					13.40
139	0.8252	0.0098	5.28	6.92					7.00
140	0.912	0.017	35.70	18.60	0.901	0.0205			30.40
141	0.8493	0.0087	7.61	7.60					2.59
142	0.8045	0.0073	8.38	6.26					32.50
143	0.9155	0.0179	67.00	11.30	0.8935	0.0178			12.10
144	0.8449	0.0073	10.90	8.71					3.01
145									
146	0.9224	0.0363	31.90	17.00	0.8703	0.0362			42.30
147	0.8102	0.0067	12.40	5.97					7.24
148	0.9137	0.0237	129.00	960.00	0.8893	0.0248			17.80
149	0.8412	0.0075					1.07	0.20	8.87
150	0.8303	0.0067	2.24	4.16					3.71
151	0.9068	0.0083	3.40	6.99					8.87
152	0.8502	0.011	1.71	4.28					6.18
153	0.8622	0.0124	10.50	11.60					0.94
154	0.8422	0.0124	0.02	0.22					10.80

Residue	S^2_s	$S^2_{s\,err}$	τ_e (ps)	τ_e err	S^2_f	$S^2_{f\,err}$	R_{ex}	R_{ex} err	χ^2
155	0.8534	0.0138	6.60	9.51					1.46
156									
157									
158	0.8478	0.0146	48.00	13.10			0.79	0.42	2.93
159	0.9182	0.0467	420.00	667.00	0.8564	0.0167			64.30

2.3. ^{2}H relaxation model-free parameters fit for the side chains of E:NADPH:TMP.

Methyl	S^2_{axis}	S^2_{axis} err	τ_e	τ_e err	χ^2
1CE	0.104	0.002	16.20	0.16	44.50
2CD1	0.447	0.014	17.90	1.17	0.77
2CG2					
4CD1					
4CD2	0.521	0.081	172.00	23.80	0.52
5CD1	0.873	0.089	29.60	5.53	1.48
5CG2	0.931	0.085	36.90	5.93	0.33
6CB	0.929	0.104	60.90	9.05	1.39
7CB	0.798	0.115	54.10	10.50	0.25
8CD1	0.344	0.052	63.10	10.10	0.13
8CD2					
9CB	0.832	0.472	52.20	343.00	0.52
10CG1					
10CG2	0.64	0.115	28.60	7.95	0.48
13CG1					
13CG2	0.627	0.205	109.00	43.80	1.55
14CD1	0.798	0.053	7.71	2.94	0.01
14CG2	0.856	0.055	27.30	3.28	2.17
16CE	0.322	0.02	5.33	0.35	120.00
19CB	0.937	0.041	21.60	1.64	2.88
20CE	0.495	0.018	14.40	1.00	0.88
24CD1					
24CD2	0.298	0.052	36.00	8.82	0.65
26CB	0.914	0.101	51.50	8.41	2.24
28CD1	0.595	0.059	36.80	5.18	0.11
28CD2					
29CB					
35CG2	0.887	0.064	18.80	3.17	0.89
36CD1	0.265	0.008	58.00	1.40	1.66
36CD2	0.287	0.009	54.60	1.43	5.35
40CG1	0.914	0.058	48.50	4.95	0.07
40CG2	0.88	0.05	44.70	4.02	0.59
41CD1	0.773	0.039	20.40	2.23	0.37

Methyl	S^2_{axis}	S^2_{axis} err	τ_e	τ_e err	χ^2
41CG2	0.866	0.034	31.90	2.19	0.04
42CE	0.88	0.019	4.18	0.65	2.20
46CG2					
50CD1	0.713	0.033	17.60	1.74	0.40
50CG2	0.806	0.023	18.50	1.14	0.77
54CD1	0.649	0.04	36.20	3.29	0.96
54CD2					
60CD1	0.317	0.009	28.00	1.08	3.19
60CG2	0.853	0.042	39.40	3.19	2.55
61CD1	0.304	0.015	32.70	1.91	3.37
61CG2	0.752	0.083	80.20	12.60	0.78
62CD1	0.45	0.051	85.70	10.60	0.21
62CD2	0.351	0.017	55.00	2.78	1.09
68CG2					
72CG1					
72CG2	0.695	0.123	85.30	19.00	0.32
73CG2	0.827	0.077	65.90	8.77	0.42
75CG1	0.922	0.045	63.70	4.21	0.68
75CG2	0.868	0.04	10.70	2.01	0.09
78CG1	0.887	0.032	30.50	1.85	1.33
78CG2	0.813	0.031	24.90	1.78	0.77
81CB					
82CD1	0.614	0.018	25.60	1.30	1.84
82CG2	0.815	0.026	31.50	1.59	0.41
83CB					
84CB					
88CG1	0.786	0.031	23.10	2.01	0.28
88CG2					
91CD1	0.735	0.014	8.63	1.36	1.37
91CG2	0.822	0.037	31.20	2.75	0.47
92CE	0.153	0.006	14.60	0.36	1.13
93CG1	0.885	0.055	44.40	4.83	0.27
93CG2	0.887	0.049	19.80	2.81	0.56
94CD1					
94CG2					
99CG1	0.808	0.07	86.70	11.70	0.04
99CG2	0.862	0.06	49.90	4.71	0.48
104CD1	0.618	0.037	42.30	3.61	0.02
104CD2					
107CB	0.756	0.07	80.20	10.30	1.68
110CD1	0.815	0.232	67.70	21.00	1.12
110CD2	0.658	0.115	34.20	10.10	0.65
112CD1	0.284	1.775	220.00	542.00	0.91
112CD2	0.956	0.114	15.20	5.68	0.84
113CG2					

Methyl	S^2_{axis}	S^2_{axis} err	τ_e	τ_e err	χ^2
115CD1	0.785	0.091	16.70	5.38	0.13
115CG2	0.892	0.062	40.90	4.43	2.68
117CB	1.056	0.472	83.70	298.00	1.26
119CG1	0.418	0.019	54.00	2.53	0.18
119CG2					
123CG2	0.818	0.059	25.80	3.27	0.44
136CG1					
136CG2					
143CB	0.883	0.039	40.00	2.43	0.51
145CB	0.862	0.023	44.60	1.44	0.98
155CD1	0.805	0.036	13.10	1.50	1.40
155CG2	0.84	0.048	33.00	3.24	0.36
156CD1	0.357	0.018	32.10	1.90	0.39
156CD2	0.352	0.017	34.80	1.89	1.45

Chapter 3

3.1. Compound 1 characterization data.

One dimensional ^{1}H and ^{13}C NMR data along with mass spectrometry confirmed the identity

of **1**. ^{1}H NMR (300 MHz, DMSO-d_6): δ 7.71 (bs, NH$_2$), 7.52-7.47 (m, 1H), 7.38-7.33 (m,

3H), 7.26-7.24 (m, 1H), 7.10-7.06 (m, 2H), and 6.27 (bs, NH$_2$); ^{13}C NMR (75 MHz, DMSO-

d_6): δ 161.7, 160.1, 155.5, 135.7, 132.2, 131.4, 131.2, 129.4, 128.9, 127.8, 126.8, and 110.7;

MS (m/z): [M]$^+$ calcd. for $C_{14}H_{11}ClN_4S$, 302.04, found, 303.0.

3.2. X-ray crystallography data collection and refinement statistics for E:NADPH:1.[*]

	3KFY
Data Collection	
Space Group	$P2_12_12_1$
Cell Dimensions	
a, b, c (Å)	34.2, 44.9, 98.0
α, β, γ (°)	90.0, 90.0, 90.0
Resolution (Å)	2.08
R_{merge}(%)	0.026 (0.042)

I/σI	22.5 (3.8)
Completeness (%)	93.7 (89.4)
Redundancy	3.3 (2.8)
Refinement	
Resolution Range (Å)	23.63-2.08
No. reflections	8993 (449)
R_{work} / R_{free}	0.1892/0.2442
No. atoms	
Protein	1295
Ligand/ion	54
Water	136
B-factors	
Protein	18.98
Ligand/ion	38.29
Water	26.31
R.m.s. deviations	
Bond lengths (Å)	0.010
Bond angles (°)	1.10
Ramanchandran	
Residues in most favored regions	156
Residues in additional allowed regions	1
Residues in generously allowed regions	0
Residues in disallowed regions	0

* Dataset was collected from a single crystal.

3.3. Met20 loop residue intensity analysis

Residue	*Description*
9	broadened
10	broadened
11	broadened; not analyzed due to spectral overlap
12	not broadened
13	not broadened
14	broadened
15	broadened; split into two resonances
16	broadened
17	broadened
18	broadened
19	broadened
20	broadened
21	proline; no $^1H^N$ resonance for analysis
22	unassigned, likely due to broadening
23	broadened; not analyzed due to spectral overlap
24	broadened

3.4. The hydrogen-hydrogen distance pattern between receptor and compound 1 in its lowest-energy bound conformation (pose A) calculated from Induced Fit Docking.

Receptor residue number	Receptor atom name[a]	Distance to the benzopyrimidine[b] (Å)			Distance to the phenyl ring[b] (Å)			
		H12	H8	H9	H23	H24	H26	H27
A7[c]	HB		4.4					
M20	HE		4.7	5.6				
	HG	5.0	4.2	3.8				
	HB	4.6	5.9					
D27	HB		4.1					
	HA		5.6					
L28[d]	HD1		5.5	5.5				
	HA				5.7			
	HB		5.5	5.8				
	HD2	5.0	3.3		4.8			
	HG		4.0					
W30	HE							
F31	HB				5.2			
	HD				3.9			
	HE				3.3	5.8	6.0	
	HZ					3.8	5.1	
K32	HG					5.9		
	HE					5.7		
T35	HG2							
M42	HE						4.4	5.8
T46	HG1							5.7
	HG2[e]						2.8	2.2
W47	HA						4.3	
	HE3						5.2	
S49	HG						4.6	
I50	HG2					5.2	3.8	4.9
	HD1						4.1	
	HG1						5.8	
L54	HD1							*6.9*
	HD2				5.0	5.1	4.5	5.8
	HG					5.4		
R57	HH1					5.7		
I94	HG2							6.0
	HD1						3.1	5.0
	HB[e]				5.0		5.1	
	HG1						3.9	

[a]Assignments were completed only for $^1H^\alpha$, $^1H^\beta$, and terminal $^1H^{Me}$ resonances. Additional side-chain and aromatic ^1H resonances were not assigned. For M20, $^1H^\beta$ assignment was not possible as the HBHA(CO)NH experiment read-out is on residue i+1 (P21 lacks backbone $^1H^N$).

[b]Only the distances less than 6 Å are shown, except for L54.HD1 (marked in red) that has NOEs to protons on **1**. In the case of methylene and methyl groups, only the closest H-H distance to **1** is reported. Atom numbering scheme for **1** taken from crystal structure 3KFY.

[c]Gray shading indicates the specific residue/H atoms that have medium to strong NOEs to protons on the benzopyrimidine moiety of **1**, as shown in Table 1.

[d]Green shading indicates the specific residue/H atoms that have NOEs to protons on the mobile phenyl ring of **1**, as shown in Table 1.

[e]Unable to assign the resonance, likely due to broadening from slow timescale exchange.

3.5. ^{15}N Relaxation dispersion fitted parameters for E:NADPH:1.

Residue	k_{ex} (s^{-1})			p_B (%)			$\Delta\omega$ (ppm)			χ^2
6	843.59	±	59.28	2.6	±	0.1	-3.431	±	0.319	17.9
7[a]	843.59	±	59.28	2.6	±	0.1	-2.605	±	0.240	6.07
8	843.59	±	59.28	2.6	±	0.1	-3.220	±	0.219	15.6
9	843.59	±	59.28	2.6	±	0.1	3.287	±	1.108	18.1
10	843.59	±	59.28	2.6	±	0.1	-0.849	±	0.139	5.97
12[a]	843.59	±	59.28	2.6	±	0.1	0.986	±	0.129	27.3
14	843.59	±	59.28	2.6	±	0.1	2.310	±	0.289	9.38
16	843.59	±	59.28	2.6	±	0.1	-2.301[b]	±	0.210	16.6
18	843.59	±	59.28	2.6	±	0.1	0.984	±	0.213	9.74
19	843.59	±	59.28	2.6	±	0.1	2.410[b]	±	0.203	22.4
20	843.59	±	59.28	2.6	±	0.1	2.686	±	0.212	24.0
24[a]	843.59	±	59.28	2.6	±	0.1	-2.911	±	0.553	7.90
27	843.59	±	59.28	2.6	±	0.1	-1.574	±	0.157	12.2
29	843.59	±	59.28	2.6	±	0.8	-1.091	±	0.167	13.5
30	843.59	±	59.28	2.6	±	0.8	0.913	±	0.271	4.79
31	843.59	±	59.28	2.6	±	0.8	1.357	±	0.164	13.3
33	843.59	±	59.28	2.6	±	0.8	-1.187	±	0.132	10.2
34	843.59	±	59.28	2.6	±	0.8	-1.219	±	0.165	12.1
35	843.59	±	59.28	2.6	±	0.8	-0.595	±	0.243	41.6
36	843.59	±	59.28	2.6	±	0.8	-2.514	±	0.282	13.4
37[c]	843.59	±	59.28	2.6	±	0.8	-1.890	±	0.147	9.58
40[c]	843.59	±	59.28	2.6	±	0.8	3.574	±	0.336	7.54
41	843.59	±	59.28	2.6	±	0.8	-1.556[b]	±	0.270	13.0
45[a]	843.59	±	59.28	2.6	±	0.8	1.346	±	0.083	23.3
48	843.59	±	59.28	2.6	±	0.1	1.349	±	0.100	9.64
50[c]	843.59	±	59.28	2.6	±	0.8	0.720	±	0.235	14.3
51	843.59	±	59.28	2.6	±	0.8	0.901	±	0.135	40.3
52[c]	843.59	±	59.28	2.6	±	0.8	-0.824	±	0.151	15.5
54	843.59	±	59.28	2.6	±	0.8	-0.960[b]	±	0.181	18.8
57[c]	843.59	±	59.28	2.6	±	0.8	1.700	±	0.081	50.1

Residue	k_{ex} (s^{-1})			p_B (%)			$\Delta\omega$ (ppm)			χ^2
60	843.59	±	59.28	2.6	±	0.8	-1.042	±	0.093	14.7
94	843.59	±	59.28	2.6	±	0.1	2.230[b]	±	0.311	9.57
96	843.59	±	59.28	2.6	±	0.1	-1.937	±	0.110	50.2
97	843.59	±	59.28	2.6	±	0.1	3.457	±	0.247	50.2
98	843.59	±	59.28	2.6	±	0.1	-1.983	±	0.152	4.60
101	843.59	±	59.28	2.6	±	0.1	-1.314	±	0.112	12.9
103	843.59	±	59.28	2.6	±	0.1	1.002	±	0.102	13.0
104	843.59	±	59.28	2.6	±	0.1	0.818	±	0.094	15.3
111	843.59	±	59.28	2.6	±	0.8	1.194	±	0.135	10.6
112	843.59	±	59.28	2.6	±	0.8	-1.307[b]	±	0.197	18.9
113	843.59	±	59.28	2.6	±	0.7	0.957	±	0.114	5.76
114	843.59	±	59.28	2.6	±	0.7	-0.882[b]	±	0.220	30.4
115[a]	843.59	±	59.28	2.6	±	0.1	0.977[b]	±	0.333	11.5
116[a]	843.59	±	59.28	2.6	±	0.1	-1.174	±	0.091	41.7
118[a]	843.59	±	59.28	2.6	±	0.1	-0.790[b]	±	0.074	24.5
120[a]	843.59	±	59.28	2.6	±	0.1	1.968[b]	±	0.199	15.4
121[a]	843.59	±	59.28	2.6	±	0.1	3.726	±	0.253	54.3
122[a]	843.59	±	59.28	2.6	±	0.1	1.101	±	0.144	14.2
123[a]	843.59	±	59.28	2.6	±	0.1	1.449	±	0.145	13.2
147	843.59	±	59.28	2.6	±	0.1	-0.746	±	0.114	15.4
148	843.59	±	59.28	2.6	±	0.1	-0.752	±	0.102	11.1
149[a]	843.59	±	59.28	2.6	±	0.1	2.402	±	0.121	8.14
150[a]	843.59	±	59.28	2.6	±	0.1	-0.853[b]	±	0.088	20.7
153	843.59	±	59.28	2.6	±	0.7	-0.981[b]	±	0.344	63.3
154	843.59	±	59.28	2.6	±	0.7	0.959[b]	±	0.288	17.5

[a] Marker of Met20 loop closed-to-occluded conformational switching motion.
[b] Residues for which $\chi^2_{global}/\chi^2_{local} > 2$ (local fitted $\Delta\omega$ reported).
[c] Residues sensitive to loss of thiophenyl from preferred binding pose A.

Chapter 4

4.1. Compound characterization data for 2-6.

(A) E:NADPH:**2**

^{1}H NMR (500 MHz, DMSO-d_6): δ 5.94 (bs, NH$_2$), 5.46 (bs, NH$_2$), 2.46-2.41 (m, 1H), 2.23-2.13 (m, 2H), 1.83-1.70 (m, 2H), 1.62-1.56 (m, 1H), 1.45-1.39 (m, 1H), 1.16-1.15 (d, 3H);

^{13}C NMR (125 MHz, DMSO-d_6): δ 165.5, 162.7, 160.9, 100.4, 34.2, 30.4, 22.4, 20.1, 19.5;

MS (*m/z*): [M]$^+$ calcd. for C$_9$H$_{14}$N$_4$, 178.12, found, 179.0.

(B) E:NADPH:**3**

^{1}H NMR (300 MHz, DMSO-d_6): δ 5.97 (bs, NH$_2$), 5.51 (bs, NH$_2$), 2.42-2.34 (m, 3H), 1.77-1.73 (m, 3H), 1.29 (m, 1H), and 1.03-1.01 (d, 3H); ^{13}C NMR (75 MHz, DMSO-d_6): δ 162.6, 161.7, 160.9, 100.4, 31.1, 30.4, 28.7, and 21.8; MS (*m/z*): [M]$^+$ calcd. for C$_9$H$_{14}$N$_4$, 178.12, found, 179.0.

(C) E:NADPH:**4**

^{1}H NMR (500 MHz, DMSO-d_6): δ 6.04 (bs, NH$_2$), 5.55 (bs, NH$_2$), 2.42-2.38 (m, 1H), 2.32-2.27 (m, 1H), 2.18-2.12 (m, 1H), 2.04-1.98 (m, 1H), 1.82-1.72 (m, 2H), 1.28-1.20 (m, 1H), 0.98-0.96 (d, 3H); ^{13}C NMR (125 MHz, DMSO-d_6): δ 162.6, 161.1, 160.6, 100.6, 30.5, 28.2, 22.5, 21.6, 21.5; MS (*m/z*): [M]$^+$ calcd. for C$_9$H$_{14}$N$_4$, 178.12, found, 179.2.

(D) E:NADPH:**5**

^{1}H NMR (500 MHz, DMSO-d_6): δ 5.93 (bs, NH$_2$), 5.45 (bs, NH$_2$), 2.35-2.33 (m, 2H), 2.19-2.17 (m, 2H), and 1.66-1.65 (m, 4H); ^{13}C NMR (125 MHz, DMSO-d_6): δ 162.6, 161.9, 160.8, 100.9, 31.3, 22.5, 22.3, 21.9; MS (*m/z*): [M]$^+$ calcd. for C$_8$H$_{12}$N$_4$, 164.11, found, 165.0.

(E) E:NADPH:**6**

^{1}H NMR (500 MHz, DMSO-d_6): δ 6.00 (bs, NH$_2$), 5.49 (bs, NH$_2$), 2.72-2.69 (m, 1H), 2.35-2.33 (m, 2H), 1.78-1.57 (m, 4H), 1.03-1.02 (d, 3H); ^{13}C NMR (125 MHz, DMSO-d_6): δ

162.3, 161.1, 160.5, 106.1, 31.2, 29.9, 24.9, 19.5, 17.3; MS (m/z): $[M]^+$ calcd. for $C_9H_{14}N_4$, 178.12, found, 179.3.

4.2. Data collection and refinement statistics for E:NADPH:3[*]

	3R33
Data Collection	
Space Group	$P2_12_12_1$
Cell Dimensions	
a, b, c (Å)	34.1, 45.1, 97.7
α, β, γ (°)	90.0, 90.0, 90.0
Resolution	2.09 Å
R_{merge}(%)	0.033 (0.044)
I/σI	27.9 (17.0)
Completeness (%)	98.3 (98.9)
Redundancy	4.8 (3.7)
Refinement	
Resolution Range (Å)	15.32-2.09
No. reflections	9261 (2470)
R_{work} / R_{free}	.1812/.2447
No. atoms	
Protein	1343
Ligand/ion	81
Water	177
B-factors	
Protein	9.61
Ligand/ion	17.31
Water	17.33
R.m.s. deviations	
Bond lengths (Å)	0.009
Bond angles (°)	1.15
Ramanchandran	
Residues in most favored regions	156
Residues in additional allowed regions	1
Residues in generously allowed regions	0
Residues in disallowed regions	0

* Dataset was collected from a single crystal.

4.3. Data collection and refinement statistics for E:NADPH:4[*]

	3QYL
Data Collection	
Space Group	$P2_12_12_1$
Cell Dimensions	
a, *b*, c (Å)	33.9, 44.8, 97.8
α, β, γ (°)	90.0, 90.0, 90.0
Resolution	1.79 Å
R_{merge}(%)	0.123 (0.260)
I/σI	15.5 (2.6)
Completeness (%)	98.3 (89.3)
Redundancy	9.2 (2.50)
Refinement	
Resolution Range (Å)	27.02-1.79
No. reflections	14401 (728)
R_{work} / R_{free}	.1749/.2088
No. atoms	
Protein	1314
Ligand/ion	77
Water	198
B-factors	
Protein	17.13
Ligand/ion	16.36
Water	26.89
R.m.s. deviations	
Bond lengths (Å)	0.010
Bond angles (°)	1.14
Ramanchandran	
Residues in most favored region	156
Residues in additional allowed regions	1
Residues in generously allowed regions	0
Residues in disallowed regions	0

* Dataset was collected from a single crystal.

4.4. Data collection and refinement statistics for E:NADPH:5[*]

	3QYO
Data Collection	
Space Group	$P2_12_12_1$
Cell Dimensions	
a, *b*, c (Å)	34.0, 45.1, 97.8
α, β, γ (°)	90.0, 90.0, 90.0

Resolution		2.09 Å
R_{merge}(%)		0.050 (0.056)
I/σI		26.6 (13.2)
Completeness (%)		99.6 (99.1)
Redundancy		5.0 (3.9)
Refinement		
Resolution Range (Å)		15.33-2.09
No. reflections		9409 (1303)
R_{work} / R_{free}		.1651/.2359
No. atoms		
	Protein	1315
	Ligand/ion	68
	Water	203
B-factors		
	Protein	9.57
	Ligand/ion	11.21
	Water	18.72
R.m.s. deviations		
	Bond lengths (Å)	0.010
	Bond angles (°)	1.13
Ramanchandran		
	Residues in most favored regions	156
	Residues in additional allowed regions	1
	Residues in generously allowed regions	0
	Residues in disallowed regions	0

* Dataset was collected from a single crystal.

4.5. ^{15}N Relaxation dispersion fitted parameters for E:NADPH:2.

Residue	k_{ex} (s^{-1})			p_B (%)			$\pm \Delta\omega$	$|\Delta\omega|$ (ppm)			χ^2
8	1658.5	±	167.7	4.1	±	1.0	n.d.*	1.787	±	0.217	17.5
9	1658.5	±	167.7	4.1	±	1.0	n.d.	2.406	±	0.384	12.8
10	1658.5	±	167.7	4.1	±	1.0	n.d.	0.782	±	0.118	15.6
11	1658.5	±	167.7	4.1	±	1.0	n.d.	2.734	±	0.488	8.80
14	1658.5	±	167.7	4.1	±	1.0	n.d.	1.353	±	0.167	6.93
22^a	1658.5	±	167.7	4.1	±	1.0	n.d.	1.983	±	0.334	6.50
36	1658.5	±	167.7	4.1	±	1.0	n.d.	0.554	±	0.180	23.3
40	4782.4	±	845.4	4.7	±	1.7	n.d.	1.657	±	0.558	32.2
44	4782.4	±	845.4	4.7	±	1.7	n.d.	1.761	±	0.428	51.0
48	4782.4	±	845.4	4.7	±	1.7	n.d.	1.849	±	0.412	39.5
50	4782.4	±	845.4	4.7	±	1.7	n.d.	1.932	±	0.586	26.9
54	4782.4	±	845.4	4.7	±	1.7	n.d.	1.735	±	0.579	32.6
57	4782.4	±	845.4	4.7	±	1.7	n.d.	1.815	±	0.418	60.6
98	4782.4	±	845.4	4.7	±	1.7	n.d.	1.261	±	0.284	21.5

Residue	k_{ex} (s^{-1})			p_B (%)			$\pm \Delta\omega$	$|\Delta\omega|$ (ppm)			χ^2
111	1658.5	±	167.7	4.1	±	1.0	n.d.	0.835	±	0.106	9.17
113	1658.5	±	167.7	4.1	±	1.0	n.d.	0.782	±	0.089	13.3
115[a,b]	2765.4	±	1125.1	2.0	±	0.9	n.d.	1.519	±	0.445	5.06
119[a,b]	4137.4	±	951.1	14.6	±	4.9	n.d.	1.106	±	0.223	10.2

[*]n.d. – Sign was not determined for these residues.
[a]Marker of Met20 loop switching, based on closed-to-occluded ^{15}N CSP (97).
[b]Local fit reported.

4.6. ^{15}N Relaxation dispersion fitted parameters for E:NADPH:3.

Residue	k_{ex} (s^{-1})			p_B (%)			$\pm \Delta\omega$	$|\Delta\omega|$ (ppm)			χ^2
8	1041.4	±	292.3	2	±	0.5	+	1.910	±	0.500	7.94
9	1041.4	±	292.3	2	±	0.5	-	2.787	±	0.899	14.2
11	1041.4	±	292.3	2	±	0.5	-	4.529	±	2.006	12.6
22[a,b]	2905.3	±	965.4	3.7	±	2.4	-	1.028	±	0.388	18.8
31	1041.4	±	292.3	2	±	0.5	+	1.305	±	0.434	11.9
111	1041.4	±	292.3	2	±	0.5	+	1.276	±	0.345	7.34
112	1041.4	±	292.3	2	±	0.5	-	1.339	±	0.307	10.1
119[b]	1041.4	±	292.3	2	±	0.5	-	0.686	±	0.416	4.93

[a]Marker of Met20 loop switching, based on closed-to-occluded ^{15}N CSP (97).
[b]Local fit reported.

4.7. ^{15}N Relaxation dispersion fitted parameters for E:NADPH:4.

Residue	k_{ex} (s^{-1})			p_B (%)			$\pm \Delta\omega$	$|\Delta\omega|$ (ppm)			χ^2
8	1841.2	±	189.3	3.7	±	2.2	n.d.[*]	1.631	±	.0393	23.7
9	1841.2	±	189.3	3.7	±	2.2	n.d.	2.353	±	0.633	14.9
11	1841.2	±	189.3	3.7	±	2.2	n.d.	2.794	±	0.782	16.0
14	1841.2	±	189.3	3.7	±	2.2	n.d.	1.114	±	0.263	15.6
22[a]	1841.2	±	189.3	3.7	±	2.2	n.d.	2.192	±	0.582	10.8
29	1841.2	±	189.3	3.7	±	2.2	n.d.	1.112	±	0.272	12.4
31	1841.2	±	189.3	3.7	±	2.2	n.d.	1.000	±	0.249	8.91
37	4885.3	±	848.2	4.7	±	1.4	n.d.	1.208	±	0.240	12.1
50	4885.3	±	848.2	4.7	±	1.4	n.d.	1.671	±	0.296	20.6
54	4885.3	±	848.2	4.7	±	1.4	n.d.	1.118	±	0.213	57.8
58	4885.3	±	848.2	4.7	±	1.4	n.d.	1.927	±	0.265	48.3
111	1841.2	±	189.3	3.7	±	2.2	n.d.	1.073	±	0.254	26.3
112	1841.2	±	189.3	3.7	±	2.2	n.d.	1.165	±	0.266	21.4
113	1841.2	±	189.3	3.7	±	2.2	n.d.	1.100	±	0.277	21.0

[*]n.d. – Sign was not determined for these residues.
[a]Marker of Met20 loop switching, based on closed-to-occluded ^{15}N CSP (97).

4.8. ^{15}N Relaxation dispersion fitted parameters for E:NADPH:5.

Residue	k_{ex} (s^{-1})			p_B (%)			$\pm \Delta\omega$	$|\Delta\omega|$ (ppm)			χ^2
8	1497.4	±	384.9	2.1	±	0.9	-	1.697	±	0.350	9.48
9	1497.4	±	384.9	2.1	±	0.9	-	3.208	±	1.254	5.10
10	1497.4	±	384.9	2.1	±	0.9	-	1.031	±	0.251	11.7
11	1497.4	±	384.9	2.1	±	0.9	-	3.738	±	1.467	6.86
22[a]	1497.4	±	384.9	2.1	±	0.9	-	2.303	±	0.650	8.54
29	1497.4	±	384.9	2.1	±	0.9	-	1.645	±	0.606	13.2
31	1497.4	±	384.9	2.1	±	0.9	+	1.180	±	0.351	8.81
36	1497.4	±	384.9	2.1	±	0.9	-	0.868	±	0.446	6.39
40	1497.4	±	384.9	2.1	±	0.9	-	1.625	±	0.421	17.6
48	1497.4	±	384.9	2.1	±	0.9	n.d.[*]	1.221	±	0.282	11.9
50	1497.4	±	384.9	2.1	±	0.9	+	1.532	±	0.507	21.8
54	1497.4	±	384.9	2.1	±	0.9	-	1.277	±	0.618	17.3
58	1497.4	±	384.9	2.1	±	0.9	-	1.110	±	0.331	21.3
96	1497.4	±	384.9	2.1	±	0.9	+	1.426	±	0.350	32.4
111	1497.4	±	384.9	2.1	±	0.9	+	1.612	±	0.402	12.1
112	1497.4	±	384.9	2.1	±	0.9	-	1.444	±	0.292	11.9
113	1497.4	±	384.9	2.1	±	0.9	n.d.	1.205	±	0.355	7.98

[*]n.d. – Sign was not determined for these residues, likely due to spectral overlap.
[a]Marker of Met20 loop switching, based on closed-to-occluded ^{15}N CSP (97).

4.9. ^{15}N Relaxation dispersion fitted parameters for E:NADPH:6.

Residue	k_{ex} (s^{-1})			p_B (%)			$\pm \Delta\omega$	$|\Delta\omega|$ (ppm)			χ^2
7	1514.9	±	206.0	2.3	±	1.1	-	1.885	±	0.382	42.8
8	1514.9	±	206.0	2.3	±	1.1	-	2.356	±	0.514	14.5
10	1514.9	±	206.0	2.3	±	1.1	-	1.017	±	0.443	16.8
11	1514.9	±	206.0	2.3	±	1.1	-	4.676	±	1.724	10.2
12	1514.9	±	206.0	2.3	±	1.1	+	1.303	±	0.274	24.8
19	1514.9	±	206.0	2.3	±	1.1	-	0.814	±	0.406	23.0
30	1514.9	±	206.0	2.3	±	1.1	+	0.961	±	0.562	12.5
36	1514.9	±	206.0	2.3	±	1.1	+	1.516	±	0.344	14.2
37	1514.9	±	206.0	2.3	±	1.1	+	1.218	±	0.340	15.0
40	1514.9	±	206.0	2.3	±	1.1	-	1.922	±	0.428	18.7
45	1514.9	±	206.0	2.3	±	1.1	-	1.480	±	0.320	29.0
49	1514.9	±	206.0	2.3	±	1.1	+	0.927	±	0.236	22.2
54	1514.9	±	206.0	2.3	±	1.1	-	1.150	±	0.313	26.2
57	1514.9	±	206.0	2.3	±	1.1	-	1.447	±	0.308	18.0
59	1514.9	±	206.0	2.3	±	1.1	+	1.070	±	0.360	11.9
98	1514.9	±	206.0	2.3	±	1.1	-	1.776	±	0.453	16.1
104	1514.9	±	206.0	2.3	±	1.1	n.d.[*]	0.559	±	0.517	8.29

Residue	k_{ex} (s^{-1})			p_B (%)			$\pm \Delta\omega$	$|\Delta\omega|$ (ppm)			χ^2
111	1514.9	±	206.0	2.3	±	1.1	+	1.574	±	0.347	26.1
112	1514.9	±	206.0	2.3	±	1.1	+	1.923	±	0.408	28.0
115[a]	1514.9	±	206.0	2.3	±	1.1	+	1.474	±	0.361	12.4
116[a]	1514.9	±	206.0	2.3	±	1.1	+	1.198	±	0.256	24.6
118[a]	1514.9	±	206.0	2.3	±	1.1	-	1.645	±	0.329	23.8
120[a]	1514.9	±	206.0	2.3	±	1.1	+	2.383	±	0.536	19.4
142	1514.9	±	206.0	2.3	±	1.1	+	1.710	±	0.374	22.2
149[a]	1514.9	±	206.0	2.3	±	1.1	-	2.218	±	0.568	11.5

[*]n.d. – Sign was not determined for this residue, likely due to spectra overlap.
[a]Marker of Met20 loop switching, based on closed-to-occluded ^{15}N CSP (97).

4.10. Relaxation dispersion global fitted parameters of the ligand-independent C-terminal residues for all complexes.

Compound	k_{ex} (s^{-1})	p_A (%)	$k_{conf,forward}$ (s^{-1})
2	585.0 ± 132.2	97.5 ± 0.2	14.6 ± 3.3
3	509.8 ± 51.3	97.4 ± 0.2	13.3 ± 1.4
4	647.4 ± 58.4	97.5 ± 0.1	16.2 ± 1.5
5	542.9 ± 113.8	97.3 ± 0.3	14.7 ± 3.1
6	389.6 ± 47.3	96.6 ± 0.3	13.2 ± 1.7

4.11. Visually broadened residues in each THQ ternary complex.

(A) E:NADPH:**2**

broadened	severely broadened
4, 6, 29, 30, 32, 35, 37, 46, 59, 64, 68, 94, 122, 123	7, 15, 17, 18, 23, 70, 97, 124

(B) E:NADPH:**3**

broadened	severely broadened
10, 15, 17, 18, 27, 29, 30, 34, 35, 36, 40, 41, 46, 50, 58, 68, 92, 94, 95, 108, 122, 123,	6, 7, 14, 23, 37, 59, 70, 87, 124

(C) E:NADPH:**4**

broadened	severely broadened
6, 7, 10, 15, 18, 27, 32, 33,	23, 30, 70, 124

34, 35, 36, 46, 47, 59, 68, 69, 94, 97, 99, 123	

(D) E:NADPH:**5**

broadened	severely broadened
6, 7, 14, 15, 18, 30, 35, 46, 47, 97, 103, 109, 123	59, 68, 69, 70, 124

(E) E:NADPH:**6**

broadened	severely broadened
34, 37, 103, 113	6, 9, 15, 18, 23, 31, 32, 46, 68, 70, 87, 94, 95, 97, 121, 122, 124, 148

Chapter 5

5.1. ^{15}N Relaxation model-free analysis of E:NADPH:1.

Residue	S^2_s	$S^2_{s\,err}$	τ_e (ps)	τ_e err	S^2_f	$S^2_{f\,err}$	R_{ex}	R_{ex} err	χ^2
2	0.8912	0.013	7.4	13					2.69
3	0.8633	0.0108	11.0	8.9					7.81
4	0.9009	0.013	4.0	7.9					1.58
5	0.8896	0.0148	2.2	6.0					4.43
6	0.8474	0.0449					2.67	1.06	1.07
7	0.8287	0.0305	3.2	8.2					1.25
8	0.829	0.0212	7.6	8.4			2.87	0.525	2.3
9	0.8258	0.0371					2.11	0.972	2.91
10	0.8451	0.0208					0.872	0.480	3.05
12	0.8771	0.0157	15.2	14.9					6.89
13	0.8954	0.0117	8.4	10.8					6.97
14	0.9539	0.0356	87.6	317					1.49
15	0.8871	0.0269	25.0	19.4			1.32	0.602	3.08
16	0.8918	0.0195					1.20	0.440	1.75
17	0.8347	0.0271					3.54	0.728	6.7
18	0.9363	0.0261	21.5	37.3					6.59
19	0.8474	0.0117	13.8	6.9			0.465	0.266	6.71
20	0.8803	0.0176	59.8	21.8					7.69
26	0.9035	0.0165	7.4	12.3					3.58

Residue	S^2_s	$S^2_{s\,err}$	τ_e (ps)	τ_e err	S^2_f	$S^2_{f\,err}$	R_{ex}	R_{ex} err	χ^2
27	0.851	0.0274					1.11	0.610	4.13
28	0.8867	0.2519	155	45.9					1.13
29	0.8674	0.0251	44.9	19.6			1.27	0.576	0.52
30	0.8901	0.019	0.2	1.4					8.42
31	0.916	0.0233					1.11	0.521	2.51
32	0.9019	0.0171					0.787	0.373	2.7
33	0.9054	0.0155	14.9	18.8					2.78
34	0.8995	0.0905	7.7E4	3.9E5					3.29
35	0.8453	0.0182					1.01	0.388	0.82
36	0.8802	0.0333					3.54	0.831	2.8
37	0.9079	0.0287	137	281					1.52
40	0.9286	0.0285	9.9	29.0					3.39
41	0.8062	0.026					1.36	0.587	2.32
42	0.9395	0.0113	8.0	1.4					3.44
43	0.8941	0.0177	0.6	2.8					7.02
44	0.8433	0.0134					1.56	0.301	6.38
47	0.8901	0.0198					1.16	0.425	1.19
48	0.8846	0.0195					0.798	0.421	2.84
49	0.836	0.0117					0.698	0.255	3
50	0.8659	0.0184	1.1	4.4					6.04
51	0.8596	0.0147	14.1	12.7					5.59
52	0.8713	0.0134	14.7	13.2					2.17
54	0.8897	0.0179	3.8	8.7					3.54
57	0.8972	0.0112	6.8	9.7					9.91
58	0.8848	0.0251	19.5	26.3					3.54
60	0.8479	0.0132	5.0	7.2					3.39
61	0.8724	0.0112	2.0	4.4					4.74
62	0.8739	0.0115	4.1	6.8					4.11
63	0.86	0.0079	7.8	7.2					4.65
64	0.851	0.0245					0.983	0.539	11.8
65	0.8734	0.0086	16.2	8.7					6.61
67	0.8061	0.0141	1870	175	0.6033	0.0116			15
68	0.7571	0.0977	938	196	0.6933	0.0551			2.38
69	0.7132	0.0221	753	79.6	0.6731	0.03			3.25
70	0.7697	0.0418	5.6	8.3					0.39
71	0.8694	0.0095	17.0	8.3					3.14
72	0.8754	0.007	8.4	6.9					29.4
73	0.8595	0.0143	4.1	6.8					3.3
74	0.8149	0.0076	2.0	3.1					3.21
75	0.8648	0.0117	3.3	5.0			0.502	0.272	3.96
76	0.8358	0.0099	13.4	9.0					4.03
77	0.8705	0.006	14.6	7.3					28.7
78	0.9177	0.011	22.4	16.2					1.74
79	0.8939	0.0072	5.7	6.9					13.3
80	0.9035	0.0084	36.7	14.0					4.81

Residue	S^2_s	$S^2_{s\,err}$	τ_e (ps)	τ_e err	S^2_f	$S^2_{f\,err}$	R_{ex}	R_{ex} err	χ^2
81	0.8984	0.0056	14.2	8.4					7.25
82	0.876	0.0096	20.2	12.6					5.02
83	0.9218	0.0067	4.5	7.5					4.94
84	0.9011	0.0059	8.4	8.1					9.98
86	0.8556	0.0077	3.2	4.7					3.55
88	0.6588	0.0058	1140	98.8	0.8596	0.0077			4.52
90	0.8786	0.0089	6.4	8.3					1.99
91	0.8489	0.0135	7.0	8.9					8.77
92	0.8852	0.013	13.1	13.7					7.69
93	0.8398	0.0117	1.9	3.9					2.17
94	0.9147	0.0228	4.00E-3	4.9E-2					10.8
95	0.9017	0.0306	44.9	30.9			2.44	0.746	1.21
96	0.8834	0.0312					2.87	0.717	9.08
97	0.8752	0.0417					2.88	0.942	15.3
98	0.9118	0.0185	52.7	34.6					1.97
99	0.8731	0.0143	3.1	5.7			0.683	0.318	4.5
101	0.8894	0.0142	32.0	15.4			0.331	0.289	2.9
103	0.8593	0.0099	3.5	5.9					4.41
106	0.8525	0.0516	2.1E5	2.3E5					1.89
107	0.8627	0.0063	22.8	8.1					8.65
108	0.8453	0.0151	5.3	7.9					1.18
111	0.8143	0.0259					1.38	0.587	2.4
112	0.8564	0.0197					1.16	0.454	1.28
113	0.8199	0.0194	4.1	6.6					2.12
114	0.8419	0.0132	1.0	2.9					6.11
115	0.8733	0.0182	5.5	9.5					1.12
116	0.9001	0.0158	11.0	15.6					2.96
117	0.7993	0.0082	2.5	3.7					2.07
120	0.816	0.0121	2.2E4	8.4E4	0.0283	7.5431			0.26
121	0.7459	0.0179	38.5	7.1			1.63	0.388	3.83
122	0.8891	0.0228	31.5	120					3.49
123	0.8517	0.0166	5.0	7.7					2.82
124	0.8719	0.115	49.2	219					4.47
125	0.884	0.0138	4.0	6.9					3.04
127	0.7939	0.0069	5.6	4.4					4.23
128	0.7517	0.0108	21.0	4.3			1.63	0.233	19.9
129	0.8553	0.0192	2.3E5	7.7E5	0.644	0.5848			0.95
131	0.8803	0.0639	676	279	0.9141	0.0474			5.79
132	0.8382	0.008	21.0	7.2					5.81
134	0.7952	0.013	18.2	6.2			0.665	0.307	3.23
136	0.8723	0.0132	2.6	5.5					1.46
137	0.85	0.0068	18.0	7.4					16.6
138	0.8927	0.0312	9.1E4	1.9E5					1.27
139	0.8185	0.0098	11.5	6.7					6
140	0.8567	0.0128	9.7E5	4.6E6					1.9

Residue	S^2_s	$S^2_{s\,err}$	τ_e (ps)	τ_e err	S^2_f	S^2_{ferr}	R_{ex}	R_{ex} err	χ^2
141	0.8253	0.0155					0.576	0.319	4.8
142	0.849	0.0094	5230	2060	0.9076	0.1532			14.7
143	0.8472	0.0129	1100	398	0.9497	0.0115			0.45
144	0.8674	0.0091	4.4	5.9					4.85
146	0.8447	0.0365	2.3E5	4.9E5					1.56
147	0.8371	0.0109	2.5	4.3					1.9
149	0.8523	0.0167					2.51	0.414	5.28
150	0.8415	0.009	20.2	8.5					1.48
151	0.9148	0.0089	7.6	10.1					0.76
152	0.8501	0.0114	2.6	4.7					1.11
153	0.8585	0.0125	1.7	4.0					1.89
154	0.8583	0.0129	0.5	2.2					6.82
155	0.8713	0.009	0.6	2.2					4.14
156	0.8573	0.0128	8.1	8.4					2.59
158	0.8701	0.0114	6.6	8.6					3.31
159	0.8416	0.0106	1740	349	0.8791	0.0109			3.37

5.2. ^{15}N Relaxation model-free analysis of E:NADPH:3.

Residue	S^2_s	$S^2_{s\,err}$	τ_e (ps)	τ_e err	S^2_f	S^2_{ferr}	R_{ex}	R_{ex} err	χ^2
1									
2	0.893	0.0127	15.9	13.3					3.6
3	0.8719	0.009	3.9	5.5					9.33
4	0.8866	0.0095	3.7	6.2					5.56
5	0.9022	0.0114	11.5	11.5					1.37
6	0.8771	0.025					1.43	0.65	1.1
7	0.8168	0.0155	5.0	7.0					0.86
8	0.8507	0.0131					1.49	0.33	1.72
9	0.8469	0.0179					2.73	0.48	1.89
10	0.8419	0.012	16.3	6.9			1.38	0.29	5.11
11	0.8888	0.0234					2.21	0.62	3.68
12	0.841	0.0123	21.5	7.1			0.67	0.29	2.5
13	0.8753	0.0078					0.57	0.20	2.1
14	0.9302	0.0207	16.7	53.8					3.55
15	0.9077	0.0114	14.7	12.6					3.92
16	0.8893	0.0098	18.0	10.4					0.23
17	0.8835	0.0184					2.14	0.48	2.84
18	0.8709	0.0203	35.4	13.6			1.23	0.51	0.84
19	0.8575	0.0051	5.0	3.9					14.1
20	0.8334	0.008	22.0	6.6					3.43
21									
22									
23									
24									

Residue	S^2_s	$S^2_{s\,err}$	τ_e (ps)	τ_e err	S^2_f	$S^2_{f\,err}$	R_{ex}	R_{ex} err	χ^2
25									
26	0.9349	0.0085	3.3	6.8					24.1
27	0.8948	0.0118	27.0	14.0					3.2
28									
29	0.9234	0.0105	4.2	8.6					4.48
30	0.8896	0.0111	2.7	5.4					1.34
31	0.9166	0.0158					0.88	0.40	4.08
32	0.905	0.0134					0.62	0.34	4.13
33	0.8848	0.007	10.8	8.3					3.31
34	0.8605	0.0092	4.7	6.1					1.47
35	0.8849	0.0093	7.8	8.4					3.05
36	0.8673	0.0116	20.4	10.3			1.10	0.31	2.17
37	0.8702	0.0137	37.0	16.7					4.48
38									
39									
40	0.8899	0.01	1.8	4.3					7
41	0.8464	0.0095	3.7	5.1					0.5
42	0.9039	0.0127	17.5	10.8			0.68	0.32	0.79
43	0.8683	0.0104	13.5	8.3					5.36
44	0.8686	0.0115					1.18	0.28	13.5
45									
46									
47	0.8932	0.0128					0.51	0.29	2.61
48	0.902	0.0127					0.92	0.30	1.71
49	0.8512	0.0074	0.6	1.8					3.79
50	0.817	0.0086	12.5	5.0			0.43	0.21	4.69
51	0.839	0.0079	23.5	7.1					1.11
52	0.8093	0.0068	24.3	3.7			0.27	0.16	1.53
53									
54	0.8471	0.0145					1.20	0.38	3.4
55									
56									
57	0.8898	0.0068	4.4	5.5					3.09
58	0.8394	0.012	22.5	9.9					2.88
59	0.817	0.0267	2.8	5.7					1.1
60	0.8553	0.0086	3.0	4.5					1.52
61	0.88	0.008	7.6	6.8					3.38
62	0.8714	0.0089	12.0	8.4					4.46
63	0.8633	0.0063	8.6	6.0					4.5
64	0.8744	0.0137	1.8	4.1					2.97
65	0.894	0.0195	8120.0	34700.0	0.9519	0.0547			6.01
66									
67	0.8131	0.0091	2040.0	134.0	0.6781	0.0093			9.59
68	0.8027	0.1096	1030.0	169.0	0.6757	0.0536			3.37
69	0.7223	0.0165	909.0	85.9	0.7519	0.0218			2.08

Residue	S^2_s	$S^2_{s\,err}$	τ_e (ps)	τ_e err	S^2_f	$S^2_{f\,err}$	R_{ex}	R_{ex} err	χ^2
70	0.7669	0.0672	21.3	22.1					0.86
71	0.8712	0.0083	2.1	3.5					8.74
72	0.8659	0.0054	9.7	5.1					16.8
73	0.8555	0.0088	0.0	0.2					7.47
74	0.8351	0.0067	6.9	4.7					3.01
75	0.8547	0.0095					0.82	0.24	1.19
76	0.8208	0.0071	24.8	5.9					2.24
77	0.8825	0.005	6.6	5.2					4.93
78	0.9183	0.0095	3.8	7.0					6.03
79	0.8979	0.0057	2.8	4.3					8.35
80	0.8998	0.0067	10.5	8.2					8.2
81	0.9019	0.005	8.3	6.8					6.26
82	0.865	0.0075	9.5	7.7					1.36
83	0.9031	0.0054	23.5	9.6					17.3
84	0.8904	0.0046	1.7	3.0					5.8
85									
86	0.8481	0.0058	8.3	4.8					10.2
87									
88	0.6416	0.004	1320.0	76.7	0.848	0.0055			9.77
89									
90	0.8556	0.0062	2.6	3.8					2.12
91	0.8243	0.0103	15.6	7.7					5.55
92	0.866	0.0113					0.70	0.29	2.43
93	0.8415	0.008	2.0	3.2					1.11
94	0.8812	0.016	0.7	2.9					2.59
95	0.9	0.0114	26.8	13.3					4.24
96	0.7998	0.0101	1710.0	281.0	0.8799	0.0112			2.49
97	0.9064	0.0131	3.3	6.7					5.16
98	0.8817	0.0106					0.68	0.26	2.08
99	0.8766	0.0098					0.75	0.23	7.72
100									
101	0.8887	0.0059	0.5	1.8					6.93
102	0.8384	0.0101	11.2	5.7			0.65	0.24	2.42
103	0.8602	0.0072	6.4	6.2					6.69
104	0.9005	0.0075	10.4	9.6					2.62
105									
106	0.8546	0.024	17400.0	76500.0	0.1648	7.9739			1.2
107	0.8597	0.0051	6.3	5.3					17.8
108	0.8765	0.0121	5.0	7.5					3.64
109	0.8768	0.0094					0.40	0.24	4.49
110									
111	0.8578	0.0129	1.5	3.7					4.23
112	0.8591	0.0152					0.69	0.37	2.88
113									
114	0.8517	0.0098	8.6	6.5					1.28

Residue	S^2_s	$S^2_{s\,err}$	τ_e (ps)	τ_e err	S^2_f	$S^2_{f\,err}$	R_{ex}	R_{ex} err	χ^2
115	0.8518	0.011	14.3	8.6					3.2
116	0.8925	0.0089	5.4	7.3					1.65
117	0.7841	0.0074	9.1	3.5			0.61	0.17	7.27
118	0.8073	0.0077	12.9	5.1					1.72
119	0.7373	0.0128	17.4	4.7			1.57	0.30	5.5
120	0.8183	0.0446	752.0	264.0	0.9194	0.0367			9.72
121	0.8231	0.0402	429.0	166.0	0.9229	0.0379			19.9
122	0.8658	0.013	9.3	9.2					2.13
123	0.8364	0.0077	0.1	0.8					5.4
124	0.8541	0.0478	6.0	25.3					2.04
125	0.838	0.0144					0.73	0.35	2.72
126									
127	0.8103	0.0325	1220.0	649.0	0.9571	0.0283			2.17
128									
129	0.8795	0.0184	28.4	16.2					2.76
130									
131	0.8307	0.0095	32.4	7.5					5.65
132	0.8768	0.0248	862.0	601.0	0.9551	0.0178			3.97
133	0.885	0.0105	28.2	7.9			0.78	0.26	4.67
134	0.8348	0.008	21.8	6.5					0.97
135									
136									
137	0.8473	0.0201	3610.0	11200.0	0.9577	0.0364			2.07
138	0.8875	0.0043	8.0	4.4					4.95
139	0.8182	0.0081	2.2	3.1					1.71
140	0.8625	0.0104	2510.0	1260.0	0.9351	0.0116			4.94
141	0.8573	0.0081	0.2	1.2					11.1
142	0.8027	0.0081	19700.0	68300.0	0.2803	5.6227			8.83
143	0.8556	0.0311	1140.0	811.0	0.9528	0.0274			3.6
144	0.8565	0.0075	7.9	5.9					2.57
145									
146	0.8282	0.0106	2160.0	1030.0	0.947	0.0091			1.63
147	0.8092	0.0069	11.9	4.3					4.98
148	0.8598	0.0291	953.0	483.0	0.9487	0.023			2.15
149	0.8334	0.0084					2.37	0.21	6.54
150	0.8404	0.0063	29.5	5.4					2
151	0.9011	0.0065	0.2	1.3					3.16
152	0.8627	0.0088	4.9	5.6					2.35
153	0.8674	0.0097	7.0	6.7					6.47
154	0.8479	0.01	9.3	6.3					1.23
155	0.8567	0.0102	9.5	7.4					1.18
156	0.869	0.0109	6.3	7.1					7.97
157									
158	0.8625	0.0098	35.0	10.0					4.54
159	0.8577	0.0083	1270.0	138.0	0.8815	0.009			6.24

5.3. ^{15}N Relaxation model-free analysis of E:NADPH:5.

Residue	S^2_f	$S^2_{f\,err}$	τ_e (ps)	τ_e err	S^2_s	$S^2_{s\,err}$	R_{ex}	R_{ex} err	χ^2
1									
2	0.8673	0.0271	13.2	19.5					1.07
3	0.8598	0.0224	16.0	18.4					0.81
4	0.8886	0.0229	22.3	26.0					0.38
5	0.8813	0.0199	2.5	6.9					0.90
6	0.9166	0.0365	46.9	189.0					0.31
7	0.8335	0.0382	64.0	37.2					0.76
8	0.8441	0.0283					1.03	0.55	0.44
9	0.8549	0.0411					1.98	0.90	2.48
10	0.8559	0.0192	9.9	12.4					2.31
11	0.8636	0.052					2.39	1.12	0.04
12	0.8079	0.0184	64.4	14.2					0.01
13	0.8733	0.0144	35.2	16.0					0.70
14	0.9295	0.0435	117.0	245.0					0.77
15	0.9061	0.0251	5.6	13.9					1.15
16	0.8623	0.0168	1.8	4.7					1.23
17	0.877	0.0398					2.34	0.87	1.14
18	0.8805	0.0309	0.3	1.9					3.32
19	0.8412	0.0112	1.1	2.8					1.01
20	0.8405	0.0166	1.7	4.3					1.48
21									
22	0.6979	0.0243					2.53	0.54	3.14
23	0.7187	0.0899	201.0	471.0					0.00
24									
25									
26	0.8904	0.0172	7.3	11.7					1.48
27									
28									
29	0.8978	0.019	43.4	30.9					0.91
30	0.858	0.0247	5.3	10.8					0.29
31	0.8996	0.0239	1.0	5.0					2.20
32	0.8729	0.0241					0.95	0.51	0.14
33	0.8784	0.0147	7.9	12.1					2.95
34	0.8441	0.0194	35.7	18.0					0.23
35	0.853	0.0225	29.7	20.7					0.19
36	0.887	0.0221					0.53	0.50	4.45
37	0.8548	0.032	71.5	43.4					0.94
38	0.7858	0.0177					0.75	0.39	0.15
39									
40	0.8947	0.0257	0.0	0.0					5.10
41	0.8463	0.0231	16.4	16.8					0.11

Residue	S^2_f	$S^2_{f\,err}$	τ_e (ps)	τ_e err	S^2_s	$S^2_{s\,err}$	R_{ex}	R_{ex} err	χ^2
42	0.9096	0.0212	15.8	23.0					0.02
43	0.9084	0.0232	27.3	92.8					0.57
44	0.8323	0.0266					1.17	0.54	1.57
45	0.8843	0.0227					0.94	0.45	9.27
46	0.7718	0.029					1.31	0.58	0.45
47	0.8956	0.018	7.2	12.7					2.20
48	0.8419	0.023					1.09	0.46	8.57
49	0.7991	0.0176					0.70	0.35	0.23
50	0.898	0.0268					0.90	0.56	0.31
51	0.8195	0.0153	25.6	12.8					0.60
52	0.8056	0.0114	24.2	9.5					0.02
53									
54	0.7925	0.0367					2.98	0.87	0.05
55									
56									
57	0.8563	0.0173	40.3	20.1					0.00
58	0.8685	0.0277	57.8	36.2					0.62
59	0.8279	0.0486	100.0	151.0					0.13
60	0.8285	0.0211	24.5	16.6					0.01
61	0.8695	0.0195	4.5	9.1					0.70
62	0.8698	0.0222	47.2	23.5					0.35
63	0.8408	0.0155	13.4	12.1					0.92
64	0.8456	0.029	6.2	10.7					0.08
65	0.8591	0.0176	42.1	15.5					0.14
66									
67	0.6814	0.0926	990.0	622.0					91.30
68	0.6878	0.0822	361.0	638.0					5.88
69	0.6521	0.0254	72.3	10.4					5.97
70	0.7214	0.1233	53.2	349.0					0.37
71	0.8802	0.0195	17.7	18.3					0.15
72	0.8507	0.0127	11.8	10.3					3.19
73	0.8341	0.0206	21.6	15.8					0.16
74	0.8148	0.0155	3.9	6.3					1.90
75	0.8638	0.0163	0.3	1.4					3.16
76	0.8425	0.0175	18.9	15.8					0.86
77	0.8892	0.011	2.4	5.4					3.23
78	0.8813	0.021	4.7	10.7					4.21
79	0.8738	0.0126	5.2	8.2					4.41
80	0.8689	0.0154	9.7	12.1					0.01
81									
82	0.8506	0.0174	3.3	7.5					0.74
83	0.8948	0.014	33.0	22.7					0.02
84	0.8722	0.0106	0.3	1.3					2.77
85	0.8426	0.0147	1.7	4.3					0.97
86	0.8356	0.0135	6.1	8.1					1.40

Residue	S^2_f	$S^2_{f\,err}$	τ_e (ps)	τ_e err	S^2_s	$S^2_{s\,err}$	R_{ex}	R_{ex} err	χ^2
87									
88	0.6035	0.0078	28.8	3.5					34.20
89									
90									
91	0.837	0.0254	4.3	9.4					0.57
92	0.8713	0.0209	6.3	12.2					0.55
93									
94	0.8945	0.0284	0.6	3.7					2.81
95	0.8831	0.0221					0.70	0.44	0.11
96	0.8311	0.0258					36.17	1.21	0.02
97	0.9557	0.0406	49.0	167.0					1.24
98	0.8729	0.017	10.9	13.9					0.36
99	0.8945	0.0166	6.3	11.1					0.56
100	0.8609	0.0169					0.58	0.33	0.69
101	0.8783	0.0144	35.0	19.8					0.63
102	0.8408	0.016	8.4	10.3					0.84
103	0.8534	0.0187	18.8	16.7					1.54
104	0.8735	0.0153	5.2	9.5					0.35
105									
106	0.8228	0.0162	33.2	13.8					0.06
107	0.8596	0.0131	25.4	15.9					3.77
108	0.8339	0.0292	49.4	29.2					0.00
109	0.8761	0.0167	29.2	19.5					0.40
110									
111	0.862	0.0302	3.9	10.6					1.16
112	0.8322	0.0302					1.08	0.62	0.22
113	0.8402	0.0319	25.4	17.2					0.00
114	0.8588	0.0223	0.0	0.0					11.90
115	0.8413	0.0252	11.5	14.7					1.02
116	0.8621	0.0192	2.4	5.9					2.93
117	0.7892	0.0146					0.38	0.28	4.46
118	0.795	0.0163	21.3	11.0					0.21
119	0.7189	0.0209					1.35	0.44	0.47
120	0.7623	0.01	34.1	6.6					2.61
121	0.7384	0.0096	42.6	5.9					0.11
122	0.8578	0.0275	2.2	6.7					1.18
123	0.8274	0.0183	0.2	0.9					3.44
124	1.0299	1.6484	6900.0	81500.0					1.62
125									
126									
127	0.7719	0.0116	20.8	7.1					1.34
128									
129	0.8009	0.037	25.9	20.6					0.11
130									
131	0.8033	0.0214	46.5	15.6					0.45

Residue	S^2_f	$S^2_{f\,err}$	τ_e (ps)	τ_e err	S^2_s	$S^2_{s\,err}$	R_{ex}	R_{ex} err	χ^2
132	0.8409	0.0156	56.5	14.6					0.13
133	0.8322	0.0262					1.31	0.55	1.19
134	0.8356	0.0176	1.6	4.2					1.30
135									
136									
137	0.822	0.0123	18.9	9.8					6.15
138									
139	0.8019	0.0188	2.6	5.0					1.35
140	0.8196	0.0213	3.5	6.4					2.12
141									
142	0.7897	0.015	27.1	8.1					6.99
143	0.8292	0.0125	3.9	5.8					3.47
144	0.8253	0.0148	2.5	4.9					0.44
145									
146	0.8102	0.0162	9.8	8.6					0.35
147	0.7944	0.0158	14.8	9.2					0.72
148	0.8441	0.0206	9.8	11.7					1.00
149	0.8331	0.0176					1.14	0.36	11.30
150	0.8203	0.015	21.6	12.4					2.46
151	0.9022	0.0155	7.2	11.3					1.39
152	0.852	0.0211	10.2	12.8					0.00
153	0.8528	0.0222	2.1	5.5					2.49
154	0.8442	0.0226	3.3	7.2					0.78
155	0.8606	0.0251	11.0	15.1					0.12
156	0.834	0.0235	34.2	16.7					0.06
157	0.8245	0.0191	41.4	14.1					0.05
158	0.8189	0.0276					1.37	0.60	4.50
159	0.8123	0.0156	22.4	12.4					15.60

5.4. ^{2}H Relaxation model-free analysis of E:NADPH:1.

Methyl	S^2_{axis}	S^2_{axis} err	τ_e	τ_e err	χ^2
1CE	0.104	0.002	16.20	0.16	44.50
2CD1	0.447	0.014	17.90	1.17	0.77
2CG2					
4CD1					
4CD2	0.521	0.081	172.00	23.80	0.52
5CD1	0.873	0.089	29.60	5.53	1.48
5CG2	0.931	0.085	36.90	5.93	0.33
6CB	0.929	0.104	60.90	9.05	1.39
7CB	0.798	0.115	54.10	10.50	0.25
8CD1	0.344	0.052	63.10	10.10	0.13
8CD2					
9CB	0.832	0.472	52.20	343.00	0.52

Methyl	S^2_{axis}	S^2_{axis} err	τ_e	τ_e err	χ^2
10CG1					
10CG2	0.64	0.115	28.60	7.95	0.48
13CG1					
13CG2	0.627	0.205	109.00	43.80	1.55
14CD1	0.798	0.053	7.71	2.94	0.01
14CG2	0.856	0.055	27.30	3.28	2.17
16CE	0.322	0.02	5.33	0.35	120.00
19CB	0.937	0.041	21.60	1.64	2.88
20CE	0.495	0.018	14.40	1.00	0.88
24CD1					
24CD2	0.298	0.052	36.00	8.82	0.65
26CB	0.914	0.101	51.50	8.41	2.24
28CD1					
28CD2	0.595	0.059	36.80	5.18	0.11
29CB					
35CG2	0.887	0.064	18.80	3.17	0.89
36CD1	0.265	0.008	58.00	1.40	1.66
36CD2	0.287	0.009	54.60	1.43	5.35
40CG1	0.914	0.058	48.50	4.95	0.07
40CG2	0.88	0.05	44.70	4.02	0.59
41CD1	0.773	0.039	20.40	2.23	0.37
41CG2	0.866	0.034	31.90	2.19	0.04
42CE	0.88	0.019	4.18	0.65	2.20
46CG2					
50CD1	0.713	0.033	17.60	1.74	0.40
50CG2	0.806	0.023	18.50	1.14	0.77
54CD1	0.649	0.04	36.20	3.29	0.96
54CD2					
60CD1	0.317	0.009	28.00	1.08	3.19
60CG2	0.853	0.042	39.40	3.19	2.55
61CD1	0.304	0.015	32.70	1.91	3.37
61CG2	0.752	0.083	80.20	12.60	0.78
62CD1	0.45	0.051	85.70	10.60	0.21
62CD2	0.351	0.017	55.00	2.78	1.09
68CG2					
72CG1	0.695	0.123	85.30	19.00	0.32
72CG2	0.827	0.077	65.90	8.77	0.42
73CG2					
75CG1	0.922	0.045	63.70	4.21	0.68
75CG2	0.868	0.04	10.70	2.01	0.09
78CG1	0.887	0.032	30.50	1.85	1.33
78CG2	0.813	0.031	24.90	1.78	0.77
81CB					
82CD1	0.614	0.018	25.60	1.30	1.84
82CG2	0.815	0.026	31.50	1.59	0.41

Methyl	S^2_{axis}	S^2_{axis} err	τ_e	τ_e err	χ^2
83CB					
84CB					
88CG1					
88CG2	0.786	0.031	23.10	2.01	0.28
91CD1	0.735	0.014	8.63	1.36	1.37
91CG2	0.822	0.037	31.20	2.75	0.47
92CE	0.153	0.006	14.60	0.36	1.13
93CG1	0.885	0.055	44.40	4.83	0.27
93CG2	0.887	0.049	19.80	2.81	0.56
94CD1					
94CG2					
99CG1	0.808	0.07	86.70	11.70	0.04
99CG2	0.862	0.06	49.90	4.71	0.48
104CD1	0.618	0.037	42.30	3.61	0.02
104CD2					
107CB	0.756	0.07	80.20	10.30	1.68
110CD1	0.815	0.232	67.70	21.00	1.12
110CD2	0.658	0.115	34.20	10.10	0.65
112CD1	0.284	1.775	220.00	542.00	0.91
112CD2	0.956	0.114	15.20	5.68	0.84
113CG2					
115CD1	0.785	0.091	16.70	5.38	0.13
115CG2	0.892	0.062	40.90	4.43	2.68
117CB	1.056	0.472	83.70	298.00	1.26
119CG1					
119CG2	0.418	0.019	54.00	2.53	0.18
123CG2	0.818	0.059	25.80	3.27	0.44
136CG1					
136CG2					
143CB	0.883	0.039	40.00	2.43	0.51
145CB	0.862	0.023	44.60	1.44	0.98
155CD1	0.805	0.036	13.10	1.50	1.40
155CG2	0.84	0.048	33.00	3.24	0.36
156CD1	0.357	0.018	32.10	1.90	0.39
156CD2	0.352	0.017	34.80	1.89	1.45

5.5. ^{2}H Relaxation model-free analysis of E:NADPH:3.

Methyl	S^2_{axis}	S^2_{axis} err	τ_e	τ_e err	χ^2
1CE	0.112	0.002	15.90	0.18	35.20
2CD1	0.467	0.019	16.60	1.33	0.98
2CG2					
4CD1	0.498	0.023	52.10	2.93	1.32
4CD2	0.559	0.265	147.00	137.00	1.96

Methyl	S^2_{axis}	S^2_{axis} err	τ_e	τ_e err	χ^2
5CD1	0.759	0.13	29.70	9.95	0.36
5CG2	0.868	0.186	48.20	35.80	2.43
6CB	0.988	0.165	87.00	23.60	0.59
7CB	0.872	0.14	72.00	18.60	0.56
8CD1	0.246	0.043	67.20	8.30	0.43
8CD2	0.189	0.01	40.30	1.50	9.11
9CB	0.664	0.147	40.30	17.30	1.12
10CG1	0.757	0.057	96.60	9.44	1.15
10CG2	1.135	0.178	16.90	8.14	4.85
13CG1					
13CG2	0.835	0.209	69.50	39.20	3.44
14CD1	0.937	0.094	6.29	4.86	0.56
14CG2					
16CE	0.35	0.006	5.61	0.23	15.10
19CB	0.95	0.046	22.60	1.91	0.63
20CE	0.323	0.032	13.20	0.76	0.36
24CD1	0.149	0.095	75.20	21.40	1.13
24CD2	0.282	0.036	37.00	4.92	0.24
26CB	0.978	0.109	50.60	8.81	1.58
28CD1	0.351	0.014	53.00	1.77	2.38
28CD2	0.304	0.025	67.30	3.12	0.88
29CB	0.98	0.042	38.00	2.27	0.81
35CG2					
36CD1	0.279	0.006	53.00	0.88	12.50
36CD2					
40CG1	0.892	0.104	53.80	8.94	0.54
40CG2					
41CD1	0.823	0.061	20.20	3.38	0.92
41CG2	0.8	0.054	36.90	3.98	1.29
42CE	0.882	0.033	3.56	1.19	0.27
46CG2	0.741	1.064	236.00	697.00	0.46
50CD1	0.733	0.04	17.00	2.15	1.41
50CG2					
54CD1					
54CD2	0.514	0.135	70.50	20.30	1.49
60CD1	0.29	0.013	27.50	1.23	3.19
60CG2	0.812	0.074	36.80	5.54	1.38
61CD1	0.326	0.03	35.80	3.29	7.30
61CG2	0.827	0.202	114.00	40.10	1.05
62CD1	0.519	0.089	86.20	17.10	2.64
62CD2	0.34	0.027	56.80	4.27	2.24
68CG2					
72CG1	0.821	0.171	62.70	18.30	0.00
72CG2	0.888	0.101	70.30	12.30	1.27
73CG2	0.972	0.054	37.70	3.32	2.15

Methyl	S^2_{axis}	$S^2_{axis}\,err$	τ_e	$\tau_e\,err$	χ^2
75CG1	0.815	0.068	69.40	7.89	0.40
75CG2	0.909	0.064	14.80	2.96	0.49
78CG1	0.841	0.05	32.60	2.95	1.69
78CG2	0.785	0.044	26.20	2.49	1.76
81CB	0.968	0.032	38.30	1.89	0.30
82CD1	0.628	0.031	26.50	1.92	2.38
82CG2	0.868	0.043	30.90	2.37	1.62
83CB					
84CB	0.877	0.056	56.00	4.76	0.97
88CG1					
88CG2	0.688	0.042	23.00	2.34	2.03
91CD1	0.748	0.023	12.00	1.37	2.02
91CG2	0.846	0.059	29.90	3.53	1.15
92CE	0.195	0.009	16.30	0.96	0.92
93CG1	0.91	0.095	51.60	8.54	1.41
93CG2	0.961	0.079	21.00	3.86	0.50
94CD1	0.759	0.102	25.20	5.88	0.18
94CG2					
99CG1	0.824	0.095	73.70	14.30	0.72
99CG2	0.561	0.043	45.70	5.75	2.68
104CD1					
104CD2	0.539	0.05	33.80	4.93	0.68
107CB	0.894	0.109	79.70	12.90	0.41
110CD1	0.679	0.382	52.20	42.50	1.09
110CD2	0.825	0.289	38.10	93.40	0.31
112CD1	0.532	1.227	281.00	817.00	0.89
112CD2	0.846	0.138	17.50	8.19	0.15
113CG2	0.851	0.133	39.20	12.10	2.09
115CD1	0.773	0.073	15.70	4.08	1.90
115CG2	0.792	0.071	40.40	5.96	0.64
117CB	1.092	0.206	71.10	26.70	0.04
119CG1					
119CG2					
123CG2	0.84	0.084	30.70	5.39	0.07
136CG1					
136CG2	0.694	0.041	60.10	4.66	2.38
143CB	0.954	0.052	38.90	3.13	0.45
145CB	0.888	0.036	43.40	2.33	2.33
155CD1	0.865	0.054	11.80	2.30	3.56
155CG2	0.933	0.077	29.40	4.48	0.01
156CD1	0.353	0.024	33.40	2.69	2.87
156CD2	0.377	0.02	35.50	2.19	1.83

5.6. ^{2}H Relaxation model-free analysis of E:NADPH:5.

Methyl	S^2_{axis}	S^2_{axis} err	τ_e	τ_e err	χ^2
1CE					
2CD1	0.41	0.014	19.7	1.05	0.77
2CG2	0.792	0.04	21.8	2.55	0.34
4CD1	0.549	0.022	53.2	3.05	0.71
4CD2	0.548	0.095	124	28	0.11
5CD1	0.81	0.083	28.4	6.65	0.20
5CG2	0.737	0.087	38.4	6.14	1.79
6CB	1.078	0.11	58.5	12.1	2.59
7CB	1.099	0.13	61	14.2	0.92
8CD1	0.217	0.033	78.9	8.24	0.32
8CD2	0.177	0.008	41.1	1.34	0.62
9CB	0.933	0.132	33.4	10.2	2.00
10CG1	0.668	0.052	121	11.4	0.39
10CG2	0.738	0.102	34.2	7.91	0.55
13CG1					
13CG2	0.694	0.143	82.6	27	0.45
14CD1	0.915	0.064	5.61	3.47	1.60
14CG2					
16CE	0.336	0.013	5.77	0.316	1.48
19CB	0.936	0.034	21	1.73	0.02
20CE	0.211	0.012	17.5	0.463	1.91
24CD1	0.189	0.061	58.1	13.2	0.22
24CD2	0.297	0.027	35.5	3.87	0.09
26CB	1	0.091	66.2	9.29	0.45
28CD1	0.314	0.01	55.3	1.56	0.25
28CD2	0.302	0.014	64.4	2.6	1.63
29CB	1.01	0.032	37.9	2.12	0.26
35CG2	0.857	0.072	24.3	4.39	0.06
36CD1	0.259	0.005	54.5	0.894	0.39
36CD2					
40CG1	0.891	0.068	44.3	6.05	0.25
40CG2					
41CD1	0.798	0.049	22.9	3.06	2.38
41CG2	0.912	0.05	35.3	3.62	0.35
42CE	0.866	0.026	4.53	1.04	1.69
46CG2					
50CD1	0.645	0.023	21.9	1.61	0.16
50CG2	0.659	0.021	23.2	1.47	0.78
54CD1	0.455	0.034	34.5	3.55	0.64
54CD2	0.485	0.065	58.7	9.97	0.33
60CD1	0.289	0.009	27	1.02	0.40

Methyl	S^2_{axis}	S^2_{axis} err	τ_e	τ_e err	χ^2
60CG2	0.895	0.066	33	5	0.23
61CD1	0.32	0.022	35.2	2.66	1.52
61CG2	0.886	0.144	104	26.7	1.60
62CD1	0.427	0.07	85.9	16.6	0.39
62CD2	0.3	0.024	58.4	4.34	1.96
68CG2					
72CG1	0.809	0.107	60.6	13.8	0.48
72CG2	0.817	0.076	59	8.72	0.49
73CG2	0.859	0.04	36.9	3.01	0.30
75CG1	0.844	0.056	81.3	8.74	5.20
75CG2	0.936	0.052	10	2.84	0.48
78CG1	0.872	0.041	28	2.56	0.81
78CG2	0.858	0.038	25.1	2.3	0.84
81CB	0.986	0.028	37.7	1.9	3.14
82CD1	0.659	0.024	25.9	1.79	1.67
82CG2	0.841	0.034	30.5	2.13	0.13
83CB					
84CB					
88CG1					
88CG2	0.791	0.036	25.2	2.3	2.21
91CD1	0.751	0.019	11.3	1.76	0.19
91CG2	0.878	0.049	32.7	3.39	1.76
92CE					
93CG1	0.961	0.071	42.3	6.41	0.29
93CG2	0.906	0.059	19.6	3.18	0.18
94CD1	0.777	0.059	16.8	3.7	0.61
94CG2	0.941	0.097	59.2	12.6	0.51
99CG1	0.85	0.079	62.2	11.7	0.01
99CG2	0.725	0.058	40	6.6	0.13
104CD1					
104CD2	0.544	0.042	39.6	4.78	0.06
107CB	0.967	0.095	66.6	11.4	0.31
110CD1	1.047	1.634	387	1370	0.13
110CD2	0.682	0.149	26.6	19.5	1.18
112CD1	0.461	0.406	89.1	146	0.45
112CD2	0.878	0.101	13.4	6.96	1.64
113CG2					
115CD1	0.702	0.045	21.4	3.11	1.21
115CG2	0.86	0.06	38.4	4.9	0.60
117CB	0.879	0.16	111	30.9	0.03
119CG1					
119CG2					
123CG2	0.898	0.07	22.7	4.67	0.13
136CG1	0.737	0.036	62.3	4.69	2.06
136CG2					

Methyl	S^2_{axis}	$S^2_{axis}\ err$	τ_e	$\tau_e\ err$	χ^2
143CB	0.997	0.045	39.5	3.06	0.36
145CB	0.859	0.031	43.2	2.33	0.72
155CD1	0.803	0.041	13	2.13	1.22
155CG2	0.9	0.06	28.5	3.95	0.03
156CD1	0.337	0.026	32.1	3.19	1.15
156CD2	0.365	0.017	35.1	2.09	0.41

Bibliography

1. Anderson AC, O'Neil RH, Surti TS, Stroud RM (2001) Approaches to solving the rigid receptor problem by identifying a minimal set of flexible residues during ligand docking. *Chem Biol* 8:445-457.

2. Fischer E (1894) Einfluss der Configuration auf die Wikung der Enzyme. *Ber Dtsch Chem Ges* 27:2985.

3. Koshland DE (1958) Application of a Theory of Enzyme Specificity to Protein Synthesis. *Proc Natl Acad Sci U S A* 44:98-104.

4. Boehr DD, Nussinov R, Wright PE (2009) The role of dynamic conformational ensembles in biomolecular recognition. *Nat Chem Biol* 5:789-796.

5. Teague SJ (2003) Implications of protein flexibility for drug discovery. *Nat Rev Drug Discov* 2:527-541.

6. Boehr DD, McElheny D, Dyson HJ, Wright PE (2006) The dynamic energy landscape of dihydrofolate reductase catalysis. *Science* 313:1638-1642.

7. Eisenmesser EZ, Bosco DA, Akke M, Kern D (2002) Enzyme dynamics during catalysis. *Science* 295:1520-1523.

8. Harel M, et al. (2000) Three-dimensional structures of Drosophila melanogaster acetylcholinesterase and of its complexes with two potent inhibitors. *Protein Sci* 9:1063-1072.

9. Kryger G, Silman I, Sussman JL (1999) Structure of acetylcholinesterase complexed with E2020 (Aricept): implications for the design of new anti-Alzheimer drugs. *Structure* 7:297-307.

10. Najmanovich R, Kuttner J, Sobolev V, Edelman M (2000) Side-chain flexibility in proteins upon ligand binding. *Proteins* 39:261-268.

11. Watkins RE, et al. (2001) The human nuclear xenobiotic receptor PXR: structural determinants of directed promiscuity. *Science* 292:2329-2333.

12. Pargellis C, et al. (2002) Inhibition of p38 MAP kinase by utilizing a novel allosteric binding site. *Nat Struct Biol* 9:268-272.

13. Ashani Y, Peggins JO, 3rd, Doctor BP (1992) Mechanism of inhibition of cholinesterases by huperzine A. *Biochem Biophys Res Commun* 184:719-726.

14. Palmer AG, 3rd (2004) NMR characterization of the dynamics of biomacromolecules. *Chem Rev* 104:3623-3640.

15. Jarymowycz VA, Stone MJ (2006) Fast time scale dynamics of protein backbones: NMR relaxation methods, applications, and functional consequences. *Chem Rev* 106:1624-1671.

16. Kay LE, Torchia DA, Bax A (1989) Backbone dynamics of proteins as studied by 15N inverse detected heteronuclear NMR spectroscopy: application to staphylococcal nuclease. *Biochemistry* 28:8972-8979.

17. Lipari G, Szabo A (1982) Model-free approach to the interpretation of nuclear magnetic resonance relaxation in macromolecules. 2. Analysis of experimental results. *J Am Chem Soc* 104:4559-4570.

18. Dellwo MJ, Wand AJ (1989) Model-Independent and Model-Dependent Analysis of the Global and Internal Dynamics of Cyclosporin A. *J Am Chem Soc* 111:4571-4578.

19. Igumenova TI, Frederick KK, Wand AJ (2006) Characterization of the fast dynamics of protein amino acid side chains using NMR relaxation in solution. *Chem Rev* 106:1672-1699.

20. Muhandiram DR, Yamazaki T, Sykes BD, Kay LE (1995) Measurement of 2H T1 and T1.rho. Relaxation Times in Uniformatly 13C-Labeled and Fractionally 2H-Labeled Proteins in Solution. *J Am Chem Soc* 117:11536-11544.

21. Clarkson MW, Lee AL (2004) Long-range dynamic effects of point mutations propagate through side chains in the serine protease inhibitor eglin c. *Biochemistry* 43:12448-12458.

22. Frederick KK, Marlow MS, Valentine KG, Wand AJ (2007) Conformational entropy in molecular recognition by proteins. *Nature* 448:325-329.

23. Fuentes EJ, Der CJ, Lee AL (2004) Ligand-dependent dynamics and intramolecular signaling in a PDZ domain. *J Mol Biol* 335:1105-1115.

24. Lee AL, Kinnear SA, Wand AJ (2000) Redistribution and loss of side chain entropy upon formation of a calmodulin-peptide complex. *Nat Struct Biol* 7:72-77.

25. Marlow MS, et al. (2010) The role of conformational entropy in molecular recognition by calmodulin. *Nat Chem Biol* 6:352-358.

26. Cavanagh J, et al. (2007) *Protein NMR Spectroscopy: Principles and Practice, Second Edition* (Elsevier Inc., New York).

27. Palmer AG, 3rd, Kroenke CD, Loria JP (2001) Nuclear magnetic resonance methods for quantifying microsecond-to-millisecond motions in biological macromolecules. *Methods Enzymol* 339:204-238.

28. Loria JPR, M.; and Palmer, A.G. (1999) A relaxation-compensated Carr-Purcell-Meiboom-Gill sequence for characterizing chemical exchange by NMR spectroscopy. *J Am Chem Soc* 121:2331-2332.

29. Mittermaier A, Kay LE (2006) New tools provide new insights in NMR studies of protein dynamics. *Science* 312:224-228.

30. Mulder FA, et al. (2001) Studying excited states of proteins by NMR spectroscopy. *Nat Struct Biol* 8:932-935.

31. Carver JP, Richards RE (1972) A general two-site solution for the chemical exchange produced dependence of T2 upon Carr-Purcell pulse separation. *J Magn Reson* 6:89-105.

32. Loria JP, Berlow RB, Watt ED (2008) Characterization of enzyme motions by solution NMR relaxation dispersion. *Acc Chem Res* 41:214-221.

33. Korzhnev DM, et al. (2004) Low-populated folding intermediates of Fyn SH3 characterized by relaxation dispersion NMR. *Nature* 430:586-590.

34. Vallurupalli P, Hansen DF, Kay LE (2008) Structures of invisible, excited protein states by relaxation dispersion NMR spectroscopy. *Proc Natl Acad Sci U S A* 105:11766-11771.

35. Farber S, Diamond LK (1948) Temporary remissions in acute leukemia in children produced by folic acid antagonist, 4-aminopteroyl-glutamic acid. *N Engl J Med* 238:787-793.

36. Fierke CA, Johnson KA, Benkovic SJ (1987) Construction and evaluation of the kinetic scheme associated with dihydrofolate reductase from Escherichia coli. *Biochemistry* 26:4085-4092.

37. Polshakov VI (2001) Dihydrofolate reductase: structural aspects of mechanism of enzyme catalysis and inhibition. *Russ Chem Bull, Int Ed* 50:1733-1751.

38. Bystroff C, Kraut J (1991) Crystal structure of unliganded Escherichia coli dihydrofolate reductase. Ligand-induced conformational changes and cooperativity in binding. *Biochemistry* 30:2227-2239.

39. Bystroff C, Oatley SJ, Kraut J (1990) Crystal structures of Escherichia coli dihydrofolate reductase: the NADP+ holoenzyme and the folate.NADP+ ternary

complex. Substrate binding and a model for the transition state. *Biochemistry* 29:3263-3277.

40.   Carroll MJ, et al. (2011) Direct detection of structurally resolved dynamics in a multi-conformation receptor-ligand complex. *J Am Chem Soc*, *in press*.

41.   Carroll MJ, et al. (2011) Evidence for dynamic motion in proteins as a mechanism for ligand ejection. *Submitted*.

42.   Sawaya MR, Kraut J (1997) Loop and Subdomain Movements in the Mechanism of *Escherichia coli* Dihydrofolate Reductase: Crystallographic Evidence. *Biochemistry* 36:586-603.

43.   Summerfield RL, et al. (2006) A 2.13 A Structure of *E. coli* Dihydrofolate Reductase Bound to a Novel Competitive Inhibitor Reveals a New Binding Surface Involving the M20 Loop Region. *J Med Chem* 49:6977-6986.

44.   Matthews DA, et al. (1977) Dihydrofolate reductase: x-ray structure of the binary complex with methotrexate. *Science* 197:452-455.

45.   Falzone CJ, Wright PE, Benkovic SJ (1994) Dynamics of a flexible loop in dihydrofolate reductase from Escherichia coli and its implication for catalysis. *Biochemistry* 33:439-442.

46.   Epstein DM, Benkovic SJ, Wright PE (1995) Dynamics of the dihydrofolate reductase-folate complex: catalytic sites and regions known to undergo conformational change exhibit diverse dynamical features. *Biochemistry* 34:11037-11048.

47.   Osborne MJ, Schnell, J., Benkovic, S.J., Dyson, H.J., and Wright, P.E. (2001) Backbone Dynamics in Dihydrofolate Reductase Complexes: Role of Loop Flexibility in the Catalytic Mechanism. *Biochemistry* 40:9846-9859.

48.   Schnell JR, Dyson, H.J., and Wright, P.E. (2004) Effect of Cofactor Binding and Loop Conformation on Side Chain Methyl Dynamics in Dihydrofolate Reductase. *Biochemistry* 43:374-383.

49.   Boehr DD, Dyson HJ, Wright PE (2008) Conformational relaxation following hydride transfer plays a limiting role in dihydrofolate reductase catalysis. *Biochemistry* 47:9227-9233.

50.   Boehr DD, McElheny D, Dyson HJ, Wright PE (2010) Millisecond timescale fluctuations in dihydrofolate reductase are exquisitely sensitive to the bound ligands. *Proc Natl Acad Sci U S A* 107:1373-1378.

51.   McElheny D, et al. (2005) Defining the role of active-site loop fluctuations in dihydrofolate reductase catalysis. *Proc Nat Acad Sci U S A* 102:5032-5037.

52.   Appleman JR, et al. (1988) Role of aspartate 27 in the binding of methotrexate to dihydrofolate reductase from Escherichia coli. *J Biol Chem* 263:9187-9198.

53.   Piper JR, et al. (1993) Lipophilic antifolates as candidates against opportunistic infections. *Adv Exp Med Biol* 338:429-433.

54.   Ashton WT, Walker FC, 3rd, Hynes JB (1973) Quinazolines as inhibitors of dihydrofolate reductase. 1. *J Med Chem* 16:694-697.

55.   Gangjee A, Zaveri N, Kothare M, Queener SF (1995) Nonclassical 2,4-diamino-6-(aminomethyl)-5,6,7,8-tetrahydroquinazoline antifolates: synthesis and biological activities. *J Med Chem* 38:3660-3668.

56.   Gangjee A, Zaveri N, Queener SF, Kisliuk RL (1995) Synthesis and Biological Activities of Tetrahydroquinazoline Analogs of Aminopterin and Methotrexate. *J Heterocyclic Chem* 32:243-247.

57.   Hitchings GH, Burchall JJ (1965) Inhibition of folate biosynthesis and function as a basis for chemotherapy. *Adv Enzymol Relat Areas Mol Biol* 27:417-468.

58.   Chan DC, Anderson AC (2006) Towards species-specific antifolates. *Curr Med Chem* 13:377-398.

59.   Baccanari DP, Joyner SS (1981) Dihydrofolate reductase hysteresis and its effect of inhibitor binding analyses. *Biochemistry* 20:1710-1716.

60.   Huennekens FM (1996) In search of dihydrofolate reductase. *Protein Sci* 5:1201-1208.

61.   Roth B, Cheng CC (1982) Recent progress in the medicinal chemistry of 2,4-diaminopyrimidines. *Prog Med Chem* 19:269-331.

62.   Chan JH, Roth B (1991) 2,4-Diamino-5-benzylpyrimidines as antibacterial agents. 14. 2,3-Dihydro-1-(2,4-diamino-5-pyrimidyl)-1H-indenes as conformationally restricted analogues of trimethoprim. *J Med Chem* 34:550-555.

63.   Davis SE, Rauckman BS, Chan JH, Roth B (1989) 2,4-Diamino-5-benzylpyrimidines and analogues as antibacterial agents. 11. Quinolylmethyl analogues with basic substituents conveying specificity. *J Med Chem* 32:1936-1942.

64.   Johnson JV, Rauchman BS, Baccanari DP, Roth B (1989) 2,4-Diamino-5-benzylpyrimidines and analogues as antibacterial agents. 12. 1,2-

Dihydroquinolylmethyl analogues with high activity and specificity for bacterial dihydrofolate reductase. *J Med Chem* 32:1942-1949.

65.   Rauckman BS, Roth B (1980) 2,4-Diamino-5-benzylpyrimidines and analogues as antibacterial agents. 3. C-Benzylation of aminopyridines with phenolic Mannich bases. Synthesis of 1- and 3-deaza analogues of trimethoprim. *J Med Chem* 23:384-391.

66.   Rauckman BS, Tidwell MY, Johnson JV, Roth B (1989) 2,4-Diamino-5-benzylpyrimidines and analogues as antibacterial agents. 10. 2,4-Diamino-5-(6-quinolylmethyl)- and -[(tetrahydro-6-quinolyl)methyl]pyrimidine derivatives. Further specificity studies. *J Med Chem* 32:1927-1935.

67.   Roth B, Aig E (1987) 2,4-Diamino-5-benzylpyrimidines as antibacterial agents. 8. The 3,4,5-triethyl isostere of trimethoprim. A study of specificity. *J Med Chem* 30:1998-2004.

68.   Roth B, Aig E, Lane K, Rauckman BS (1980) 2,4-Diamino-5-benzylpyrimidines as antibacterial agents. 4. 6-Substituted trimethoprim derivatives from phenolic Mannich intermediates. Application to the synthesis of trimethoprim and 3,5-dialkylbenzyl analogues. *J Med Chem* 23:535-541.

69.   Roth B, et al. (1981) 2,4-Diamino-5-benzylpyrimidines and analogues as antibacterial agents. 5. 3',5'-Dimethoxy-4'-substituted-benzyl analogues of trimethoprim. *J Med Chem* 24:933-941.

70.   Roth B, et al. (1988) 2,4-Diamino-5-benzylpyrimidines and analogues as antibacterial agents. 9. Lipophilic trimethoprim analogues as antigonococcal agents. *J Med Chem* 31:122-129.

71.   Roth B, et al. (1987) 2,4-Diamino-5-benzylpyrimidines as antibacterial agents. 7. Analysis of the effect of 3,5-dialkyl substituent size and shape on binding to four different dihydrofolate reductase enzymes. *J Med Chem* 30:348-356.

72.   Roth B, Strelitz JZ, Rauckman BS (1980) 2,4-Diamino-5-benzylpyrimidines and analogues as antibacterial agents. 2. C-Alkylation of pyrimidines with Mannich bases and application to the synthesis of trimethoprim and analogues. *J Med Chem* 23:379-384.

73.   Roth B, et al. (1989) 2,4-Diamino-5-benzylpyrimidines as antibacterial agents. 13. Some alkenyl derivatives with high in vitro activity against anaerobic organisms. *J Med Chem* 32:1949-1958.

74.   Stuart A, Paterson T, Roth B, Aig E (1983) 2,4-diamino-5-benzylpyrimidines and analogues as antibacterial agents. 6. A one-step synthesis of new trimethoprim derivatives and activity analysis by molecular modeling. *J Med Chem* 26:667-673.

75.   Maskell JP, Sefton AM, Hall LM (2001) Multiple mutations modulate the function of dihydrofolate reductase in trimethoprim-resistant Streptococcus pneumoniae. *Antimicrob Agents Chemother* 45:1104-1108.

76.   Watson M, Liu JW, Ollis D (2007) Directed evolution of trimethoprim resistance in Escherichia coli. *FEBS J* 274:2661-2671.

77.   Zolli-Juran M, et al. (2003) High throughput screening identifies novel inhibitors of Escherichia coli dihydrofolate reductase that are competitive with dihydrofolate. *Bioorg Med Chem Lett* 13:2493-2496.

78.   Banerjee D, et al. (2002) Novel aspects of resistance to drugs targeted to dihydrofolate reductase and thymidylate synthase. *Biochim Biophys Acta* 1587:164-173.

79.   Mauldin RV, Carroll MJ, Lee AL (2009) Dynamic Dysfunction in Dihydrofolate Reductase Results from Antifolate Drug Binding: Modulations of Dynamics within a Structural State. *Structure* 17:386-394.

80.   Beach H, Cole R, Gill ML, Loria JP (2005) Conservation of mus-ms enzyme motions in the apo- and substrate-mimicked state. *J Am Chem Soc* 127:9167-9176.

81.   Sich C, et al. (2000) Solution structure of a neurotrophic ligand bound to FKBP12 and its effects on protein dynamics. *Eur J Biochem* 267:5342-5355.

82.   Moy FJ, et al. (2002) Impact of mobility on structure-based drug design for the MMPs. *J Am Chem Soc* 124:12658-12659.

83.   Shapiro YE, et al. (2002) Domain flexibility in ligand-free and inhibitor-bound Escherichia coli adenylate kinase based on a mode-coupling analysis of 15N spin relaxation. *Biochemistry* 41:6271-6281.

84.   Ahmed AH, Loh AP, Jane DE, Oswald RE (2007) Dynamics of the S1S2 glutamate binding domain of GluR2 measured using 19F NMR spectroscopy. *J Biol Chem* 282:12773-12784.

85.   Showalter SA, et al. (2008) Quantitative lid dynamics of MDM2 reveals differential ligand binding modes of the p53-binding cleft. *J Am Chem Soc* 130:6472-6478.

86.   Cameron CE, Benkovic SJ (1997) Evidence for a functional role of the dynamics of glycine-121 of Escherichia coli dihydrofolate reductase obtained from kinetic analysis of a site-directed mutant. *Biochemistry* 36:15792-15800.

87.   Delaglio F, et al. (1995) NMRPipe - a multidimensional spectral processing system based on Unix pipes. *J Biomol NMR* 6:277-293.

88.	Johnson BA, Blevins RA (1994) NMRView - a computer program for the visualization and analysis of NMR data. *J Biomol NMR* 4:603-614.

89.	Muhandiram DR, Kay LE (1994) Gradient-Enhanced Triple-Resonance Three-Dimensional NMR Experiments with Improved Sensitivity. *J Magn Reson B* 103:203-216.

90.	Bax A, Delaglio F, Grzesiek S, Vuister GW (1994) Resonance assignment of methionine methyl groups and chi 3 angular information from long-range proton-carbon and carbon-carbon J correlation in a calmodulin-peptide complex. *J Biomol NMR* 4:787-797.

91.	Uhrin D, et al. (2000) 3D HCCH(3)-TOCSY for resonance assignment of methyl-containing side chains in (13)C-labeled proteins. *J Magn Reson* 142:288-293.

92.	Neri D, et al. (1989) Stereospecific nuclear magnetic resonance assignments of the methyl groups of valine and leucine in the DNA-binding domain of the 434 repressor by biosynthetically directed fractional 13C labeling. *Biochemistry* 28:7510-7516.

93.	Osborne MJ, Wright PE (2001) Anisotropic rotational diffusion in model-free analysis for a ternary DHFR complex. *J Biomol NMR* 19:209-230.

94.	Lee LK, Rance M, Chazin WJ, Palmer AG, 3rd (1997) Rotational diffusion anisotropy of proteins from simultaneous analysis of 15N and 13C alpha nuclear spin relaxation. *J Biomol NMR* 9:287-298.

95.	d'Auvergne EJ, Gooley PR (2003) The use of model selection in the model-free analysis of protein dynamics. *J Biomol NMR* 25:25-39.

96.	Polshakov VI, et al. (2002) NMR-based solution structure of the complex of Lactobacillus casei dihydrofolate reductase with trimethoprim and NADPH. *J Biomol NMR* 24:67-70.

97.	Osborne MJ, Venkitakrishnan RP, Dyson HJ, Wright PE (2003) Diagnostic chemical shift markers for loop conformation and substrate and cofactor binding in dihydrofolate reductase complexes. *Protein Sci* 12:2230-2238.

98.	Chen J, Dima RI, Thirumalai D (2007) Allosteric communication in dihydrofolate reductase: signaling network and pathways for closed to occluded transition and back. *J Mol Biol* 374:250-266.

99.	Bursavich MG, Rich DH (2002) Designing non-peptide peptidomimetics in the 21st century: inhibitors targeting conformational ensembles. *J Med Chem* 45:541-558.

100. B-Rao C, Subramanian J, Sharma SD (2009) Managing protein flexibility in docking and its applications. *Drug Discov Today* 14:394-400.

101. Mobley DL, Dill KA (2009) Binding of Small-Molecule Ligands to Proteins: "What You See" Is Not Always "What You Get". *Structure* 17:489-498.

102. Bruning JB, et al. Coupling of receptor conformation and ligand orientation determine graded activity. *Nat Chem Biol* 6:837-843.

103. Peng JW (2009) Communication breakdown: protein dynamics and drug design. *Structure* 17:319-320.

104. May LT, Leach K, Sexton PM, Christopoulos A (2007) Allosteric modulation of G protein-coupled receptors. *Annu Rev Pharmacol Toxicol* 47:1-51.

105. Lee GM, Craik CS (2009) Trapping moving targets with small molecules. *Science* 324:213-215.

106. Zhang J, et al. (2010) Targeting Bcr-Abl by combining allosteric with ATP-binding-site inhibitors. *Nature* 463:501-506.

107. Yang CY, Wang R, Wang S (2005) A systematic analysis of the effect of small-molecule binding on protein flexibility of the ligand-binding sites. *J Med Chem* 48:5648-5650.

108. Schnell JR, Dyson HJ, Wright PE (2004) Structure, dynamics, and catalytic function of dihydrofolate reductase. *Annu Rev Biophys Biomol Struct* 33:119-140.

109. Singh J, Gurney ME (2005) Preparation of 2,4-diamioquinazolines for treatment of spinal muscular atrophy. WO 2005-US19753.

110. Wider G, Dreier L (2006) Measuring protein concentrations by NMR spectroscopy. *J Am Chem Soc* 128:2571-2576.

111. Skrynnikov NR, Dahlquist FW, Kay LE (2002) Reconstructing NMR spectra of "invisible" excited protein states using HSQC and HMQC experiments. *J Am Chem Soc* 124:12352-12360.

112. Chou JJ, et al. (2001) A simple apparatus for generating stretched polyacrylamide gels, yielding uniform alignment of proteins and detergent micelles. *J Biomol NMR* 21:377-382.

113. Cornilescu G, Marquardt JL, Ottier M, Bax A (1998) Validation of protein structure from anisotropic carbonyl chemical shifts in a dilute liquid cystalline phase. *J Am Chem Soc* 120:6836-6837.

114. Lee W, Revington MJ, Arrowsmith C, Kay LE (1994) A pulsed field gradient isotope-filtered 3D 13C HMQC-NOESY experiment for extracting intermolecular NOE contacts in molecular complexes. *FEBS Lett* 350:87-90.

115. Bax A, Grzesiek S, Gronenborn AM, Clore GM (1994) Isotope-Filtered 2D HOHAHA Spectroscopy of a Peptide-Protein Complex Using Heteronuclear Hartmann-Hahn Dephasing. *J Mag Reson, Series A* 106:269-273.

116. Otwinowski Z, Minor W (1997) Processing of X-ray Diffraction Data Collected in Oscillation Mode. *Methods Enzymol* 276:307-326.

117. Collaborative Computational Project, number 4 (1994) The CCP4 suite: programs for protein crystallography. *Acta Crystallogr D Biol Crystallogr* 50:760-763.

118. Emsley P, Cowtan K (2004) Coot: model-building tools for molecular graphics. *Acta Crystallogr D Biol Crystallogr* 60:2126-2132.

119. Bricogne G, et al. (2009) 2.8.0. ed. Cambridge, United Kingdom: Global Phasing Ltd.

120. Sherman W, et al. (2006) Novel procedure for modeling ligand/receptor induced fit effects. *J Med Chem* 49:534-553.

121. Friesner RA, et al. (2006) Extra precision glide: docking and scoring incorporating a model of hydrophobic enclosure for protein-ligand complexes. *J Med Chem* 49:6177-6196.

122. Andrec M, et al. (2002) Complete protein structure determination using backbone residual dipolar couplings and sidechain rotamer prediction. *J Struct Funct Genomics* 2:103-111.

123. Whitlow M, et al. (2001) X-Ray crystal structures of Candida albicans dihydrofolate reductase: high resolution ternary complexes in which the dihydronicotinamide moiety of NADPH is displaced by an inhibitor. *J Med Chem* 44:2928-2932.

124. Whitlow M, et al. (1997) X-ray crystallographic studies of Candida albicans dihydrofolate reductase. High resolution structures of the holoenzyme and an inhibited ternary complex. *J Biol Chem* 272:30289-30298.

125. Boehr DD, Dyson HJ, Wright PE (2006) An NMR perspective on enzyme dynamics. *Chem Rev* 106:3055-3079.

126. Cole R, Loria JP (2002) Evidence for flexibility in the function of ribonuclease A. *Biochemistry* 41:6072-6081.

127. Arora K, Brooks III CL (2009) Functionally Important Conformations of the Met20 Loop in Dihydrofolate Reductase are Populated by Rapid Thermal Fluctuations. *J Am Chem Soc* 131:5642-5647.

128. Das K, et al. (2008) High-resolution structures of HIV-1 reverse transcriptase/TMC278 complexes: strategic flexibility explains potency against resistance mutations. *Proc Natl Acad Sci U S A* 105:1466-1471.

129. Schames JR, et al. (2004) Discovery of a novel binding trench in HIV integrase. *J Med Chem* 47:1879-1881.

130. Hazuda DJ, et al. (2004) A naphthyridine carboxamide provides evidence for discordant resistance between mechanistically identical inhibitors of HIV-1 integrase. *Proc Natl Acad Sci U S A* 101:11233-11238.

131. Kobilka BK, Deupi X (2007) Conformational complexity of G-protein-coupled receptors. *Trends Pharmacol Sci* 28:397-406.

132. Ghanouni P, et al. (2001) Functionally different agonists induce distinct conformations in the G protein coupling domain of the beta 2 adrenergic receptor. *J Biol Chem* 276:24433-24436.

133. Vajpai N, et al. (2008) Solution conformations and dynamics of ABL kinase-inhibitor complexes determined by NMR substantiate the different binding modes of imatinib/nilotinib and dasatinib. *J Biol Chem* 283:18292-18302.

134. Olson JS, Phillips GN, Jr. (1996) Kinetic pathways and barriers for ligand binding to myoglobin. *J Biol Chem* 271:17593-17596.

135. Bourgeois D, et al. (2003) Complex landscape of protein structural dynamics unveiled by nanosecond Laue crystallography. *Proc Natl Acad Sci U S A* 100:8704-8709.

136. Bourne HR, Sanders DA, McCormick F (1991) The GTPase superfamily: conserved structure and molecular mechanism. *Nature* 349:117-127.

137. Ishima R, et al. (1999) Flap opening and dimer-interface flexibility in the free and inhibitor-bound HIV protease, and their implications for function. *Structure* 7:1047-1055.

138. Eisenmesser EZ, et al. (2005) Intrinsic dynamics of an enzyme underlies catalysis. *Nature* 438:117-121.

139. Labeikovsky W, Eisenmesser EZ, Bosco DA, Kern D (2007) Structure and dynamics of pin1 during catalysis by NMR. *J Mol Biol* 367:1370-1381.

140.   Masterson LR, et al. Dynamics connect substrate recognition to catalysis in protein kinase A. *Nat Chem Biol* 6:821-828.

141.   Sapienza PJ, Mauldin RV, Lee AL Multi-timescale dynamics study of FKBP12 along the rapamycin-mTOR binding coordinate. *J Mol Biol* 405:378-394.

142.   Gangjee A, Zaveri N, Queener SF, Kisliuk RL (1995) Synthesis and Biological Activities of Tetrahydroquinazoline Analogs of Aminopterin and Methotrexate. *Journal of Heterocyclic Chemistry* 32:243-247.

143.   Leslie AG (2006) The integration of macromolecular diffraction data. *Acta Crystallogr D Biol Crystallogr* 62:48-57.

144.   Frauenfelder H, Sligar SG, Wolynes PG (1991) The energy landscapes and motions of proteins. *Science* 254:1598-1603.

145.   Rozovsky S, Jogl G, Tong L, McDermott AE (2001) Solution-state NMR investigations of triosephosphate isomerase active site loop motion: ligand release in relation to active site loop dynamics. *J Mol Biol* 310:271-280.

146.   Kovrigin EL, Cole R, Loria JP (2003) Temperature dependence of the backbone dynamics of ribonuclease A in the ground state and bound to the inhibitor 5'-phosphothymidine (3'-5')pyrophosphate adenosine 3'-phosphate. *Biochemistry* 42:5279-5291.

147.   Rasmussen BF, Stock AM, Ringe D, Petsko GA (1992) Crystalline ribonuclease A loses function below the dynamical transition at 220 K. *Nature* 357:423-424.

148.   Volkman BF, Lipson D, Wemmer DE, Kern D (2001) Two-state allosteric behavior in a single-domain signaling protein. *Science* 291:2429-2433.

149.   Petit CM, et al. (2009) Hidden dynamic allostery in a PDZ domain. *Proc Natl Acad Sci U S A* 106:18249-18254.

150.   Tzeng SR, Kalodimos CG (2009) Dynamic activation of an allosteric regulatory protein. *Nature* 462:368-372.

151.   Watt ED, Shimada H, Kovrigin EL, Loria JP (2007) The mechanism of rate-limiting motions in enzyme function. *Proc Natl Acad Sci U S A* 104:11981-11986.

152.   Namanja AT, et al. (2010) Toward flexibility-activity relationships by NMR spectroscopy: dynamics of Pin1 ligands. *J Am Chem Soc* 132:5607-5609.

153.   Frieden C (1979) Slow transitions and hysteretic behavior in enzymes. *Annu Rev Biochem* 48:471-489.

154. Hansen DF, Vallurupalli P, Kay LE (2008) Using relaxation dispersion NMR spectroscopy to determine structures of excited, invisible protein states. *J Biomol NMR* 41:113-120.

155. Hansen DF, et al. (2008) Probing chemical shifts of invisible states of proteins with relaxation dispersion NMR spectroscopy: how well can we do? *J Am Chem Soc* 130:2667-2675.

156. Mauldin RV, Lee AL Nuclear magnetic resonance study of the role of M42 in the solution dynamics of Escherichia coli dihydrofolate reductase. *Biochemistry* 49:1606-1615.

157. Lee AL, Wand AJ (2001) Microscopic origins of entropy, heat capacity and the glass transition in proteins. *Nature* 411:501-504.

158. Lee AL, et al. (2002) Temperature dependence of the internal dynamics of a calmodulin-peptide complex. *Biochemistry* 41:13814-13825.

159. Li Z, Raychaudhuri S, Wand AJ (1996) Insights into the local residual entropy of proteins provided by NMR relaxation. *Protein Sci* 5:2647-2650.

160. Yang D, et al. (1997) Contributions to protein entropy and heat capacity from bond vector motions measured by NMR spin relaxation. *J Mol Biol* 272:790-804.

161. Li DW, Bruschweiler R (2009) A dictionary for protein side-chain entropies from NMR order parameters. *J Am Chem Soc* 131:7226-7227.

162. Ren J, et al. (2000) Binding of the second generation non-nucleoside inhibitor S-1153 to HIV-1 reverse transcriptase involves extensive main chain hydrogen bonding. *J Biol Chem* 275:14316-14320.

163. Adams J, Johnson K, Matthews R, Benkovic SJ (1989) Effects of distal point-site mutations on the binding and catalysis of dihydrofolate reductase from Escherichia coli. *Biochemistry* 28:6611-6618.

164. Igumenova TI, Lee AL, Wand AJ (2005) Backbone and side chain dynamics of mutant calmodulin-peptide complexes. *Biochemistry* 44:12627-12639.

165. Wang T, et al. (2005) Changes in calmodulin main-chain dynamics upon ligand binding revealed by cross-correlated NMR relaxation measurements. *J Am Chem Soc* 127:828-829.